UNIVERSITÀ
DEGLI STUDI
FIRENZE

DOTTORATO DI RICERCA IN
FISICA E ASTRONOMIA

CICLO XXX

COORDINATORE Prof. Raffaello D'Alessandro

Quantum systems of ultracold atoms with tunable interactions

Settore Scientifico Disciplinare: FIS/03 Fisica della materia

Dottorando

Dott. Giulia Faraoni

Giulia Faraoni

Tutori

Prof. Giovanni Modugno

Giovanni Modugno

Prof. Francesca Ferlaino

Francesca Ferlaino

Coordinatore

Prof. Raffaello D'Alessandro

Raffaello D'Alessandro

Anni 2014/2017

Contents

Introduction

The first experimental realizations of a Bose-Einstein condensate (BEC) by the group of Eric Cornell and Carl Wiemann at JILA (Boulder, Colorado) [1] and Wolfgang Ketterle at MIT (Cambridge, Massachusetts) [2] in 1995, opened up a new era in the field of atomic physics. The existence of a quantum state of matter characterized by bosonic particles macroscopically occupying the same single-particle quantum state, had been theoretically predicted by Einstein [3], 70 years before its first observation in the lab. In the long quest for the experimental realization of Bose-Einstein condensation, a major breakthrough is represented by the huge progresses in laser cooling and trapping techniques of alkali atoms, together with the estabilishment of evaporative cooling of alkalis, developed in late 1980's, which have made it possible to reach the extremely low temperatures, on the order of ~ 100 nK, and the dilute regime, necessary for Bose-Einstein condensation to occur in a atomic gas. In 2001 Cornell, Wiemann and Ketterle received the Nobel Prize in physics for their remarkable achievement.

An enormous interest has arised on BECs since their first experimental realizations. These macroscopic quantum objects have proven, for instance, to exhibit a superfluid behaviour through the formation of quantized vortices [4], thus allowing to test theories developed in the context of superfluid helium. Early studies on BECs (see ref. [5] for a review) include the demonstration of matter-wave interference [6]. In the last ten years, an increasing interest has developed in the ultracold atomic community towards using degenerate gases for quantum simulation of condensed matter physics phenomena. Complex Hamiltonians have been engineered in BECs thanks to the unprecedented control and flexibility of such systems, not achievable in condensed matter. Among the theories that have been simulated one finds the Bose-Hubbard model [7], the superfluid to Mott-insulator transition [8],

and Anderson localization in disordered media [9, 10].

Although BECs are very dilute systems with respect to solid state systems, most of their properties are governed by interactions between particles. In the ultracold regime characteristic of quantum gases, typically the only relevant scattering processes are two-body isotropic elastic collisions (s-wave scattering). The low-energy scattering is fully determined by a single parameter, namely the s-wave scattering length. Thus, the details of the real interatomic short-range potential can be ignored and one can replace the true potential by an effective contact interaction potential, with the coupling given by the s-wave scattering length. One of the most prominent properties of ultracold atomic systems is that the s-wave scattering length can be tuned in experiments, by using Feshbach resonances [11], through the simple application of a homogeneous magnetic field to the system. Thus, depending on an external magnetic field, the atoms can be made non-interacting or strongly interacting, and even the sign of the interactions (attractive or repulsive) can be changed across a Feshbach resonance. Beside interactions, many other system parameters can be controlled in experiments. For instance, the temperature and density of the gas, and the geometry and dimensionality of the system.

After the pioneering experiments on rubidium (Cornell and Wiemann), and sodium (Ketterle), other alkali atoms, such as lithium [12], cesium [13] and potassium [14] have been brought to degeneracy in the past years. Moreover, thanks to advances in laser technology and more sophisticated cooling schemes, many other atomic species than alkalis have been Bose-condensed: spin-polarized hydrogen [15], metastable helium [16, 17], chromium [18], ytterbium [19], and alkaline earth elements such as calcium [20] and strontium [21, 22]. More recently, Bose-Einstein condensation has been also achieved in the strongly magnetic lanthanides dysprosium [23], and erbium [24]. Among the above listed BECs, particularly relevant in the framework of my thesis are the BEC of alkali potassium 39 atoms, first realized by the group of Giovanni Modugno at LENS in Florence (Italy) [25], and the BEC of magnetic lanthanide erbium 166, created for the first time by the group of Francesca Ferlaino at the University of Innsbruck (Austria) [26], that constitute

the two systems on which I have been working during my PhD.

Each atomic species brings new ingredients in the physics at play, which originate from the peculiar properties of the internal atomic structure and electron configuration. Thus, potassium (K) presents very large Feshbach resonances [27], which provide a broad tunability of the s-wave scattering length over many orders of magnitude in this system, allowing to transform the gas from attractive to non-interacting, to strongly repulsive. This property of K makes it particularly suited for studying phenomena which require a high degree of control of the short-range interatomic interactions, such as the many-body localization phenomenon of condensed matter physics [28]. This phenomenon, which is essentially the generalization of the above mentioned Anderson localization (of non-interacting particles) in disordered potentials, to weakly interacting systems, is a very general issue, concerning, for instance, thin-film superconductors [29] and superfluid helium in porous media [30]. Quantum simulation with K BEC could give insights into the complex interplay of interactions and disorder in such systems. This is precisely the long-term goal of the experiment with K in which I have been involved during part of my thesis work.

Erbium (Er), for its part, presents a large magnetic moment in its ground state, and therefore magnetic dipole-dipole interactions (DDI) occur in addition to contact interactions in Er BECs. The distinguishing features of DDI are their long-range and anistropic character, which contrasts to the isotropic and short-range nature of interactions in conventional (non-dipolar) atomic gases. As a consequence, a wealth of novel phenomena can be studied in dipolar systems compared to experiments with alkali atoms, as reviewed in ref. [31]. Dipolar interactions account for many physically and biologically significant phenomena, ranging from novel phases of matter appearing in ultracold quantum many-body systems, such as the liquid-like quantum droplets, recently observed in dipolar BECs of Dy [32] and Er [26], or liquid crystals and ferrofluids in soft condensed matter physics [33], to the mechanism underlaying protein folding [34]. Of fundamental importance in the context of this thesis is the prediction, of almost 15 years ago, that dipolar BECs show a roton-maxon low-energy excitation spectrum, reminescent of that in superfluid helium [35], and originating from the peculiar properties of the DDI. Observing this phenomenon in a fully controllable system, such as a dipolar BEC,

could enlighten new aspects of superfluidity in ultracold matter, hardly accessible with superfluid helium. Part of my PhD thesis work has been devoted to the experimental observation of the roton mode excitation in a dipolar BEC of Er atoms.

Thesis overview

My PhD project developes in the framework of a scientific collaboration between two leading European research groups in the field of experimental ultracold atomic physics: the group of Prof. Giovanni Modugno at LENS, in Florence, and the group of Prof. Francesca Ferlaino at the Experimental Physics Institute of the University of Innsbruck (Innsbruck, Austria). The first part of my PhD (November 2014 - April 2016) has been carried out in the group of Prof. Modugno, while in the second part (May 2016 - July 2017) I worked in the group of Prof. Ferlaino.

The goal of my PhD work is to exploit tunable atomic interactions of different nature, namely short-range and DDI, to investigate many-body phenomena in ultracold bosonic quantum gases. During my work in Florence, I have been involved in the construction of a new experiment, aimed at studying the impact of weak short-range interatomic interactions on a three-dimensional Anderson localized system in a controllable disordered potential [36]. My contribution to this experiment has been at the very initial stage, and consisted in the design of a new vacuum apparatus necessary to produce a Bose-Einstein condensate of ^{39}K atoms. In Innsbruck I have been working on a fully operating machine, producing dipolar BECs of ^{166}Er atoms. Here, I have been involved in the *first* experimental observation of the roton mode population in a dipolar BEC. My contribution to the ERBIUM experiment in Innsbruck has been twofold: I partecipated to the measurements, and performed numerical simulations.

This thesis is organized as follows.

- In **Chapter 1** I first briefly review the internal structure of isolated atoms, and then give a theoretical description of the interaction of atoms with optical and magnetic fields. These interactions are at the basis of the fundamental

cooling and trapping techniques used in ultracold atomic experiments to produce a BEC, that are presented in the chapter. Their knowledge is essential for the design of a vacuum apparatus. I underline the similarities and differences between a laboratory apparatus typically used for producing a BEC of K, and the one used for Er, which depend on the peculiar properties of the two atomic species.

- **Chapter 2** is devoted to the description of interatomic interactions in ultracold quantum gases. Here I introduce experimental and theoretical tools that will be employed in the investigation described in Chapter 4. Basics of quantum scattering theory are given, demonstrating that low-energy short-range scattering is fully described by the s-wave scattering length. The mechanism of Feshbach resonances for tuning the s-wave scattering length in experiments is presented. The long-range and anisotropic dipole-dipole interaction, playing a fundamental role in strongly magnetic BECs of Er atoms, is then described. Later, I present the theoretical description of a weakly interacting BEC in a trap, in a mean-field approximation. In this approximation, the Gross-Pitaevskii equation describing the dynamics of the condensate state is derived. A generalized form of the Gross-Pitaevskii equation for dipolar systems is finally obtained.

- In **Chapter 3** I present the design of the vacuum system for the new experimental apparatus for the production of BECs of ^{39}K in Florence. Here, I give technical descriptions of the various components of the vacuum system. The experimental steps towards the realization of the BEC that are planned for this experiment are presented. They fundamentally determine the choices of design.

- **Chapter 4** focuses on the investigation of the roton mode excitation in a dipolar BEC of ^{166}Er atoms, in which I have been involved during the time I spent in Innsbruck. After a first historical introduction on rotons in superfluid helium, I present the theoretical proposal of 2003 [35], at the basis of our study, predicting the emergence of a minimum of energy at finite momentum in the low-energy excitation spectrum of a dipolar BEC confined

in a anisotropic geometry. The experimental realization of the ^{166}Er BEC is described. Then, the measurements performed in the lab are presented, and the results are given, showing the expected population of the roton mode in our system. The results are compared to theoretical models, specifically developed for our system parameters. Finally, I present numerical simulations that I personally performed to have additional insights on the system, in the regime where the roton physics occurs. Part of the work presented in this chapter is reported in ref. [37].

Finally, I conclude the thesis and give outlooks on possible future investigations, following the work presented here.

Chapter 1

Production and detection of ultracold bosonic quantum gases

In this chapter, after a short introduction on the phenomenon of Bose-Einstein condensation in dilute atomic gases, I will briefly review the main properties of the internal structure of isolated atoms and of atoms interacting with magnetic and light fields. These interactions are at the basis of the laser cooling and atom trapping techniques used to produce degenerate gases in a laboratory. The chapter is then devoted to the description of these techniques. Particular attention is directed towards the specific techniques typically used with K and Er. The knowledge of the techniques used with K is of fundamental importance for the design of the vacuum apparatus, that will be presented in Chapter 3. Finally, the detection scheme used in the framework of this thesis is described.

1.1 Bose-Einstein condensation in dilute atomic gases

The phenomenon of Bose-Einstein condensation in an ideal (non-interacting) gas, proposed by Einstein in 1924 [3] is a paradigm of quantum statistical mechanics. It is based on the indistiguishability and wave nature of particles. Bosons are particles with integer spin, therefore the wave function for a system of identical bosons is symmetric under interchange of any two particles. Unlike fermions, which have half-odd-integer spin and antisymmetric wave functions, bosons may

occupy the same single-particle state.

In a simplified picture, non-interacting atoms in a gas may be regarded as quantum-mechanical wavepackets which have an extent on the order of a *thermal de Broglie wavelength*, defined as [38]:

$$\lambda_{dB} = \left(\frac{2\pi\hbar^2}{m k_B T} \right)^{1/2}, \tag{1.1}$$

where $\hbar$ is the Planck constant divided by 2π, k_B is the Boltzmann constant, m the mass of the atom and T is the temperature of the gas. λ_{dB} expresses the atom position uncertainty associated with the thermal momentum distribution. If the temperature of the gas decreases, λ_{dB} increases. When atoms are cooled to the point where λ_{dB} is comparable to the mean interatomic separation, the atomic wavepackets "overlap" and, in the case of bosons, interfere constructively. At this temperature, the indistinguishability of particles becomes important for the macroscopic behaviour of the gas: bosons undergo a phase transition and form a Bose-Einstein condensate (BEC), a coherent cloud of atoms all occupying the same single-particle ground state [3, 39]. The many-body ground-state wavefunction is then the product of many identical single-particle ground-state wavefunctions. This single-particle wavefunction is called the *condensate wavefunction* or *macroscopic wavefunction*. Introducing the *phase space density*, defined as $\rho = n\lambda_{dB}^3$, where n is the atomic spatial density of the gas, assumed to be infinite and uniform, the Bose-Einstein condensation takes place when $\rho = 2.612$ [38]. For gases of alkali atoms at room temperature ($T_{room} \sim 300$ K) and atmospheric pressure, typical densities are on the order of 10^{14} cm^{-3}, which lead to a phase space density of $\sim 10^{-7}$. In order to increase the phase space density of at least 7 orders of magnitude to reach Bose-Einstein condensation, one has either to increase the density, or to decrease the temperature of the gas. It is worth noticing here that the Bose-Einstein condensation phase transition occurs in a regime of pressure and temperature, for which the equilibrium state of matter is the solid state for most of the elements of the periodic table, with the only exception of helium, which instead remains liquid even at absolute zero [38]. Since the solid state is the true ground state of the system, the BEC is in a metastable state. It is clear that, in this state, neglecting the interactions between the atoms is unrealistic. The main

processes that lead to the solidification of the gas are the ones in which three atoms collide: two of them form a molecule and the third one ensures conservation of momentum. However, if the sample is sufficiently dilute, the probability to find three atoms close enough to cause a three-body collision can be negligible, and the lifetime of the metastable BEC state can be long enough to allow its observation in experiments.

1.2 Theoretical background: atomic internal structure and atom-light interaction

In this section I will first briefly recall the basic atomic structure and the atomic properties which play an important role in experiments on cold atomic gases. Then, I will describe the influence of magnetic and optical fields on atomic energy levels, and introduce the semiclassical theory of atom-light interaction.

1.2.1 Energy level structure of isolated atoms

On a gross level of approximation, the description of the atomic energy level structure is typically based on considering an atom as constituded by one electron moving in the central Coulomb potential created by the nucleus (hydrogen-like system) [40]. The hydrogen-like hamiltonian $\hat{H}_0 = \frac{p^2}{2m} - \frac{Ze^2}{4\pi\epsilon_0 r}$, where Z is the atomic number, e the electron charge, and ϵ_0 the vacuum permettivity, has a central symmetry. Therefore, it commutes with the total angular momentum operator $\hat{L}^2$, and with its z-component $\hat{L}_z$. The eigenfunctions of $\hat{H}_0$ are then characterized by three quantum numbers, n, l, m, where n is the principal quantum number, which takes integer values $n \geq 1$, l indicates the orbital angular momentum quantum number, with values $l = 0, ..., (n-1)$, and m is its z-component, with $m = -l, ..., l$. The wavefunctions are of the form $\psi_{n,l,m}(\mathbf{r}) = R_{nl}(r)Y_{l,m}(\theta, \phi)$ [1], and the energy levels are organized in a shell structure, indexed by the quantum number n and characterized by a n^2-fold degeneracy.

[1] $R_{nl}(r)$ contains the radial dependence, and the angular dependence is contained in the spherical harmonics $Y_{l,m}(\theta, \phi) = P_l^m(\cos\theta)e^{im\phi}$, with $P_l^m(\cos\theta)$ the associated Legendre polynomial of degree l and order m.

The first correction to this simple Hamiltonian $\hat{H}_0$, comes from relativistic effects, which lead to lifting of the n^2-fold degeneracy. These relativistic corrections determine a splitting of the energy levels called *fine structure*. Among this effects, particularly relevant is the one coming from the coupling of the spin of the electron s with the electron's orbital degrees of freedom. Indeed, the interaction of the electron's spin with the internal magnetic field of the atom due to the electron orbiting the nucleus gives rise to the so-called spin-orbit coupling, which contributes to the total Hamiltonian with a term $\hat{H}_{SO} = A_{SO}\hat{L}\cdot\hat{S}$, where $\hat{S}$ is the electron spin operator, and A_{SO} is a constant. Under the spin-orbit coupling, L_z (and S_z) are no longer good quantum numbers, and one introduces the total angular momentum operator $\hat{J}$, defined by $\hat{J} = \hat{L}+\hat{S}$ to label the fine structure states via the quantum numbers J^2, J_z.

A further refinement of the atomic energy level structure comes from the interaction of the nuclear spin $\hat{I}$ with the total angular momentum of the electron $\hat{J}$, defined as the *hyperfine interaction*. The hyperfine coupling enters the total Hamiltonian with a term $\hat{H}_{HF} = A_{HF}\hat{I}\cdot\hat{J}$, where A_{HF} is a constant. In presence of both the spin-orbit coupling and the hyperfine interaction, the appropriate conserved quantum number is the total angular momentum $\hat{F}$ given by $\hat{F} = \hat{I} + \hat{J}$. Typically, the energy level splitting in the fine structure is on the order of 10^{-4} - 10^{-5} eV, and in the hyperfine structure of 10^{-7} - 10^{-8} eV [40].

The above described corrections to the Hamiltonian $\hat{H}_0$ have to be taken into account in order to correctly describe even the single-electron hydrogen atom. For multi-electron atoms, an additional effect that need to be considered is the Coulomb interaction between the electrons, leading to a screening of the nuclear charge by the inner shell electrons. Electronic states further from the nucleus experience a greater screening effect, and therefore, for a fixed principal quantum number n, large l states are less deeply bound than small l states, and lie at higher energy. Thus, each shell, indexed by n, is divided into subshells, indexed by the orbital angular momentum quantum number l. The electron orbitals in a subshell are then indexed by the angular momentum projection quantum number $m_l = -l, ..., l$ and, according to the Pauli exclusion principle, at most two electrons with opposite spin projection quantum number m_s can occupy the same orbital. The distribution of the electrons among the electron orbitals (i.e. the electron con-

Element	Electron configuration	Isotopes	Abundance (%)	Nuclear spin	Statistics
K	$1s^2 2s^2 2p^6 3s^2 3p^6 4s^1$	**^{39}K**	**93.26**	**3/2**	**boson**
		^{40}K	0.01	4	fermion
		^{41}K	6.73	3/2	boson
Er	[Xe]$4f^{12}6s^2$	^{162}Er	0.14	0	boson
		^{164}Er	1.6	0	boson
		^{166}Er	**33.5**	**0**	**boson**
		^{167}Er	22.86	7/2	fermion
		^{168}Er	26.9	0	boson
		^{170}Er	15.0	0	boson

Table 1.1: Some relevant properties of K and Er. The two isotopes ^{39}K and ^{166}Er in bold in the table are the ones used in the work of this thesis. In the electron configuration of Er, [Xe] indicates the electron configuration of xenon: [Xe] = $1s^2 2s^2 2p^6 3s^2 3p^6 3d^{10} 4s^2 4p^6 4d^{10} 5s^2 5p^6$. Note that for Er, all bosonic isotopes have zero nuclear spin, therefore they do not possess a hyperfine structure. The data for the isotopic composition and relative abundances for the two species are taken from [41].

figuration) of an atomic element in its ground state is determined by the Aufbau principle, which regulates the order of filling of the orbitals, starting from the one with lowest energy.

Let us consider specifically the two atomic elements of interest for this thesis: potassium (K) and erbium (Er). The ground-state electron configuration of K and Er are reported in Table 1.1, together with other relevant atomic properties. There, the standard spectroscopic notation nl^e for the electron configuration has been used, where n is the principal quantum number, the orbital quantum number l is denoted by the letter s if $l = 0$, p if $l = 1$, d if $l = 2$, f if $l = 3$, ..., and finally e indicates the number of electrons in the nl subshell.

Potassium (K) [42] Potassium is an alkali-metal atom, with atomic number $Z_K = 19$, and an atomic mass of ≈ 39 amu, with 1 amu $\simeq 1.66 \times 10^{-27}$ kg. Its ground-state electronic structure is characterized by all electrons but one occupying closed shells, and the remaining valence electron occupying an s orbital in a higher shell. Since the core is a closed shell, the only contribution to the total orbital

angular momentum comes from the valence electron, whose state is completely determined by the orbital quantum number L and the spin quantum number S. In the ground state $L = 0$, and the nuclear spin I is coupled to the electronic spin by the hyperfine interaction. Since $S = 1/2$, the hyperfine coupling yelds the two possibilities $F = I \pm 1/2$ for the quantum number F for the total spin. For alkali-metal atoms the electronic states are typically specified in the Russel-Saunders notation, as $n^{(2S+1)}L_J$, where n is the principal quantum number of the valence electron. The ground state of K is then written as

$$\text{K ground state:} \qquad 4^2\mathrm{S}_{1/2} \qquad (L = 0, S = 1/2, J = 1/2). \tag{1.2}$$

For an excited state with $L = 1$, and $S = 1/2$, one has $J = 1/2$ or $J = 3/2$, corresponding to the states $4^2\mathrm{P}_{1/2}$ or $4^2\mathrm{P}_{3/2}$, respectively. The fine structure interaction lifts the degeneracy of the $4^2\mathrm{P}_{1/2}$ and $4^2\mathrm{P}_{3/2}$ levels, splitting the spectral lines in the so-called D_1 line ($4^2\mathrm{S}_{1/2} \rightarrow 4^2\mathrm{P}_{1/2}$), with a wavelength of the transition of 770 nm, and D_2 line ($4^2\mathrm{S}_{1/2} \rightarrow 4^2\mathrm{P}_{3/2}$), with a wavelength of 767 nm, which are typically used for laser cooling in experiments (see below and Chapter 3).

Erbium (Er) [43] Erbium is a rare-earth element belonging to the lanthanide series of the periodic table. It has an atomic number $Z_{Er} = 68$, and atomic mass of ≈ 167 amu. Its ground-state electron configuration (see Table 1.1) forms a so-called submerged-shell structure, with all orbitals, except the $4f$, completely filled. In the case of erbium, there are two electron vacancies in the $4f$ orbitals, immersed in a completely filled outer-lying $6s$ shell, and they have an angular momentum projection quantum number of $m_l = +2$ and $+3$. Due to their large orbital angular momentum quantum number $l = 3$, the $4f$ orbitals are highly anisotropic. This anisotropy is at the origin of strongly anisotropic van der Waals interaction potentials (see section 2.1) between Er atoms, which are not observed with alkali atoms. This has consequences on their scattering properties, and in particular on the Feshbach resonances, as will be discussed in Chapter 2.4.

In the case of Er, and in general for heavy atoms, the coupling of electrons is more complicated than for K, or lighter atoms. The reason is that the spin-orbit interaction becomes comparable or even stronger than the Coulomb interaction

for electrons in higher orbitals. Thus, the previously described spin-orbit coupling scheme of electrons is not applicable any more and one has to use the so-called *jj-coupling* scheme, where the total atomic Hamiltonian commutes both with $\hat{J}^2$ (as in the standard spin-orbit coupling), and with $\hat{J}_i^2$ for each electron i. In this case the electronic states are usually specified in the ${}^{(2S+1)}L_J$ notation, and the ground state of Er is given by:

$$\text{Er ground state:} \qquad {}^3\mathrm{H}_6 \qquad (L = 5, S = 1, J = 6). \tag{1.3}$$

Note the large orbital angular momentum quantum number $L = 5$, due to the spin-orbit coupling of all electrons, with respect to the $L = 0$ of K in its ground state. The large angular momentum of Er, originating from the characteristic electron configuration, determines a peculiar property of this atomic species, that is a high magnetic moment of 7 Bohr magneton (compared to a magnetic moment of ≈ 1 Bohr magneton for alkali). This property of Er opens the possibility of studying effects of the magnetic dipole-dipole interaction experimentally with this system, as will be shown in Chapter 4.

Laser cooling of Er atoms is typically performed on atomic transitions from the ground state $J = 6$ to an excited state $J = 7$ [44]. In the experiment described in Chapter 4, two such transitions are used: $[Xe]4f^{12}({}^3\mathrm{H}_6) \rightarrow 6s6p({}^1\mathrm{P}_1)$, at a wavelength of 401 nm, and $[Xe]4f^{12}({}^3\mathrm{H}_6) \rightarrow 6s6p({}^3\mathrm{P}_1)$ at 583 nm [43].

1.2.2 Interaction with static external magnetic fields

In the presence of an external magnetic field $\mathbf{B}$, the atomic energy levels shift according to the Zeeman effect. This effect arises from the interaction of the magnetic moments of the electron and the nucleus with the magnetic field. For low values of the magnetic field, for which the Zeeman effect can be treated as a perturbation of the fine and hyperfine interactions, F and m_F are still good quantum numbers, and the total Hamiltonian acquires a term of the form $\hat{H}_B = \mu_B g_F \hat{F} \cdot \mathbf{B}$. Here, μ_B is the Bohr magneton, and g_F is the Landé-g factor for an atom with a non-zero nuclear spin, given by:

$$g_F = g_J \frac{F(F+1) + J(J+1) - I(I+1)}{2F(F+1)}, \tag{1.4}$$

with

$$g_J = 1 + \frac{J(J+1) + S(S+1) - L(L+1)}{2J(J+1)} \tag{1.5}$$

the Landé-g factor associated with the electron spin [40]. Assuming that the magnetic field is oriented along the z direction, the Zeeman energy shift ΔE_z is proportional to the applied magnetic field according to the relation:

$$\Delta E_z = \mu_B g_F m_F B_z. \tag{1.6}$$

Eq.(1.6) holds in typical ultracold atomic experiments, where the Zeeman energy splitting is much smaller than the hyperfine splitting. If stronger magnetic fields are applied, in first approximation the energy shift turns out to be quadratic in the magnetic field (quadratic Zeeman effect, see ref. [40]).

1.2.3 Atom-light interaction

Let us consider now the interaction of an atom with a light field. To describe the atom-light interaction I will make use of a well estabilished semi-classical description [45], where the internal state of the atom is treated in a fully quantum mechanical way, while the external degrees of freedom of the atom (its position and momentum), as well as the light field, are treated classically. Moreover, the atom is approximated to have only two-levels. This is valid when the external field is weak and nearly resonant with a single atomic transition. Indeed, in this case only the ground state and the near-resonant excited level, indicated by $|g\rangle$ and $|e\rangle$, respectively, have a relevant probability of occupation. Let $\hbar\omega$ be the energy difference between $|g\rangle$ and $|e\rangle$. We consider the evolution of this system when illuminated by a classical nearly-monochromatic laser beam with electic field $\mathbf{E}$ of the form:

$$\mathbf{E}(\mathbf{r}, t) = \epsilon(\mathbf{r}) \frac{E(\mathbf{r})}{2} e^{-i(\omega_L t - \phi(\mathbf{r}))} + c.c., \tag{1.7}$$

where ϵ is the polarization unit vector, E the field amplitude, ω_L the angular frequency and ϕ the phase. The interaction Hamiltonian can be expressed in the so-called *dipole approximation*, as:

$$\hat{V}_{AL} = -\hat{\mathbf{D}} \cdot \mathbf{E}(\mathbf{r}, t), \tag{1.8}$$

where $\hat{\mathbf{D}}$ is the atomic dipole moment operator, given by:

$$\hat{\mathbf{D}} = \mathbf{d}_{eg}(|e\rangle\langle g| + |g\rangle\langle e|) \tag{1.9}$$

with $\mathbf{d}_{eg}$ the dipole transition matrix element beetween the ground and excited states. By inserting Eq.(1.7) into Eq.(1.8), one obtains two contributions to the interaction Hamiltonian. The first one oscillates at a frequency equal to the difference between the laser frequnecy ω_L and the atomic transition frequency ω, defined as the laser *detuning*, and indicated by

$$\delta = \omega_L - \omega, \tag{1.10}$$

and its amplitude is proportional to $1/\delta$. The second contribution oscillates at a frequency which equals the sum of ω_L and ω, with an amplitude inversely proportional to that sum. In most situations encountered in the experiments, the laser fields are near resonant with the atomic transitions under consideration, and one can safely ignore the rapidly oscillating, or "counterrotating", term with frequency $\sim (\omega_L + \omega)$. This is the so-called *rotating-wave approximation* (RWA). Under the RWA, the interaction Hamiltonian (1.8) takes the form:

$$\hat{V}_{AL} \simeq \frac{\hbar}{2}\Omega_R(\mathbf{r}) \left(e^{-i\phi(\mathbf{r})-i\omega_L t}|e\rangle\langle g| + h.c.\right), \tag{1.11}$$

where Ω_R is the *Rabi frequency*, defined as:

$$\Omega_R(\mathbf{r}) \equiv -\frac{E(\mathbf{r})\mathbf{d}_{eg} \cdot \epsilon(\mathbf{r})}{\hbar}. \tag{1.12}$$

The internal two-level atom dynamics under the effect of $\hat{V}_{AL}$ can be properly described by the optical Bloch equations (OBEs) for the atomic density matrix operator $\hat{\rho}$ (see, for instance, ref. [40]). For a nearly-resonant laser field, it

can be demonstrated that the state of the atom oscillates in between $|g\rangle$ and a superposition of $|g\rangle$ and $|e\rangle$, at a rate given by the generalized Rabi frequency $\Omega \equiv \sqrt{\Omega_R^2 + \delta^2}$. To correctly describe the dynamics of the internal state of the atom, in the OBEs one has to add to the interaction Hamiltonian (1.11) a phenomenological relaxation term describing the spontaneous emission process from the excited to the ground state, occurring at a rate [40]

$$\Gamma_{spont} = \frac{\Gamma}{2} \frac{s(\mathbf{r})}{1 + s(\mathbf{r})}, \tag{1.13}$$

where $\Gamma = 2\pi/\tau$ is the decay rate of the excited state $|e\rangle$, whose radiative lifetime is indicated by τ, and $s(\mathbf{r})$ is the saturation parameter, defined as:

$$s(\mathbf{r}) = \frac{\Omega_R^2(\mathbf{r})/2}{\delta^2 + \Gamma^2/4}. \tag{1.14}$$

Mean forces exerted by light on an atom at rest The concept of a mean light force $\mathbf{F}(\mathbf{r})$ acting on an atom at position $\mathbf{r}$, due to transfer of momentum ($\mathbf{F} = \langle d\mathbf{p}/dt \rangle$), is valid only if the atomic wavepacket is well-localized in position and momentum space during the interaction with light, compatibly with Heisenberg uncertainty principle [45]. The two constraints on atomic position and momentum reads, respectively: $\Delta x \ll \lambda_L$, where Δx is given in the ultracold regime by the De Broglie wavelength, and $\lambda_L = 2\pi/k_L$ is the laser wavelength, and $k_L \Delta p/m \ll \Gamma$. By writing the Heisenberg uncertainty principle for the conjugated variables of the atomic motion and making use of the above conditions, one obtains the following relation:

$$\frac{\hbar\Gamma}{2} \gg \frac{\hbar^2 k_L^2}{2m}. \tag{1.15}$$

The right-hand side of Eq.(1.15) expresses the so-called kinetic recoil energy $E_{rec} = \hbar^2 k_L^2/2m$, associated with the transfer of momentum that an atom gets from the light field in an absorption event. Eq.(1.15) is also known as the "large linewidth condition" [45], and insures that the interaction with the light field does

not change significantly the atomic energy over many absorption-emission cycles. For instance, for the cooling transition typically used with ^{39}K, the ratio $\Gamma\hbar/2E_{rec}$ is about 350, and the large linewidth condition is satisfied.

Under this condition, the mean force exerted on an atom at position $\mathbf{r}$ by a nearly-resonant laser field can be calculated as:

$$\mathbf{F}(\mathbf{r},t) = -\langle \nabla \hat{V}_{AL}(\mathbf{r},t)\rangle \equiv -\mathrm{Tr}\ \{\hat{\rho}_{st}\nabla \hat{V}_{AL}(\mathbf{r},t)\}, \tag{1.16}$$

where $\hat{\rho}_{st}$ represents the steady state solution of the OBEs for the density matrix $\hat{\rho}$. In the simple case of a two-level atom at rest, the mean force has two contributions: a dissipative, or *radiation pressure force* and a reactive, or *dipole force*. The radiation pressure force is expressed by:

$$\mathbf{F}_{rad}(\mathbf{r}) = -\frac{\hbar\Gamma}{2}\frac{s(\mathbf{r})}{1+s(\mathbf{r})}\nabla\phi(\mathbf{r}). \tag{1.17}$$

It is proportional to the phase gradient of the laser field. The dipole force is instead given by:

$$\mathbf{F}_{dip}(\mathbf{r}) = -\hbar\delta\frac{s(\mathbf{r})}{1+s(\mathbf{r})}\frac{\nabla\Omega_R(\mathbf{r})}{\Omega_R(\mathbf{r})}, \tag{1.18}$$

and is proportional to the amplitude gradient of the laser field.

Let us discuss these two forces in more details. If the light field is a single plane wave, with $\phi = -\mathbf{k}_L\cdot\mathbf{r}$, and constant field amplitude, the radiation pressure force takes the form:

$$\mathbf{F}_{rad}(\mathbf{r}) = \hbar\mathbf{k}_L\frac{\Gamma}{2}\frac{s(\mathbf{r})}{1+s(\mathbf{r})}. \tag{1.19}$$

For very high intensity of the laser field, $s \gg 1$, $\mathbf{F}_{rad} \to \hbar\mathbf{k}_L\Gamma/2$. This force can be interpreted as due to scattering of photons at a rate $\frac{\Gamma}{2}\frac{s(\mathbf{r})}{1+s(\mathbf{r})}$, which is exactly the spontaneous emission rate Γ_{spont} introduced in Eq.(1.13). The radiation pressure force thus accounts for absorption-spontaneous emission cycles. When a photon is absorbed, it changes the atom momentum by $\hbar\mathbf{k}_L$ in the direction of the incoming photon. After the absorption of a photon, the energy of the atom is almost entirely converted into internal energy, therefore the atom ends up in an excited state.

Then, the atom returns to the ground state by spontaneously emitting a photon. The conservation of momentum in this process causes the atom to recoil again, but this time, the direction is opposite to that of the emitted photon. However, since spontaneous emission occurs in a random direction, it does not contribute to the net change in the momentum of the atom when averaged over many absorption-spontaneous emission cycles. The radiation pressure force plays a fundamental role in the Doppler cooling of atomic samples, as will be discussed in section 1.3.2.

In contrast to the dissipative force, the dipole force is zero for an incident plane wave, since it does not present any field amplitude gradient. To have a non-zero dipole force, it is necessary to have a spatially varying field amplitude. This force originates from the interaction of the induced atomic electric dipole moment with the intensity gradient of a light field, and it can be interpreted as due to the exchange and redistribution of momentum between the atom and the various plane waves composing the laser field, that an atom can operate by absorbing a photon from one plane wave and emitting it by stimulated emission in another one. The dipole force (1.18) can be derived from a potential of the form:

$$U_{dip}(\mathbf{r}) = \frac{\hbar\delta}{2}\ln(1 + s(\mathbf{r})). \tag{1.20}$$

This force is thus conservative, and can be used for atom trapping in a so-called *optical dipole trap*, which will be discussed in section 1.3.4. For a negative detuning δ (*red-detuned* laser field), the dipole potential (1.20) attracts the atoms towards the maxima of the laser field intensity, instead for a positive δ (*blue-detuned* laser field), the atoms are repelled from the region of maximum intensity of the field, and they are instead attracted towards the intensity minima.

1.3 Experimental techniques to realize Bose-Einstein condensation in dilute gases

In order to create a Bose-Einstein condensate in a dilute gas, atoms must be cooled and compressed in a trap until their thermal de Broglie wavelength is on the order of the interatomic distance. In addition, the atoms must be thermally isolated from all material walls. This is done by trapping atoms with laser light or

magnetic fields inside ultrahigh vacuum chambers, where the background pressure can be made as low as $\sim 10^{-11}$ mbar . Such traps can store atoms for seconds or even minutes, which is enough time to cool them.

The two basic techniques used to reach low temperatures in dilute atomic gases are *laser cooling* and *evaporative cooling*. Laser cooling allows to cool a gas from room temperature down to a few μK, and it is typically used as a pre-cooling stage. Evaporative cooling is instead used to reach the few hundreds of nK that are necessary to achieve the BEC transition.

In typical ultracold atomic experiments, the starting point is an atomic vapour, from which an atomic beam in produced, and pre-cooled by using laser cooling techniques. The pre-cooled atoms are then confined in conservative traps, where evaporative cooling allows to reach degeneracy. In the following I will present the fundamental techniques used to produce a quantum gas in the laboratory. A full account of these techniques can be found, for instance, in [46].

1.3.1 Atom sources

The most common atom sources for ultracold atom experiments are vapour cells and effusive ovens. In a vapour cell, an atomic trap is loaded from background gas. Higher background gas pressures result in faster loading rates, but above a certain optimum pressure, losses due to collisions with the background gas increase as fast as the loading rate. Effusive ovens consist of a reservoir vacuum chamber in which the desired species is stored in solid or liquid form, and is in equilibrium with its vapour. The vapour effuses through a small opening toward the experiment. The atomic flux can be controlled by changing the oven temperature and thus the equilibrium vapour pressure in the reservoir.

The choice of the atom source depends essentially on the properties of the used atomic species, in particular the melting point. For Er, which has a high melting point at 1529 °C, a high-temperature oven is used as atom source (see Chapter 4), while for K, with a much lower melting point at around 64 °C, vapour cells are typically used. The atomic vapour is either released from current driven dispensers mounted inside the vacuum apparatus, or it can be obtained by simply heating a solid sample, also placed under vacuum (see, for instance, [47]). This latter

strategy is the one we want to adopt in the new experimental apparatus described in Chapter 3.

1.3.2 Laser cooling

The radiation pressure force exerted by a nearly-resonant laser field on a two-level atom at rest at position $\mathbf{r}$ has been introduced in section 1.2.3. By substituting the definition of the saturation intensity (1.14) into Eq.(1.17), one obtains an expression for the radiation pressure force in terms of the laser detuning $\delta = \omega_L - \omega$, of the form:

$$\mathbf{F}_{rad}(\mathbf{r}) = \hbar \mathbf{k_L} \frac{\Gamma}{2} \left(\frac{\Omega_R^2(\mathbf{r})/2}{\delta^2 + \Gamma^2/4 + \Omega_R^2(\mathbf{r})/2} \right). \tag{1.21}$$

Now, if the atom is moving with velocity $\mathbf{v}$, the effective frequency of the light field that the atom sees is modified by the Doppler effect. Therefore, the detuning entering in the expression of the radiation pressure force is Doppler shifted according to:

$$\delta' = \delta - \mathbf{k_L} \cdot \mathbf{v}.$$

The radiation pressure force now depends on the atomic velocity through δ':

$$\mathbf{F}_{rad}(\mathbf{v}) = \hbar \mathbf{k_L} \frac{\Gamma}{2} \left(\frac{\Omega_R^2/2}{\delta'^2 + \Gamma^2/4 + \Omega_R^2/2} \right). \tag{1.22}$$

In the low velocity limit, that is if $|2\delta \mathbf{k_L} \cdot \mathbf{v}| \ll \delta^2 + \Gamma^2/4 + \Omega_R^2/2$, terms in v^2 can be neglected, and the expression of the force can be linearized around $\mathbf{v} = 0$:

$$\mathbf{F}_{rad}(\mathbf{v}) \simeq \hbar \mathbf{k_L} \left(\frac{\Gamma}{2} \frac{\Omega_R^2/2}{\delta^2 + \Gamma^2/4 + \Omega_R^2/2} \right) + \hbar (\mathbf{k_L} \cdot \mathbf{v}) \mathbf{k_L} \delta\Gamma \left(\frac{\Omega_R^2/2}{(\delta + \Gamma^2/4 + \Omega_R^2/2)^2} \right). \tag{1.23}$$

The first term is the force for zero velocity. The second term is proportional to the component of the velocity in the direction of the laser.

Let us now consider the simple one-dimensional (1D) scenario where the laser beam is counterpropagating with respect to the atomic motion. This means ($\mathbf{k_L} \cdot$

$\mathbf{v})\mathbf{k_L} = -k_L^2\mathbf{v}$. Therefore, in the linear approximation, the radiative pressure force is given by:

$$F_{rad}(v) \simeq F_{rad}(v=0) - \alpha v, \tag{1.24}$$

with

$$\alpha = -\hbar k_L^2 \Gamma \left[\frac{\delta \Omega_R^2/2}{(\delta^2 + \Gamma^2/4 + \Omega_R^2/2)^2} \right]. \tag{1.25}$$

The last term in the expression of the force (1.24) is a *friction force*, opposite to the direction of the atomic velocity, as long as the *friction coefficient* α is positive. According to Eq.(1.25), $\alpha > 0$ for $\delta < 0$, that is for a red-detuned laser light. As the Doppler effect plays a central role, this cooling scheme is typically referred to as *Doppler cooling*.

Zeeman slower In the previous section we have seen that a red-detuned laser light can decelerate an atom moving towards it. This is the principle at the basis of the operation of a *Zeeman slower*. A Zeeman slower is typically used in ultracold atomic experiments to reduce the longitudinal velocity of an atomic beam coming from the atom source. A laser beam is shined collinearly to the atomic beam, in the counterpropagating direction with respect to it. The Doppler shift of the atoms changes as the velocity of the atoms is reduced during the slowing process. In order to keep the atoms constantly on resonance with the light, one exploits the Zeeman shift of the energy levels in a magnetic field (see section 1.2.2). Indeed, a proper configuration of magnetic coils creates an inhomogeneous magnetic field leading to a position-dependent Zeeman shift of the atomic resonances, which compensates the position-dependent Doppler shift. The Zeeman slower provides an efficient reduction of the longitudinal velocity of the atoms if their initial velocity is below a maximum value, known as *capture velocity*. The capture velocity of a Zeeman slower depends on the actual deceleration acting on the atoms while travelling the Zeeman slower, and on the length of the Zeeman slower itself, that is the spatial extension of the region where the moving atoms are kept on resonance with the counterpropagating light field. In the ERBIUM experiment described in

Chapter 4, erbium atoms with an initial velocity smaller than 325 m/s are slowed down to a velocity of about 8 m/s in the Zeeman slower [43].

Optical molasses Eq.(1.24) shows that a single laser beam directed oppositely to an atomic beam, can not cool the atoms as the main component of the force is given by the zero order term $F_{rad}(v = 0)$, which accelerates the atoms in the direction of the laser, regardless of the (small) atomic velocity. For neutral atoms, the idea for eliminating the velocity-independent term consists of using two counterpropagating laser beams, instead of a single one, with wavevectors $\mathbf{k_L}$ and $\mathbf{k_L'} = -\mathbf{k_L}$, both with the same frequency, tuned slightly below an atomic absorption line (red-detuned light)[48]. Because of the Doppler effect, the atom sees the light it moves towards Doppler shifted closer to resonance, whereas the light it moves away appears further from resonance. Thus, the atom predominantly scatters photons from the counter-propagating laser, which exerts a stronger force with respect to the co-propagating wave. This situation is sketched in Fig.1.1(b). For weak intensities of the laser fields ($s(\mathbf{r}) \ll 1$), the two radiation pressure forces of the two lasers add independently. In the 1D case, the total radiation pressure force thus reads:

$$F_{rad}(v) \simeq -2\alpha v. \tag{1.26}$$

Eq.(1.26) describes the motion of a particle in a viscous medium, which was reasonably called *optical molasses*. This configuration can be generalized to three dimensions by using three mutually orthogonal, intersecting pairs of counterpropagating laser beams. In the intersection region, the atoms feel a laser cooling damping force in all directions (3D optical molasses, see Fig.1.1(c)). The velocity range over which the linear approximation of the radiation pressure force remains valid (velocity capture range) is given by $|\mathbf{k_L} \cdot \mathbf{v}| \ll \Gamma/2$, that is satisfied if the semiclassical picture is applicable (i.e. if Eq.(1.15) is valid).

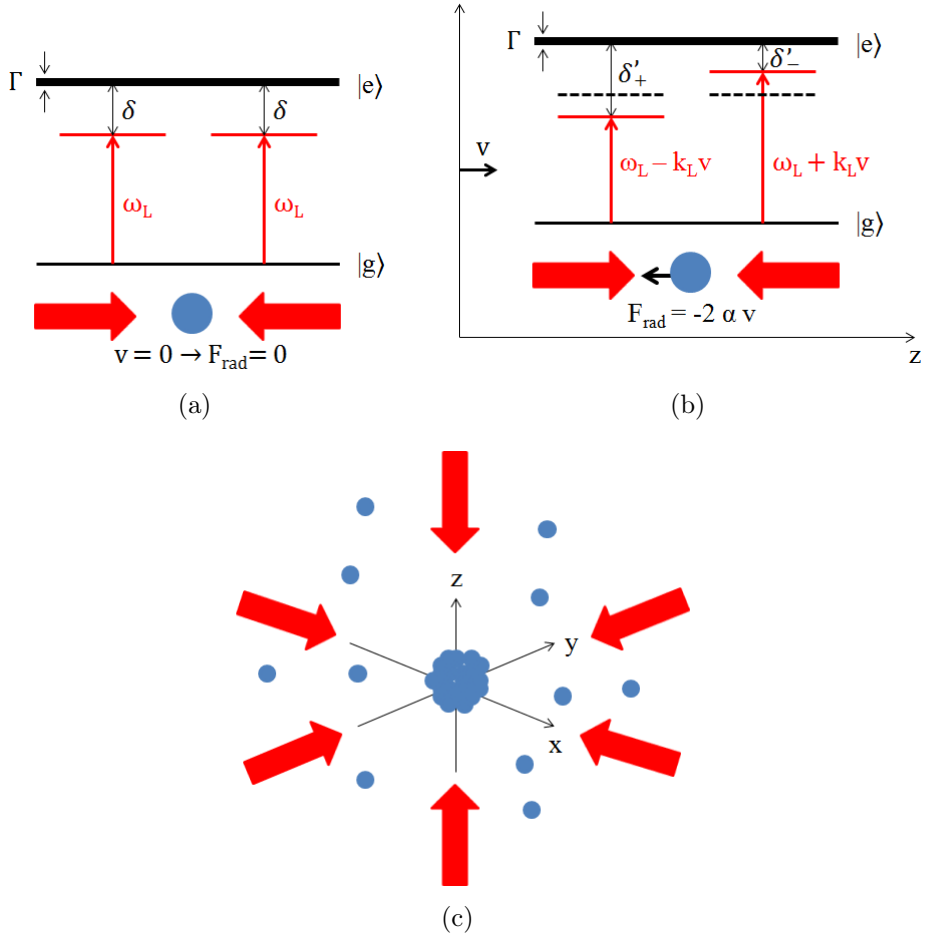

Figure 1.1: Optical molasses. In 1D, an atom at rest, subjected to two counterpropagating laser beams, red-detuned with respect to an atomic resonance, does not feel any force due to the cancellation of the radiation pressure forces exterted by the two laser fields **(a)**. $|g\rangle$ and $|e\rangle$ are the ground and excited state, respectively. **(b)** If the atom has a finite velocity $v \neq 0$, the Doppler effect leads to a dominant strength of the radiation pressure force exerted by the laser propagating in the direction opposite to the atom. This gives rise to a friction force which slows down the atom (1D optical molasses). In the figure, $\delta'_{\pm} = \delta \pm k_L v$ indicate the effective laser detunings of the two beams, which are Doppler shifted. The situation is represented in the reference frame of the atom moving with velocity v. **(c)** 3D configuration of an optical molasses. The laser beams intersect at the centre of the coordinate axes, creating a viscous medium for the atoms. Due to the random nature of the absorption and re-emission processes characteristic of laser cooling, the atoms can still diffuse around, and eventually escape from the molasses.

1.3.3 Magneto-optical trap

The optical molasses introduced in the previous section does not constitute a trap, but rather a viscous medium. It allows to gather a sample of cold atoms in the intersection region of the counterpropagating laser beams, but the atoms are free to diffuse around: they eventually reach the surface of the intersection region of the lasers, and escape. In order to confine the atoms in a certain spatial region, it is necessary to have a position dependent force, directed towards the center of the trap. The required restoring force can be obtained by combining a optical molasses configuration with a magnetic field gradient. This is realized in the so-called magneto-optical trap (MOT), where an inhomogeneous magnetic field modifies the radiation pressure force through the Zeeman effect. In a MOT, a magnetic field gradient created by a pair of magnetic coils in anti-Helmohltz configuration (i.e. with the current circulating in opposite directions) causes an imbalance between the radiation pressure forces due to two counterpropagating laser beams. The imbalance depends on the position of the atom with respect to the *magnetic* center of the trap (where the magnetic field is zero).

Fig.1.2 shows the working principle of a 1D MOT, with the counterpropagating laser beams and the axis of the pair of coils both along the z-axis. Here we consider an atomic transition $J = 0 \rightarrow J = 1$, as an example. At the center of the coils, the magnetic fields produced by the two coils cancel out, therefore $B(z = 0) = 0$. Close to the center, the inhomogeneity of the magnetic field $B(z) = bz$ gives rise to a uniform magnetic field gradient $b = dB(z)/dz$.

The Zeeman shift for the three sublevels $m_J = 0, \pm 1$ of the excited state $J = 1$ is linear along z and given by $\Delta E(z) = g_J m_J \mu_B B(z)$ (see section 1.2.2). Thus, the state $m_J = +1$ is shifted upwards for $z > 0$, and downwards for $z < 0$, since the magnetic field is in the opposite direction. The situation is inverted for the $m_J = -1$ state. The relative shift of the resonance frequency is given by:

$$\omega(z) = \omega(z = 0) + \frac{\Delta E(z)}{\hbar} = \omega + \frac{\Delta E(z)}{\hbar}. \tag{1.27}$$

Two counterpropagating laser beams with opposite circular polarizations σ^+ and σ^-, both red-detuned by the same amount with respect to the atomic resonance at the center of the trap, are in resonance with the atom at different places

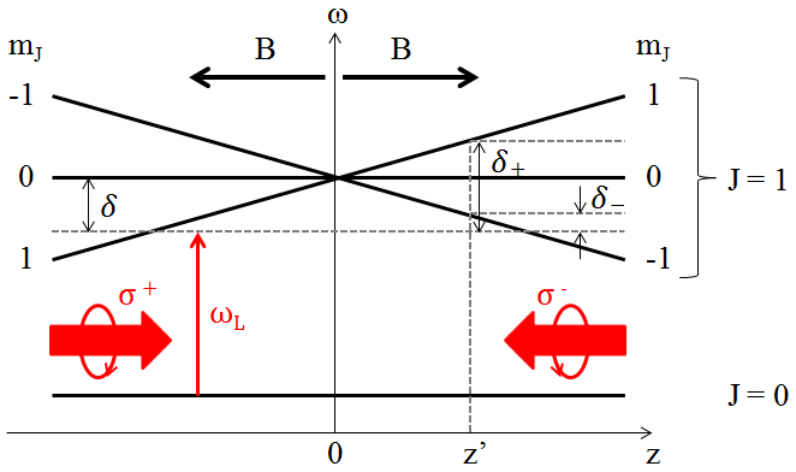

Figure 1.2: Working principle of a 1D MOT on a $J = 0 \rightarrow J = 1$ transition. The picture is not in scale: the Zeeman shift is typically much smaller than the energy of the atomic transition.

along z. Indeed, for an atom at a position $z' > 0$ along the z-axis, the magnetic field causes a shift of the $\Delta m_J = -1$ transition closer to resonance, while the $\Delta m_J = +1$ is shifted farther from resonance, compared to the situation experienced by an atom at the trap center $z = 0$. This means that the atom absorbs more likely a photon from the laser beam coming from right, which is σ^- polarized, than from the σ^+-polarized laser beam coming from left. Therefore the net radiation pressure force for an atom at position $z' > 0$ pushes the atom towards the center of the trap. For an atom at a position $z' < 0$, the shift of the states $m_J = \pm 1$ is reversed, and the atom interact more likely with the laser beam coming from left, such that the resulting force also points towards the center. One therefore achieves a stable trapping around $z = 0$.

In 1D the calculation of the force experienced by an atom in a MOT is carried out in the same manner as in section 1.3.2 for the frictional force in a 1D optical molasses configuration, taking into account the Zeeman shift of the atomic levels. Let us consider the radiation pressure force given in Eq.(1.22). The total force on an atom moving along the z-axis is given by the sum of the forces exerted by the two laser beams:

$$F_{MOT} = F_{rad}^{\sigma^+}(\delta_-) + F_{rad}^{\sigma^-}(\delta_+), \tag{1.28}$$

where the detuning $\delta_\pm$ for the $\sigma^\mp$-polarized laser beams, respectively, is now a function of z:

$$\delta_\pm = \delta \pm k_L v \pm \frac{g_J \mu_B b z}{\hbar}, \tag{1.29}$$

with δ defined as usual, $\delta = \omega_L - \omega$. The δ_+ term is the detuning with respect to the $\delta m_J = +1$ transition, and the δ_- is the one for the $\delta m_J = +1$ transition.

When both the Doppler shift and the Zeeman shift are small compared to the detuning δ ($k_L v$, $g_J \mu_B b z/\hbar \ll \delta$), the force can be expanded around $v = 0$ and $z = 0$. Thus Eq.(1.28) becomes:

$$F_{MOT} \simeq -2\frac{\partial F_{rad}}{\partial \omega_L} k_L v + 2\frac{\partial F_{rad}}{\partial \omega}\frac{g_J \mu_B b z}{\hbar}. \tag{1.30}$$

Since $\partial F_{rad}/\partial \omega_L = -\partial F_{rad}/\partial \omega$, it is possible to express the force exerted in a MOT as follows:

$$F_{MOT} \simeq -\alpha' v - \kappa z, \tag{1.31}$$

where $\alpha' = 2\alpha$, with α the friction coefficient defined in Eq.(1.25), and κ representes the elastic costant, given by:

$$\kappa = \frac{g_J \mu_B b}{\hbar k_L}\alpha'. \tag{1.32}$$

From Eq.(1.31) one clearly sees that, in addition to the friction term, a restoring force arises from the Zeeman shift contribution. The red-detuning of the laser beams also provides cooling of the trapped atoms. Therefore, in a MOT the atoms can be simultaneously cooled and trapped.

Such a scheme can be extended to three dimensions, provided that other two pairs of mutually orthogonal counterpropagating laser beams are added, as shown in Fig.1.3. The magnetic quadrupole field produced by the coils in anti-Helmholtz configuration is zero at the centre of the trap, and its amplitude increases linearly for small distances to the centre. From Maxwell equation $\nabla \cdot \mathbf{B} = 0$, one gets:

$$\frac{dB_x}{dx} = \frac{dB_y}{dy} = -\frac{1}{2}\frac{dB_z}{dz}. \tag{1.33}$$

The magnetic field gradient in each radial direction is half the one along the axis of the coils [49]. Thus, the previously described trapping mechanism also works in each radial direction.

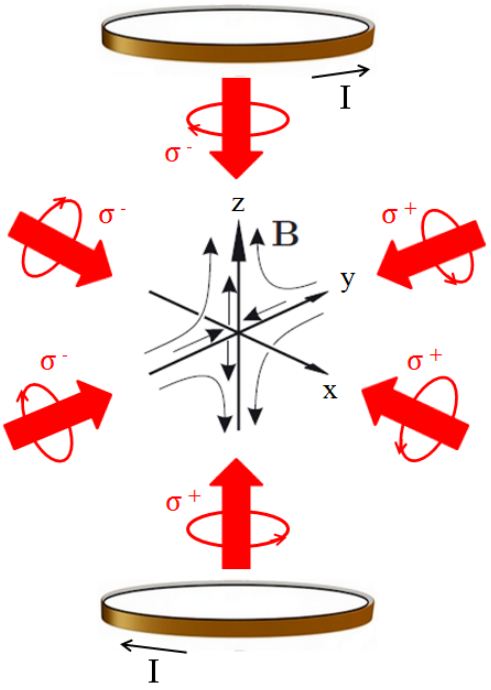

Figure 1.3: Sketch of a 3D MOT. A 3D MOT is composed of three pairs of mutually orthogonal counterpropagating laser beams, which intersecate at the centre of a pair of coils in anti-Helmholtz configuration. In each pair of laser beams, the two counterpropagating laser fields have a different circular polarization. The magnetic field is zero at the intersection point, and increases linearly in all spatial directions for small distances from the centre. In such a configuration of optical and magnetic fields, the atoms (not drown in the picture) feel a restoring force in all directions which pushes them towards the centre of the system, in addition to the friction force typical of an optical molasses. Thus, both cooling and trapping of the atoms are realized in this configuration.

2D MOT The two-dimensional magneto-optical trap configuration (2D MOT) deserves particular attention, since it is often used as a preliminar cooling and trapping stage in experiments using vapour cells as atom sources. In these systems, a 2D MOT is typically loaded from the background gas in order to produce an atomic beam out of the atomic vapour coming from the source. In fact, in a 2D MOT, the atoms are cooled and trapped in two orthogonal spatial directions, and are free to move in the third direction, thus forming an atomic beam. The atomic beam is then directed towards a region of the vacuum apparatus where a 3D MOT is performed. This technique is typically used in alternative to the Zeeman slower, to increase the efficiency of the loading in a 3D MOT. The use of the Zeeman slower or the 2D MOT depends crucially on the atomic species under consideration, and therefore on the type of atom source. In the case of Er, for instance, a Zeeman slower is necessary to decelerate the high speed atomic flux coming from the oven. In experiments with K, instead, the 2D MOT configuration is adopted, since a vapour cell is used as atom source (see also Chapter 3).

Limit temperature in Doppler cooling The minimum temperature of the atoms that can be achieved in a MOT, using Doppler cooling, can be estimated through the following argument. The equation describing the evolution of the atomic velocity in time within the semiclassical approach is Newton equation, given by:

$$m\frac{d\mathbf{v}}{dt} = -2\alpha\mathbf{v} \Longrightarrow \mathbf{v}(t) = \mathbf{v}(0)e^{-\gamma t}, \tag{1.34}$$

where $\gamma = 2\alpha/m$. In principle, after a time long as compared to γ^{-1} , the velocity should vanish, and the final temperature reach $T = 0$. However, this simple model neglects the random nature of the absorption and spontaneos emission processes, which cause fluctuations of the radiation pressure force in time. These fluctuations give rise to a diffusion in momentum space, and thus to heating of the atomic sample. The competition between cooling due to the friction force and this heating process due to fluctuations of the radiative force sets a lower limit on the width of the atomic velocity distribution, and consequently, a minimum finite temperature achievable with Doppler cooling.

In the simple 1D case, the damping force leads to a decreasing of the momentum dispersion:

$$\frac{dp}{dt} = -\frac{2\alpha}{m}p \Longrightarrow \left(\frac{d(\Delta p)^2}{dt}\right)_{cool} = -2\gamma(\Delta p)^2. \tag{1.35}$$

Since we search for the minimum temperature, let us assume that the friction coefficient is maximum: according to Eq.(1.25), $\alpha_{max} = 2\hbar k_L^2 s$ (obtained for $\Delta = -\Gamma/2$). Then, $\gamma = 2\alpha_{max}/m = 4\hbar k_L^2 s/m$. The diffusion of the atomic momentum along the laser beam axis originates from both the fluctuations in the number of absorbed photons during a given time interval, and from the fluctuations of the recoil momentum transferred by the fluorescence photons that are emitted in random directions: since the spontaneous emission occurs in a random direction, the atom experiences a random walk of step size $\hbar k_L$ in momentum space. Taking into account these two contributions, the fluctuation-dissipation theorem allows to write the rate of increase of the momentum dispersion due to heating in the following way:

$$\left(\frac{d(\Delta p)^2}{dt}\right)_{heat} = 2D. \tag{1.36}$$

where D is the diffusion coefficient. It can be demonstrated (see, for instance, [45]) that for two identical counterpropagating waves in the weak intensity regime ($s \ll 1$), the diffusion coefficient takes the value $D = \hbar^2 k_L^2 \Gamma s$.

The equilibrium condition for $(\Delta p)^2$ results from a trade-off between cooling and heating mechanism:

$$\left(\frac{d(\Delta p)^2}{dt}\right)_{cool} + \left(\frac{d(\Delta p)^2}{dt}\right)_{heat} = 0. \tag{1.37}$$

From Eq.(1.37) one finds: $(\Delta p)^2_{eq} = \hbar\Gamma m/2$. Since the equilibrium temperature is defined as $\frac{1}{2}k_B T = \frac{1}{2}\frac{(\Delta p)^2_{eq}}{m}$, where k_B is the Boltzmann constant, it is possible to determine the minimum temperature T_D achievable with Doppler cooling, which is called *Doppler temperature*:

$$k_B T_D = \frac{\hbar\Gamma}{2}. \tag{1.38}$$

As one can see from Eq.(1.38), the Doppler temperature depends on the linewidth of the atomic transition employed for cooling, and it is lower for a narrower transition. For instance, the typical transition used for cooling K in the MOT, the D_2 line, has a linewidth of $\approx 2\pi\times 6$ MHz, which gives a Doppler temperature of $T_D(\mathrm{K}) \simeq 145\mu K$ [47]. In the case of Er, the MOT is operated on a transition with a narrow linewidth of $2\pi\times 190$ kHz, providing a Doppler temperature of $T_D(\mathrm{Er}) = 4.6\mu K$ [50].

It is worth noticing that the Doppler temperature is not the lowest temperature achievable in a MOT. Atomic samples with a multilevel ground state can be cooled below the Doppler limit in presence of a non homogeneous polarization of the light field [51]. This technique, named *Sysiphus cooling*, allows to reach the ultimate limit, given by the *recoil temperature* T_{rec}, defined as:

$$\frac{1}{2}k_B T_{rec} = E_{rec}, \tag{1.39}$$

where E_{rec} is the recoil kinetic energy introduced in Eq.(1.15).

1.3.4 Optical dipole trap

As already discussed in section 1.2.3, the force acting on an atom interacting with a light field in the semiclassical picture includes a contribution coming from the interaction of the induced atomic electric dipole moment with the intensity gradient of the light field, which is called dipole force (see Eq.(1.18)). The dipole force is conservative and derives from a potential, given in Eq.(1.20), which is typically exploited in experiments to trap the atoms in a so-called *optical dipole trap* [52]. Usually the light used for optical dipole trapping is far-detuned from the atomic resonance, so that the optical excitation is very low and the radiation pressure force on the atoms, due to photon scattering, is negligible as compared to the dipole force. Indeed, the absorptive part of the dipole interaction in far-detuned light leads to residual photon scattering of the trapping light, which sets the limits to the performance of an optical dipole trap.

The basic equations for the dipole potential and the scattering rate in a far-detuned optical dipole trap can be expressed in a convenient form as follows:

$$U_{dip}(\mathbf{r}) \simeq -\frac{3\pi c^2}{2\omega^3}\frac{\Gamma}{\delta}I(\mathbf{r}), \tag{1.40}$$

$$\Gamma_{sc}(\mathbf{r}) \simeq \frac{3\pi c^2}{2\hbar\omega^3}\left(\frac{\omega_L}{\omega}\right)^3\left(\frac{\Gamma}{\delta}\right)^2 I(\mathbf{r}). \tag{1.41}$$

where the field intensity $I(\mathbf{r}) = 2\epsilon_0 c|\mathbf{E}(\mathbf{r})|^2$ has been introduced, with ϵ_0 the dielectric constant and c the speed of light in vacuum. The derivation of these equations requires the use of the atomic complex polarizability $\bar{\alpha}$, relating the induced atomic dipole moment $\mathbf{D}$ to the electric field $\mathbf{E}$ via $\mathbf{D} = \bar{\alpha}\mathbf{E}$, and is fully explained in ref. [53]. Equations (1.40) and (1.41) show the two essential properties of optical dipole trapping in far-detuned laser fields. First, the sign of the dipole potential depends on the sign of the detuning: if the light is red-detuned ($\delta < 0$) the dipole potential is negative and attracts atoms in the light field. Thus, potential minima are found at positions with maximum intensity. On the contrary, if the laser light is blue-detuned ($\delta > 0$), the dipole potential repel the atoms out of the field, and therefore potential minima correspond to minima of the intensity. Second, since the dipole potential scales as I/δ, while the scattering rate scales as I/δ^2, it becomes clear that using laser fields with large detunings allows to keep the scattering rate as low as possible at a certain potential depth.

During my PhD project I have worked only with red-detuned optical dipole traps, therefore in the following I will review the main features of this kind of dipole traps. A comprehensive description of blue-detuned optical dipole traps can be found in [53].

The simplest realization of a red-detuned optical dipole trap is to focus onto the atoms a single laser beam with a frequency far below the atomic resonance frequency (see Fig.1.4(a)). In Gaussian optics [54], the spatial intensity distribution of a focused laser beam propagating along the z-axis with radial symmetry r is described by:

$$I(r,z) = \frac{2P}{\pi w(z)^2}\exp\left(-2\frac{r^2}{w(z)^2}\right), \tag{1.42}$$

where P indicates the total power of the beam, which can be obtained by

integrating the intensity $I(r,z)$ over the whole area in polar coordinates, and $w(z)$ is the $1/e^2$ beam radius:

$$w(z) = w_0\sqrt{1+\left(\frac{z}{z_R}\right)^2}. \tag{1.43}$$

Here, $w_0 = w(z=0)$ is called *beam waist* and denotes the minimum radius of the Gaussian beam, corresponding to the focus position ($z=0$), and $z_R = \pi w_0^2/\lambda$ is the *Rayleigh range*, that is the distance along z over which the waist of the beam has increased to $\sqrt{2}w_0$ (λ is the laser wavelength). Eq.(1.42) shows that the intensity is maximal at the focal point at the center of the beam, and is given by:

$$I_0 = I(0,0) = \frac{2P}{\pi w_0^2}. \tag{1.44}$$

From the intensity distribution one can derive the optical potential $U(r,z) \propto I(r,z)$ using Eq.(1.40). In particular, the peak intensity I_0 defines the trap depth $\hat{U}$ as:

$$\hat{U} = |U(r=0,z=0)| \approx -\frac{3\pi c^2}{2\omega^3}\frac{\Gamma}{\delta}I_0. \tag{1.45}$$

If the thermal energy k_BT of an atomic ensemble is much smaller than the potential depth $\hat{U}$, the extension of the atomic sample is radially small compared to the beam waist and axially small compared to the Rayleigh range. In this case the atoms populate only the bottom of the trap (see Fig.1.4(b)), and the optical dipole potential can be well approximated by a cylindrically symmetric harmonic oscillator potential:

$$U(r,z)_{harmonic} \approx \frac{1}{2}\frac{\partial^2 U_{dip}}{\partial r^2}(0)r^2 + \frac{1}{2}\frac{\partial^2 U_{dip}}{\partial z^2}(0)z^2 = -\hat{U}\left(1 - 2\frac{r^2}{w_0^2} - \frac{z^2}{z_R^2}\right). \tag{1.46}$$

By comparing Eq.(1.46) to the classical harmonic potential $\frac{1}{2}m(\omega_r^2 r^2 + \omega_z^2 z^2)$, it is possible to derive the trapping frequencies, i.e. the oscillation frequencies of a trapped atom, in radial and axial direction:

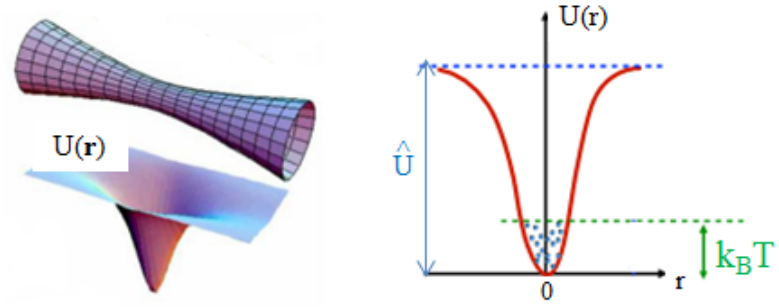

(a) (b)

Figure 1.4: Red-detuned optical dipole trap. (**a**) Spatial intensity distribution of a focused laser beam (Eq.(1.42)) (upper figure) and corresponding optical dipole potential $U(\mathbf{r})$ (lower figure). Figure courtesy of Ultracold group in Innsbruck. (**b**) If $k_B T \ll \hat{U}$, the atoms only populate the bottom of the trap, where the dipole potential can be approximated as harmonic. Figure adapted from [55].

$$\omega_r \equiv \sqrt{\frac{4\hat{U}}{mw_0^2}}, \tag{1.47}$$

$$\omega_z \equiv \sqrt{\frac{2\hat{U}}{mz_R^2}}. \tag{1.48}$$

Since the Rayleigh range z_R is larger than the beam waist w_0 by a factor of $\pi w_0/\lambda$, the axial confinement is much weaker than the radial one. Therefore, the potential in the axial direction is much less steep than in the radial direction. An important point that one has to take into consideration in order to provide stable trapping in a optical dipole trap is to ensure that the gravitational force does not exceed the confining dipole force. Focused-beam traps are therefore mostly aligned along the horizontal axis. In this case, the strong radial force minimizes the perturbing effects of gravity. Moreover, crossed optical dipole trap configurations, where two focused laser beams are crossed at their respective focii, and/or magnetic field gradients are typically used in experiments to compensate this effect.

Because $\hat{U} \propto P/w_0^2$ and $z_R \propto w_0^2$, one can derive the following expressions of practical use for the dependence of the trapping frequencies on the power and

waist of the focused laser beam:

$$\omega_r \propto \frac{\sqrt{P}}{w_0^2},\ \omega_z \propto \frac{\sqrt{P}}{w_0^3}. \tag{1.49}$$

It is worth to emphasize that the trap depths that can be achieved in a tightly focused beam are typically in the millikelvin range, orders of magnitude smaller than the thermal energy of room-temperature atoms. This means that in order to efficiently trap an atomic sample in a optical dipole trap, the atoms have to be preliminarly cooled via laser cooling methods. The standard way to load a dipole trap in ultracold atomic experiments is to start from a MOT. The dipole trap is filled by focusing the trap laser beam onto the centre of the atomic cloud in the MOT, before the latter is turned off. In the dipole trap, the atoms can be further cooled down to temperatures far below the ones achievable with laser cooling, by using a technique called *evaporative cooling*, which is described in the next section.

1.3.5 Evaporative cooling

Cooling by evaporation is a known phenomenon in daily life: it happens everytime we blow on a cup of coffee in order to cool it. In the context of trapped atomic gases, it is done by continuously removing the most energetic particles from the trap [56]. These particles occupy the high-energy tail of the thermal distribution. When, because of elastic collisions, they leave the trap, they carry away more than the average thermal energy, which means that the temperature of the remaining atoms, after rethermalization, is lower than before. Due to the lower temperature, the evaporation process slows down, unless evaporation is *forced* by modifying the system in such a way that particles with smaller and smaller energies can escape from the trap, thus sustaining the cooling process. Even though atoms are lost, the decrease of the temperature can be so large that the phase space density of the atomic cloud increases, and the system eventually reaches the condensation point.

The first experiments on evaporative cooling of alkali atoms have been done in *magnetic traps*. Magnetic traps are conservative traps where the trapping mechanism relies on the coupling of the atomic permanent or induced magnetic dipole moment to magnetic field gradients [45]. In these traps only atoms in certain spin

states can be trapped. In such system the evaporation of atoms is controlled by radio frequency (rf) radiation [57], which flips the spin of the atoms. As a result, the attractive trapping force turns into a repulsive force and expels the atoms from the trap. This scheme is energy-selective because the resonance frequency is proportional to the magnetic field and therefore to the potential energy of the atoms. The rf frequency can be chosen in such a way that only atoms with a given potential energy (i.e. the highest) will be resonant. The evaporation is then forced by progressively reducing the rf frequency, thus allowing atoms with lower and lower potential energy to escape.

Later, evaporative cooling has been realized also in optical dipole traps [58]. In these traps, if the depth $\hat{U}$ (defined in Eq.(1.45)) is fixed, the evaporation slows down when the temperature of the trapped sample decreases to values such that $k_B T \ll \hat{U}$, since elastic collisions can no longer transfer enough energy to allow atoms to leave the trap. At this point, the evaporation process can be forced by reducing the depth of the trapping potential, thus allowing less energetic atoms to escape (Fig.1.5). In practice, this corresponds to progressively reduce the power of the dipole trap laser beam.

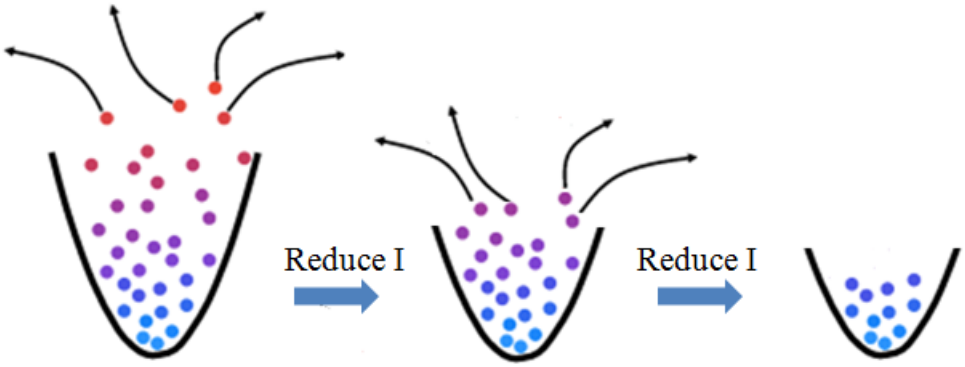

Figure 1.5: Mechanism of forced evaporative cooling in a optical dipole trap. By progressively reducing the intensity I of the laser beam used to create the optical dipole trap, the depth of the trap is decreased accordingly. This allows less and less energetic atoms to escape from the trap, thus letting the remaining atoms to thermalize at lower and lower temperatures. In the picture, the atoms drown in red are the hottest ones, whereas the atoms in light blue are the coldest. Figure courtesy of Ultracold group in Innsbruck.

Evaporative cooling constitutes a fundamental step in the realization of a BEC,

allowing to increase the phase space density of a laser cooled atomic cloud by several (typically 6-7) orders of magnitude. The essential condition for an efficient evaporative cooling is a long lifetime of the atomic sample compared to the collisional thermalization time. Since the sample lifetime is essentially limited by inelastic collisions (with the background gas, two- or three-body collisions, technical noise on the trapping potential,...) while, on the contrary, elastic collisions are essential for the thermalization of the sample, it is the ratio of elastic to inelastic collisions that eventually sets the maximum gain in phase space density achievable with evaporative cooling.

1.4 Imaging of an ultracold quantum gas

Once a BEC has been created, we want to observe it. This is made by shining a probe laser beam onto the atoms. In general, the interaction of atoms with a light beam involves three processes: absorption of photons, spontaneous re-emission of photons, and shifting the phase of the transmitted light. These properties are used in absorptive, fluorescence, and dispersive imaging methods, respectively. Moreover, a BEC can be observed either in a trap (*in-situ* imaging) or in ballistic expansion (*time-of flight* (TOF) imaging). In TOF imaging, the trapping potential is switched off and the atoms are let free to drop under the effect of gravity and expand because of their non-zero temperature, for a certain amount of time, before being probed (Fig.1.6). In the following section I will only describe the main features of absorption imaging, since this is the technique I have used during my PhD work. Fluorescence and dispersive imaging techniques are extensively discussed in ref.[59].

1.4.1 Absorption imaging

Absorption imaging is done by illuminating the atoms with a resonant laser beam and imaging the shadow cast by the atoms onto a CCD camera, due to the absorption of the resonant light (Fig.1.6).

Reliable information on the atoms can not be extracted from a single absorption image (A), since usually the probe field is inhomogeneous due to diffraction

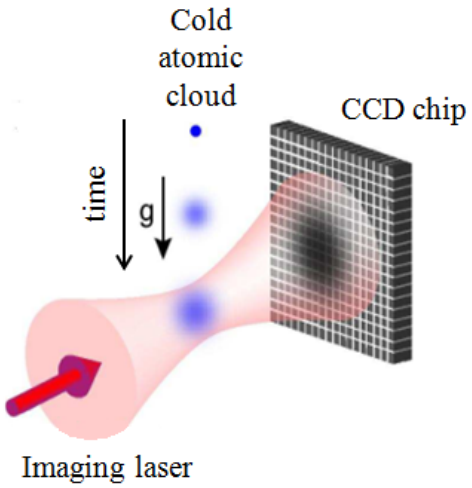

Figure 1.6: Time-of-flight absorption imaging of an ultracold atomic gas. The cloud is imaged during its free expansion, after being released from a trap. The resonant laser light used for imaging is absorbed by the atoms, which cast a shadow onto a CCD sensor. The shadow allows to reconstruct the 2D atomic density distribution in the plane perpendicular to the propagation direction of the imaging beam, at the time the image is taken (see text). In the picture, g indicates the gravitational acceleration constant. Figure adapted from [5].

fringes and the Gaussian beam profile. Therefore, other two subsequent images are typically acquired: a "bright-field" image (B), where the probe intensity is recorded with no absorbing atoms, and a "dark-field" image (D) with no atoms and no probe light, which is used to remove any stray light and CCD dark counts from the absorption image. With these three images it is possible to reconstruct the two-dimentional (2D) density distribution of the atoms in the plane perpendicular to the propagation direction of the imaging beam, according to the following procedure.

Let us indicate by I_{in} the intensity of the incident probe light, and by I_{out} the intensity of the outgoing probe beam after the absorption from the atoms. By subtracting the dark-field image both from the absorption image and from the bright-field image it is possible to calculate the *optical density* (OD) of the atomic cloud, defined as $OD = -log(I_{out}/I_{in})$. Since $\frac{I_{out}}{I_{in}} \propto \frac{A-D}{B-D}$, a 2D optical density image can be obtained as:

$$OD = -log\left(\frac{A-D}{B-D}\right). \tag{1.50}$$

If one assumes that the imaging light propagates along the z-axis, then the optical density of the atomic cloud is directly proportional to the 2D atomic density distribution in the (x, y) plane. The so-called *column density* $n_{2D}(x, y) = \int_{-\infty}^{\infty} n(x, y, z)dz$ can in fact be calculated as:

$$n_{2D}(x, y) = \frac{OD}{\sigma}, \tag{1.51}$$

where

$$\sigma = \frac{\sigma_0}{1 + \frac{4\Delta^2}{\Gamma^2} + \frac{I_{in}}{I_{sat}}}. \tag{1.52}$$

is the absorption cross section for the imaging light. Here, $\sigma_0 = 3\lambda^2/2\pi$ is the two-level absorption cross section for a resonant light (with λ the imaging laser wavelength), Δ is the detuning of the laser light from the atomic resonance, Γ is the natural linewidth of the excited state, and I_{sat} is the saturation intensity of the atomic transition (in typical experimental conditions $I_{in}/I_{sat} \ll 1$).

Chapter 2

Atomic interactions in ultracold gases

This chapter gives a theoretical description of interatomic interactions in dilute atomic gases. Understanding how atoms interact in quantum gases is important for two main reasons. First, elastic collisions play a key role in evaporative cooling, which is essential to reach Bose-Einstein condensation. Second, interactions turned out to be fully controllable in experiments, by using Feshbach resonances.

I will first review the basic concepts of quantum scattering theory, demonstrating that the scattering at low energy can be described in terms of a single parameter, the s-wave scattering length, which determines the strength and sign of the interatomic interactions. Thus, one can replace the exact short-range (van der Waals) interaction potential, whose details may be difficult to know, by a contact effective potential, giving the same s-wave scattering length as the exact potential. I will show that this effective potential is chosen in such a way that it gives the correct value of the s-wave scattering length in the Born approximation, a property which is important for the mean-field description of a gaseous BEC, given later in this chapter. Feshbach resonances are then introduced, and their working principle is described. After a brief review of the most important inelastic collision processes in a degenerate gas, I will introduce the dipole-dipole interaction, and describe its main properties. This kind of interaction is of fundamental importance in a BEC of Er atoms, because of the high permanent magnetic moment of these

atoms in their ground state.

Later, I will present a theoretical description of a weakly interacting BEC in a trap, in a mean-field approximation. In this approximation, the Gross-Pitaevskii equation describing the dynamics of the condensate state is derived. From the stationary solution of this equation, the static properties of a dilute BEC can be obtained. In particular, I will derive the BEC ground state solution in the so-called Thomas-Fermi limit (large repulsive contact interactions), where the mean-field prediction takes a simple analytical form. Finally, I will present a generalized form of the Gross-Pitaevskii equation which includes the dipole-dipole interaction contribution to the mean-field energy, and I will show the effects of this contribution on the stationary solution of a dilute BEC, again in the Thomas-Fermi limit.

The concepts presented in this chapter will be used throughout the experimental work and the numerical simulations reported in Chapter 4.

2.1 Basics of quantum scattering theory

In a ultracold atomic gas the mean interparticle distance $\langle r \rangle$ is usually much larger than the interaction range b (typical numbers are $\langle r \rangle \sim 10^2$ nm, $b \sim$ nm). Because of this dilutness, two-body interactions between atoms dominate, and three- and higher-body interactions are negligible. In this diluteness condition, collisions in atomic gases are well described through quantum scattering theory [45]. Here we consider an elementary collision process between two identical particles with the same mass m and same internal state. The two particles interact via an interaction potential $V(\mathbf{r})$ that depends on the distance $\mathbf{r}$ between the two particles. The scattering theory shows that the collision dynamics is entirely contained in the description of the relative motion of the two particles and correspond to the scattering of a fictitious particle of mass $\mu_r = m/2$ in the the potential V. This is expressed by the Hamiltonian:

$$H = \frac{\mathbf{p}^2}{2\mu_r} + V(\mathbf{r}), \tag{2.1}$$

where $\mathbf{r}$ and $\mathbf{p}$ are the position and momentum of the reduced particle.

For neutral atoms, the interaction potential $V(\mathbf{r})$ is characterized by a strong

repulsion at small distances, due to the overlapping of the electronic clouds of each atom, which prevents the nuclei to come too close to each other (Fermi pressure), and it is weakly attractive at large distances because of the van der Waals interaction. This latter is a short-range interaction which falls off with the interatomic distance r as $-1/r^6$. Depending on the atomic species (and more specifically on the electron configuration) other interactions may come into play, such as magnetic dipole-dipole interactions or quadrupole-quadrupole forces. In the case of alkali atoms, the van der Waals interaction dominates and is isotropic at large distance, due to the simplicity of the electron configuration. This is not the case for more complex atomic species, such as chromium, dysprosium or erbium [60].

The scattering problem with Hamiltonian (2.1) can be solved by solving the following Schrödinger equation:

$$\left(-\frac{\hbar^2}{2\mu_r}\Delta + V(\mathbf{r})\right)\psi(\mathbf{r}) = E\psi(\mathbf{r}), \tag{2.2}$$

with $E = \frac{\hbar^2 k^2}{2\mu_r}$. Thanks to the diluteness condition, collision in ultracold gases can be correctly described by considering the asymptopic behaviour ($r \to \infty$) of ψ. In this limit, the solution of Eq.(2.2) can be written as a sum of a plane wave, corresponding to the unperturbed free particles, and a spherical wave, corresponding to the scattered particles:

$$\psi_{\mathbf{k}}(\mathbf{r}) = e^{i\mathbf{k}\cdot\mathbf{r}} + f(k, n, n')\frac{e^{ikr}}{r}, \tag{2.3}$$

where $n = \mathbf{k}/k$, $n' = \mathbf{r}/r$, and $f(k, n, n')$ is the *scattering amplitude* in the direction defined by the unit vector n'. At a given position $\mathbf{r}$ within the asymptotic limit, the scattering amplitude f does not depend on the distance r, and is given by:

$$f(k, n, n') = -\frac{\mu_r}{2\pi\hbar^2}\int d^3\mathbf{r}' e^{-i\mathbf{k}'\cdot\mathbf{r}'} V(\mathbf{r}')\psi_{\mathbf{k}}(\mathbf{r}'), \tag{2.4}$$

where $\mathbf{k}' = kn'$. This implicit expression of the scattering state links the value of the wavefunction far from the scattering region (f) to its values inside the scattering region (through the potential V). Its complete analysis requires to solve

the Schrödinger equation (2.2). The so-called Born approximation offers a zeroth order estimate of the scattering amplitude, valid for a weak interaction potential. Thus, to lowest order in V, one can neglect the scattered part in the integral and replace $\psi_{\mathbf{k}}(\mathbf{r}')$ by the unperturbed wavefunction $e^{i\mathbf{k}\cdot\mathbf{r}'}$. This gives:

$$f(k,n,n') \simeq -\frac{\mu_r}{2\pi\hbar^2}\int d^3\mathbf{r}' e^{i(\mathbf{k}-\mathbf{k}')\cdot\mathbf{r}'}V(\mathbf{r}'), \tag{2.5}$$

which is simply the Fourier transform of the scattering potential V in $(\mathbf{k}-\mathbf{k}')$.

The knowledge of the scattering amplitude f gives a direct access to the differential and total scattering cross sections, respectively given by:

$$\frac{d\sigma(\mathbf{k})}{d\Omega} = |f(k,n,n')|^2, \tag{2.6}$$

and

$$\sigma(\mathbf{k}) = \int |f(k,n,n')|^2 d^2n'. \tag{2.7}$$

For identical particles the two scattering diagrams of Fig.2.1 can not be distinguished, and the wavefunction $\psi_{\mathbf{k}}(\mathbf{r})$ of Eq.(2.3) must be symmetrized (antisymmetrized) with respect to changing the sign of the relative coordinate $\mathbf{r} \to -\mathbf{r}$, if the particles are bosons (fermions). The (anti-)symmetrization of the wave function is done by replacing:

$$f(k,n,n') \to f(k,n,n') \pm f(k,n,-n') \tag{2.8}$$

where the +(-) sign applies to bosons (fermions).

2.1.1 Partial wave expansion

In many cases, and in particular in the case of alkali atoms, the scattering potential can be considered as spherically symmetric, that is $V(\mathbf{r}) = V(r)$. This consideration simplifies greatly the scattering problem. First, by symmetry argument, f only dependends on the angle θ between n and n': $f(k,n,n') \equiv f(k,\theta)$. Second, the Hamiltonian (2.1) commutes with L^2 and L_z, where L is the relative angular momentum, so that the wave function $\psi_{\mathbf{k}}$ is conveniently expanded on the

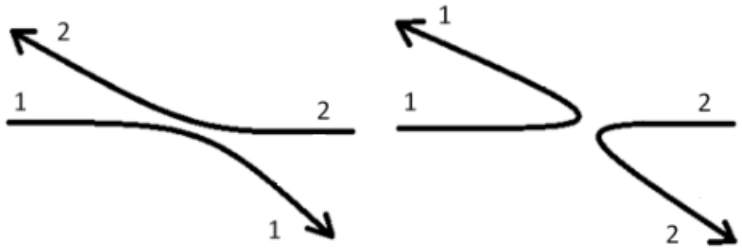

Figure 2.1: Two collisional processes which are indistinguishable for two identical particles, indicated by 1 and 2. The two processes yeld the same final state, therefore their amplitude probability has to be symmetrized if the particles are bosons.

spherical-wave basis, taking z as the direction of the incident wave (i.e. n). Even in absence of spherical symmetry, such a partial-wave expansion is typically used and reads:

$$\psi_{\mathbf{k}}(\mathbf{r}) = \sum_{l=0}^{\infty} \sum_{m=-l}^{l} Y_l^m(\theta, \phi) \frac{u_{k,l,m}(r)}{r}, \tag{2.9}$$

where ϕ is the azimutal angle around the z-axis, and $Y_l^m(\theta, \phi)$ are the spherical harmonic functions. Each term of the sum (2.9) corresponds to a partial wave with angular momentum norm $\hbar\sqrt{l(l+1)}$ and projection $m\hbar$. In the spherically symmetric case, since the incident wave is an eigenstate of L_z with eigenvalue $m = 0$, and due to the conservation of flux, only the sperical harmonics with $m = 0$ contribute in (2.9). That is, the only contribution to the scattering is given by $Y_l^0(\theta, \phi) \propto P_l(\cos\theta)$, where $P_l(x)$ are the Legendre polynomials.

Each radial wavefunction $u_{k,l}(r)$ satisfies a 1D Schrödinger equation with an effective potential

$$V_e(r) = V(r) + \frac{\hbar^2 l(l+1)}{2\mu_r r^2} \tag{2.10}$$

where the second term is the centrifugal barrier (for $l > 0$). It can be demonstrated (see ref. [45]) that at large distances ($kr \gg 1$) the radial wave functions $u_{k,l}(r)$ can be expressed in terms of phase shifts $\delta_l(k)$ according to the following equation:

$$u_{k,l}(r) \simeq \sin(kr - l\frac{\pi}{2} + \delta_l(k)) \tag{2.11}$$

where $\delta_l(k)$ are real and depend on the incident wave vector modulus. Therefore, in the limit of large r, the radial wave function $u_{k,l}(r)$ behave as a free wave ($V = 0$), except for a possible phase shift for the reflected outgoing wave.

By comparing equations (2.9) and (2.11) with (2.3), and expanding the plane wave $e^{i\mathbf{k}\cdot\mathbf{r}} = e^{ikz}$ in Legendre polynomials, one obtains the scattering amplitude in the form of a partial wave expansion:

$$f(k,\theta) = \frac{1}{2ik}\sum_{l=0}^{\infty}(2l+1)(e^{2i\delta_l(k)} - 1)P_l(\cos\theta). \tag{2.12}$$

As a consequence, also the cross section can be expressed as a partial wave expansion using Eq.(2.7), thanks to the orthogonality of the spherical waves. The expression for the total cross section is then given by:

$$\sigma_k^{tot} = \frac{4\pi}{k^2}\sum_{l=0}^{\infty}(2l+1)\sin^2\delta_l(k). \tag{2.13}$$

The symmetrization condition (2.8) causes the cancellation of the odd partial waves for bosons and of the even ones for fermions. One thus obtains:

$$\text{for bosons: } \sigma_k^{tot,B} = \frac{8\pi}{k^2}\sum_{2l}(2l+1)\sin^2\delta_l(k), \tag{2.14}$$

$$\text{for fermions: } \sigma_k^{tot,F} = \frac{8\pi}{k^2}\sum_{2l+1}(2l+1)\sin^2\delta_l(k). \tag{2.15}$$

2.1.2 Scattering length

Let us consider the centrifugal barrier $\frac{\hbar^2 l(l+1)}{2\mu_r r^2}$ entering in the effective potential (2.10) felt by the radial partial wave $u_{k,l}$ with $l > 0$. A relative particle with an energy $E = \hbar^2k^2/2\mu_r$ much smaller than the resulting barrier height does not feel the short-range potential $V(r)$, as it will be reflected on the barrier. One thus qualitatively expects that scattering amplitudes (or equivalently the phase shifts $\delta_l(k)$) vanish when $k \to 0$ for all partial wave with $l > 0$. Therefore, the only

partial wave contributing to the scattering in the low energy limit is the one with $l = 0$ (*s-wave*), for which there is no energy barrier.

Note that this low energy limit describes well collisions which verify $kb \ll 1$ (equivalently $E \ll \hbar^2/2\mu_r b^2$), where b is the interaction range. In a gas, this condition is satified for $k_B T \ll \hbar^2/2\mu_r b^2$ (equivalently $\lambda_{dB} \gg b$).

As a consequence, the total low-energy cross section for bosons reads:

$$\sigma_k^{tot,B} = \frac{8\pi}{k^2} \sin^2 \delta_0(k), \tag{2.16}$$

whereas, since only odd partial waves contribute to the cross section for identical fermions, at low temperature a fermionic gas behaves as an ideal, non interacting, gas.

Finally, one can define the *s-wave scattering length* a:

$$a = -\lim_{k\to 0} \frac{\tan \delta_0(k)}{k}, \text{ or equivalently } \lim_{k\to 0} \delta_0(k) = -ka, \tag{2.17}$$

such that the low-energy limit of the scattering amplitude and scattering cross section for identical bosons tend to constant values:

$$\lim_{k\to 0} f(k) = -a, \tag{2.18}$$

$$\lim_{k\to 0} \sigma_k^{tot,B} = 8\pi a^2. \tag{2.19}$$

Equations (2.18) and (2.19) show that in a ultracold bosonic gas, a is the only relevant parameter which characterizes the short-range collisions at low energy. It is important to note that this argument is in fact true if $V(r)$ decreases fast enought to zero for increasing r (so-called short-range interaction potential). This is the case for the Van der Waals potential, for which the scattering at low energy is isotropic. Instead, for $V(r)$ decreasing as r^{-3} or slower (so-called long-range interaction potential), all partial wave would contribute in the low energy limit. This comes from a general result of low-energy scattering (see, for instance [61]) stating that for a central potential falling off at large distances like $1/r^n$, the scattering phase shifts $\delta_l(k)$ scale, for $k \to 0$, like k^{2l+1} if $l < (n-3)/2$, and like k^{n-2} otherwise.

In the following, for convenience, I will simply use the term "scattering length" to indicate the "s-wave scattering length".

2.1.3 Effective contact potential

In the previous section it has been demonstrated that the scattering of a pair of identical particles with small total energy via a short-range interaction potential (such as the van der Waals) is dominated by the s-wave contribution to the wave function, and it is described entirely in terms of a single parameter, the scattering length a. This is a fundamental point, as it can be shown that, in the ultracold regime, the macroscopic properties of dilute gases do not depend on the details of the interatomic potential $V(r)$, which in general has a complicated dependence on the interparticle distance and can be difficult to determine, but simply on a. In contrast, a is usually much easier to predict as well as readily accessible in experiments [45]. Therefore, for the purpose of calculating the many-body properties of an ultracold and dilute gas, one can replace the true interatomic potential by an effective potential $V_{eff}(r)$ that gives the same scattering length as $V(r)$. The idea is then to use the simplest effective potential possible, namely a contact potential of the form:

$$V_{eff}(r) = g\delta(r), \tag{2.20}$$

where $\delta(r)$ denotes the Dirac delta function, and the coupling constant g should be taken such that V_{eff} and V correspond to the same scattering length. The scattering amplitude due to V_{eff} can be calculated in the Born approximation (Eq. (2.5)), and reads:

$$f(k,\theta) = -\frac{\mu_r g}{2\pi\hbar^2}. \tag{2.21}$$

Then, using equations (2.21) and (2.18), one finds:

$$g = \frac{2\pi\hbar^2 a}{\mu_r} = \frac{4\pi\hbar^2 a}{m}. \tag{2.22}$$

Equations (2.20) and (2.22) show that the scattering length also determines the

sign of the effective short-range interatomic potential: if $a > 0$, V_{eff} is repulsive, if $a < 0$, V_{eff} is attractive. This effective potential will be used in section 2.5 that is devoted to the theoretical description of a weakly interacting BEC.

2.2 Tuning the interactions: Feshbach resonances

One of the most fascinating features of cold atom physics is the possibility of controlling the interactions between the atoms. Indeed, the value and the sign of the scattering length a which determine the ultracold collision process, can be controlled in the experiments by simply tuning an external parameter, such as a uniform magnetic field applied on the atomic sample. The physical mechanisms responsible for the variation of a are the so-called *Feshbach resonances*, that appear when, during a collision process, the two colliding atoms pass through a resonant intermediate state where they are temporarily bound, before separating again.

Feshbach resonances have been initially investigated in the context of nuclear physics [62] and atomic physics [63], and later they have become important in cold atomic physics [64] since they constitute the essential tool to tune the *strength* of the effective interatomic interaction, passing from non-interacting, to weakly interacting to strongly interacting regimes (by varying the *strength* of a), and also changing the *sign* of the interactions from repulsive to attractive and viceversa (by changing the *sign* of a).

Here I will outline the basic physics of magnetically-tunable Feshbach resonances, following ref. [5]. A detailed description of Feshbach resonances can be found, for instance, in the review [11].

Let us consider the collision of two atoms respectively in the internal states of quantum numbers f_1, m_{f_1} and f_2, m_{f_2}, characterizing the total angular momentum norm and projection. At very low energy, one can consider that the atoms approach each other with a orbital angular momentum $l = 0$. The initial collision state of the two ultracold atoms is thus characterized by the quantum numbers:

$$\alpha : \ \{f_1, m_{f_1}, f_2, m_{f_2}, l = 0\} \tag{2.23}$$

indicated by the simplified notation α. This set of quantum numbers defines a *collision channel*, here the so-called *entrance channel* or *open channel*. Of course, there are other channels defined by other sets β of quantum numbers.

One important point leading to the Feshbach resonances is that, taking into account the internal states of the atoms, the previously introduced scattering Hamiltonian (2.1) can show a coupling of the different channels. This can come from the mere anisotropy of the scattering potential $V(r)$, as it is the case for Er, for example (see below). It can also come from the dependence of V on the total electronic spin of the atom pair. This will couple the channels if the nuclear spin is not zero (and is thus related to the existence of an hyperfine structure, see section 1.2.1). An important additional term in (2.1) when accounting for the internal state of the atoms, is the Zeeman effect (section 1.2.2).

Two-channel model Let us consider a simplified model that takes only two channels into account: the open channel, which contains the entering collision state, with a very small energy $E \simeq 0$, and a second channel containing a resonant bound state, whose energy E_{res} is very close to E. This latter is called *closed channel* if its dissociation threshold is above E, so that the two colliding atoms can not access the continuum of this channel (see Fig.2.2).

The state of the system can be written as a vector whose components refer to each channel:

$$\begin{pmatrix} |\phi_{op}\rangle \\ |\phi_{cl}\rangle \end{pmatrix} \tag{2.24}$$

where the indices *op* and *cl* refer to the quantum numbers (for instance the spin states) in each channel. In this two-state basis, the two-channel Hamiltonian H_2 reads:

$$H_2 = \begin{pmatrix} -\frac{\hbar^2\Delta}{2\mu_r} + V_{op}(r) & W(r) \\ W(r) & -\frac{\hbar^2\Delta}{2\mu_r} + V_{cl}(r) \end{pmatrix}, \tag{2.25}$$

where V_{op} and V_{cl} are the interaction potentials operators in the open and closed channels, respectively, and W describes the coupling between the two channels.

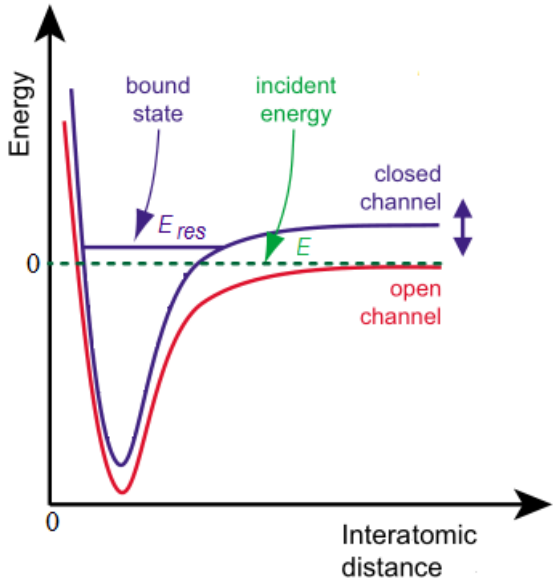

Figure 2.2: Two-channel model for a Feshbach resonance. Two atoms prepared in the open channel undergo a collision at an energy E which is typically close to zero in the ultracold domain. In the course of the collision the open channel is coupled to the closed channel, which supports a bound molecular state at energy E_{res}. When $E_{res} \simeq 0$ a scattering resonance occurs. If the magnetic moments of the closed and open channels differ, resonant coupling can be conveniently realized by tuning the position of the closed channel with respect to the open one through the variation of an external magnetic field. Figure adapted from [5].

In absence of coupling ($W = 0$), The potential V_{op} gives rise to the so called *background scattering length*, indicated by a_{bg}. A Feshbach resonance occurs when there exists one bound state $|\phi_{res}\rangle$ in the potential V_{cl} which has an energy close to E and in presence of a non zero coupling $W(r)$. In the following, all the eigenstates of the Hamiltonian projected in the closed channel other than the resonant bound state can be neglected, since they negligibly contribute to the scattering. Assuming that the spin configurations of the open and closed channels have different magnetic moments, the energies of the colliding states in these channels vary differently when a static magnetic field B is applied and scanned, because of a different Zeeman shift. By properly tuning B, it is possible to bring the bound state of the closed channel potential on resonance with the entrance collision state in the open channel, that is $E_{res} = E \simeq 0$. When the energy difference between the

two channels vanishes, one expects a divergence of the scattering amplitude, and therefore a divergence of the scattering length a. This is the basic mechanism of a Feshbach resonance in a ultracold atomic gas.

The variation of the scattering length with the applied magnetic field close to a Feshbach resonance reads [65]:

$$a(B) = a_{bg}\left(1 - \frac{\Delta}{(B - B_0)}\right). \tag{2.26}$$

where Δ denotes the *resonance width* in units of magnetic field, and B_0 is the *resonance position*, that is the value of the magnetic field where the scattering length diverges ($a(B_0) \to \pm\infty$). The background scattering length a_{bg} represents the scattering length far from the resonance. Another important quantity is the *zero crossing* of the scattering length associated with a Feshbach resonance: it occurs at a magnetic field $B_{zc} = B_0 + \Delta$. Note that both a_{bg} and Δ can be positive or negative, and that the sign of a changes when B is scanned around B_0. The relation (2.26) is depicted in Fig.2.3.

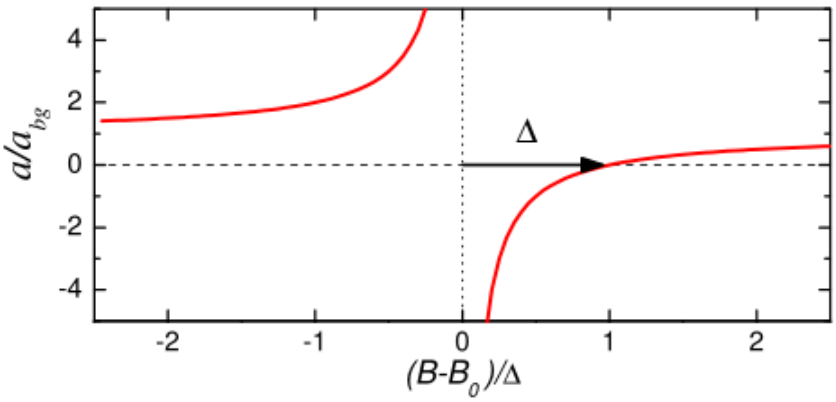

Figure 2.3: Variation of the scattering length a with the magnetic field B near a Feshbach resonance. a_{bg} is the value of the off-resonance scattering length, Δ is the resonance width and B_0 the resonant magnetic field. Figure adapted from [11].

Within the two channel model, one can find that the resonance width Δ relates to the coupling strength via [5]:

$$\delta\mu a_{bg}\Delta = \frac{\hbar^2}{2\mu_r r^*}, \tag{2.27}$$

where $\delta\mu$ is the difference between the magnetic moments of the open and closed channels in absence of coupling, and r^* is a characteristic length defined by:

$$\langle\phi_{cl}|W|\phi_{op}\rangle = \frac{\hbar^2}{2\mu_r}\sqrt{\frac{4\pi}{r^*}}. \tag{2.28}$$

Eq.(2.28) shows that $1/r^*$ is a measure of how strongly the open and closed channels are coupled. Since $\Delta \propto 1/r^*$, then the stronger is the coupling, the wider is the resonance.

The ability to tune the scattering length close to the zero crossing (where $a = 0$) is measured by the quantity:

$$\left(\frac{da}{dB}\right)_{a\simeq 0} \simeq \frac{a_{bg}}{\Delta}. \tag{2.29}$$

This means that a small a_{bg} and a large Δ are desirable conditions to get a high degree of tunability of the scattering length. Moreover, typically in the lab the magnetic noise can be of the order of a few tens of mG and, therefore, tuning the interactions on sharp resonances can be challenging. Exceptionally favourable cases are represented by several alkali atoms, and in particular by ^{39}K, for which Feshbach resonances can be as wide as 10-100 G, and take place at values of the magnetic field experimentally easy to access. Indeed, the high degree of tunability of the scattering length via Feshbach resonances constitutes the most attracting feature of ^{39}K. A completely different scenario opens up in the case of the more complex lanthanide Er, for which the width of the Feshbach resonances can be as low as 10 mG. This requires a very high precision in the determination of the magnetic field in the lab in order to be able to tune the interactions.

2.3 Inelastic collisions

Inelastic scattering processes lead to a change in the internal states of the atoms. The most relevant inelastic collisions in ultracold atomic gases are of three types: collisions with the background gas, two-body processes with spin-exchange,

and three-body collisions. All these processes can cause losses of atoms from the trap. Collisions with the background gas can be minimized in experiments by reaching ultra-high vacuum pressures of $\sim 10^{-11}$ mbar in the vacuum chamber. Two-body spin-exchange processes are the main cause of atom losses in magnetic traps, since in these traps only certain spin states can be trapped. In three-body collisions, two atoms form a molecule and the third one ensures conservation of momentum. The binding energy of the molecule gets converted into kinetic energy, leading to the loss of all the three atoms from the trap. Three-body recombination limits the maximum density that can be achieved in a trap, being strongly density-dependent. If the atomic sample is dilute, the probability to find three atoms close enough to determine a three-body loss, can be negligible. The rate of three-body collisions in a gas is given by [66]:

$$\frac{dn}{dt} = -L_3 n^3, \tag{2.30}$$

where n is the atomic density, and L_3 the three-body recombination parameter. Both for alkali-metal atoms and for lanthanides L_3 is on the order of 10^{-41} m^6/s [67, 26]. Thus, for a typical BEC density of $\sim 10^{14}$ cm^{-3}, Eq.(2.30) predicts a lifetime of the condensate of ~ 10 s.

2.4 Dipole-dipole interaction

In ultracold gases of atomic species like Er, which possess a permanent magnetic dipole moment, the interparticle interaction does not only include the short-range effective potential described in section 2.1.3, but also the so-called *dipole-dipole interaction* (DDI). The treatment of the DDI below is based on the reviews [68] and [69].

For two atoms 1 and 2 with a permanent magnetic dipole moment μ_m along the unit vectors $\mathbf{e_1}$ and $\mathbf{e_2}$ and relative position $\mathbf{r}$, as represented in Fig.2.4(a), the DDI energy reads:

$$V_{dd}(\mathbf{r}) = \frac{\mu_0 \mu_m^2}{4\pi} \frac{(\mathbf{e_1} \cdot \mathbf{e_2}) r^2 - 3(\mathbf{e_1} \cdot \mathbf{r})(\mathbf{e_2} \cdot \mathbf{r})}{r^5}. \tag{2.31}$$

where μ_0 is the permeability of vacuum. When an external magnetic field is

present, all the dipoles point in the same direction, parallel to the field, and the DDI energy simplifies to:

$$V_{dd}(r,\theta) = \frac{\mu_0 \mu_m^2}{4\pi} \frac{1 - 3\cos^2\theta}{r^3}, \tag{2.32}$$

where θ is the angle between the relative position of the particles $\mathbf{r}$ and the direction of polarization, here assumed to be the z-axis (Fig.2.4(b)).

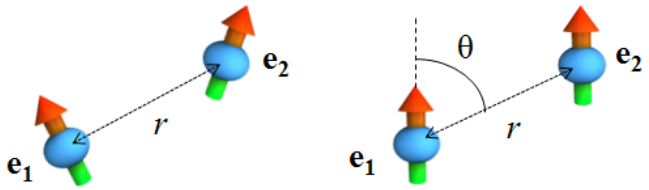

(a) (b)

Figure 2.4: Two particles interacting via dipole-dipole interaction. (**a**) Non-polarized dipoles. (**b**) Polarized dipoles. $\mathbf{e_1}$ and $\mathbf{e_2}$ are the unit vectors of the dipole moments for particles 1 and 2 respectively, r is the distance between the dipoles and θ in **b** indicates the angle between the relative position of the dipoles and their direction of polarization.

The potential V_{dd} has two important features: it is *long-range*, scaling with the interpartcile distance as $\sim 1/r^3$ (see discussion in 2.1.2), and *anisotropic*, due to the $\cos^2\theta$-dependence. As θ varies between 0 and $\pi/2$, the factor $(1 - 3\cos^2\theta)$ varies between -2 and 1, and thus the DDI is repulsive for particles sitting *side-by-side* ($\theta = \pi/2$), while it is attractive (with twice the strength of the repulsive interaction) for dipoles in the so-called *head-to-tail* configuration ($\theta = 0$), see Fig.2.5. There exists also a "magic angle" $\theta_m = \arccos(1/\sqrt{3}) \simeq 54.7°$ for which the DDI vanishes.

The long-range character and the anisotropy of the DDI have both very important consequences on all the variety of properties of an ultracold gas. They affect the scattering properties, the stability of the system, the thermodynamics and many-body properties. A striking effect of the DDI on the many-body physics of an ultracold bosonic quantum gas will be presented in chapter 4. Here I will focus on the consequences of the DDI on the scattering properties.

As already discussed in section 2.1.2, usually the interaction potential between

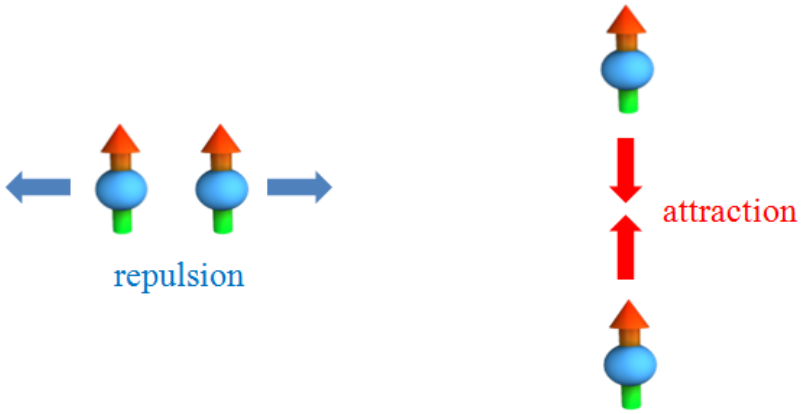

Figure 2.5: Anisotropy of the dipole-dipole interaction. On the left: two polarized dipoles side-by-side repel each other. On the right: two polarized dipoles in a head-to-tail configuration attract each other.

two atoms separated by a distance r behaves as $-1/r^6$ at large distances. For such a van der Waals potential, it has been demonstrated that in the limit of a vanishing collision energy, only the s-wave scattering plays a role. In the case of the dipole-dipole interaction, the long-range behaviour, characterized by a slow decay $\sim 1/r^3$ at large distances, implies that all partial waves contribute to the scattering amplitude, in contrast to the case of a short-range interaction. Moreover, the anisotropy of the interaction means that the orbital angular momentum L is not conserved during the scattering: the DDI mixes all even (odd) orbital angular momenta scattering channels in the scattering of two bosons (fermions). Therefore, one cannot replace the true interaction potential simply by a short-range, isotropic contact potential, but needs to use (in Born approximation, see section 2.1.3) an effective potential of the form [69]:

$$V(\mathbf{r},\theta) = \frac{4\pi\hbar^2 a}{m}\delta(\mathbf{r}) + \frac{\mu_0\mu_m^2}{4\pi}\frac{1-3\cos^2\theta}{r^3}, \tag{2.33}$$

where the first term on the right-hand side is the effective contact potential (2.20) accounting for the short-range interaction, and the second term is the long-range and anisotropic DDI potential.

The strength of the DDI can be quantified by the so-called *dipolar length*, defined as:

$$a_{dd} \equiv \frac{\mu_0 \mu_m^2 m}{12\pi\hbar^2}. \tag{2.34}$$

This length scale expresses the characteristic range of the DDI, and it can be demonstrated that it determines the low-energy limit of the dipole-dipole scattering amplitudes [69]. In this sense, a_{dd} can be considered as the analogous for the DDI of the scattering length a for the short-range interaction. It is very useful to introduce here the ratio of the dipolar length to the scattering length, denoted by ϵ_{dd}:

$$\epsilon_{dd} \equiv \frac{a_{dd}}{a} = \frac{\mu_0 \mu_m^2}{3g}, \tag{2.35}$$

where $g = 4\pi\hbar^2 a/m$ is the coupling constant of the effective contact potential (see section 2.1.3). In most cases, it is this ratio, comparing the relative strength of the dipolar and contact interactions, which determines the physical properties of a dipolar system. Indeed, $\epsilon_{dd} > 1$ defines the dipolar-dominated regime in which the DDI rules the behaviour of the system. An example will be given in Chapter 4.

Dipolar systems Atoms can have a permanent magnetic moment in their electronic ground state, due to the spin and the orbital angular momentum of the electrons, and the strength of the magnetic dipole moment varies from element to element. In alkali atoms, typically $\mu \leq 1\mu_B$, and thus the magnetic dipolar effects are very weak. However, there are other atomic species, like chromium, erbium, europium, holmium, dysprosium and terbium, which possess a large magnetic moment of several Borh magneton in their ground state, and thus experience significant magnetic DDI. Among them, only three elements have been Bose-condensed up to now: chromium (with a magnetic moment $\mu_{Cr} = 6\mu_B$) [18], dysprosium ($\mu_{Dy} = 10\mu_B$) [23] and erbium ($\mu_{Er} = 7\mu_B$) [24]. For these species, far from any Feshbach resonance (that is, when the scattering length equals the background scattering length), ϵ_{dd} ranges from ~ 0.1 in the case of chromium, to ~ 1 for dysprosium and erbium. In chromium, an $\epsilon_{dd} \simeq 0.16$ has been enough to observe a perturbative effect of the dipolar interaction on the expansion dynamics of the cloud [70]. Moreover, close to a Feshbach resonance, one can decrease the value of

the scattering length a, in order to increase ϵ_{dd}, and thus obtain enhanced dipolar effects (see, for instance [71], [32], [26], and Chapter 4 of this thesis).

Note in passing that other dipolar quantum system than magnetic atoms have been of interest for the experimentalists. These include heteronuclear polar molecules in their electronic molecular ground state, and Rydberg atoms, i.e. atoms with one electron promoted to a high energetic state. This systems have a much larger dipolar coupling constant with respect to magnetic dipoles, but they are difficult to investigate experimentally. In fact, quantum degenerate gases of polar molecules have not been realized yet. Progresses have been made in recent years in the cooling of molecules, but the densities and temperatures achieved so far are still orders of magnitude away from the quantum degenerate regime. A promising approach towards degeneracy, pursued by several groups in experimental molecular physics around the world, is to start from already ultracold atomic mixtures, and then use a Feshbach resonance to create heteronuclear molecules [72]. In the case of Rydberg atoms, the main limitation is given by the short lifetime of the excited state [73]. Electric dipoles could also be induced in atoms, however, due to the typically very small electric polarizability of ground state atoms, extremely high electric field strengths would be necessary to induce a relevant dipolar interaction in this case.

Feshbach resonances in dipolar systems The anisotropy of the DDI has been demonstrated to be at the origin of a rich spectrum of Feshbach resonances in the strongly magnetic lanthanide Er and Dy atoms [60, 74]. It is interesting to compare Feshbach resonances in Er, for instance, with those in alkali-metal atoms. First, in alkalis Feshbach resonances are typically induced by a difference in the magnetic moment of different molecular hyperfine states, where multiple $l = 0$ (s-wave) channels are present, and thus s-wave Feshbach resonances exist. For bosonic Er, where the hyperfine structure is absent, Feshbach resonances are instead due to the coupling of rotational bound states. This coupling is achieved through the anisotropic DDI, which couple bound states with non-zero orbital angular momentum l. Experimentally, an extremely large density of Feshbach resonances, of about three per Gauss for the bosonic ^{166}Er and ^{168}Er isotopes, and about 25 per Gauss for the fermionic ^{167}Er (which, additionally, has an hyperfine

structure) has been measured (see ref. [75]). This density, is about 2 orders of magnitude larger than the one observed in ultracold alkali-metal atoms [76]. As a consequence, Feshbach resonances in lanthanides are typically much narrower than the one in alkalis (see discussion at the end of section 2.2).

Tuning of the dipole-dipole interaction An approach to tune the DDI was proposed in ref. [77]. It is based on a combination of a static magnetic field along the z-axis and a fast rotating magnetic field in the perpendicular xy-plane, such that the dipoles adiabatically follow the time-dependent external field. This is valid provided that the rotating frequency of the field Ω is much smaller than the Larmor frequency $\omega_{Larmor} = \mu_m B/\hbar$, and much higher compared to the typical frequencies of the atomic motion, given by the trapping frequencies of the potential which confines the dipolar gas. In this limit, the particles feel a time-average of the DDI (2.32) over a period $2\pi/\Omega$, which reads:

$$\langle V_{dd}(r,\theta,\phi)\rangle = \frac{\mu_0\mu_m^2}{4\pi}\frac{1-3\cos^2\theta}{r^3}\left(\frac{3\cos^2\phi-1}{2}\right). \tag{2.36}$$

The averaged energy (2.36) differs from the interaction energy of aligned dipoles (2.32) by a factor $(3\cos^2\phi-1)/2$. By varying the angle ϕ from 0 to $\pi/2$, this factor can be changed continuosly from 1 to -1/2, thus allowing to invert the sign of the DDI, and even cancel it completely when ϕ is equal to the magic angle θ_m. Note that when $\phi > \theta_m$, the averaged DDI turns out to be attractive for particles sitting side-by-side.

2.5 Mean field description of a trapped Bose-Einstein condensate

In this section I will give a theoretical description of the main properties of a weakly interacting trapped BEC, following the treatment of ref. [78]. In particular, I will discuss properties such as the shape and size of the density distribution in a trapped condensate. Other properties, like elemenatry excitations will be discussed in Chapter 4.

The many-body Hamiltonian operator describing N interacting bosons confined by an external potential V_{ext} is given, in second quantization, by:

$$\begin{aligned}\hat{H} = &\int d\mathbf{r}\hat{\Psi}^\dagger(\mathbf{r})[-\frac{\hbar^2}{2m}\nabla^2 + V_{ext}(\mathbf{r})]\hat{\Psi}(\mathbf{r}) + \\ &\frac{1}{2}\int\int d\mathbf{r}d\mathbf{r}'\hat{\Psi}^\dagger(\mathbf{r})\hat{\Psi}^\dagger(\mathbf{r}')V(\mathbf{r}-\mathbf{r}')\hat{\Psi}(\mathbf{r}')\hat{\Psi}(\mathbf{r}),\end{aligned} \tag{2.37}$$

where $\hat{\Psi}(\mathbf{r})$ and $\hat{\Psi}^\dagger(\mathbf{r})$ are the boson field operators that annihilate and create a particle at the position $\mathbf{r}$, respectively, and $V(\mathbf{r}-\mathbf{r}')$ is the two-body interatomic potential. A weakly-interacting dilute Bose gas in which Bose-Einstein condensation occurs is well described within the Bogoliubov method [79], which consists in separating out the condensate contribution to the bosonic field operator. In general, the field operator can be written as $\hat{\Psi}(\mathbf{r}) = \sum_\alpha \Psi_\alpha(\mathbf{r})\hat{a}_\alpha$, where $\Psi_\alpha(\mathbf{r})$ are single-particle wave functions and $\hat{a}_\alpha$ are the corresponding annihilation operators.

Bose-Einstein condensation occurs when a single-particle state gets macroscopically occupied: the number of particles N_0 of this particular state becomes macroscopic, that is $N_0 \gg 1$, and the ratio N_0/N remains finite in the thermodynamic limit $N \to \infty$. In this regime the operators $\hat{a}_0$ and $\hat{a}_0^\dagger$ can be treated like c-numbers: $\hat{a}_0 = \hat{a}_0^\dagger = \sqrt{N_0}$. The field operator can then be decomposed as $\hat{\Psi}(\mathbf{r}) = \sqrt{N_0}\Phi_0(\mathbf{r}) + \Psi'(\mathbf{r})$, where $\Psi'(\mathbf{r})$ is a quantum field operator accounting for the non-condensed atoms. The generalization of the above decomposition (indicated as *mean-field approximation*) to the case of time-dependent configurations is given by:

$$\hat{\Psi}(\mathbf{r},t) = \Phi_0(\mathbf{r},t) + \hat{\Psi}'(\mathbf{r},t), \tag{2.38}$$

where the Heisenberg representation for the field operators has been used. Here, the function $\Phi_0(\mathbf{r},t)$ is a classical field which has the meaning of an order parameter, and it is also referred to as the "macroscopic wave function of the condensate". Its modulus defines the condensate density through $n(\mathbf{r},t) = |\Phi_0(\mathbf{r},t)|^2$. The time evolution of the field operator $\hat{\Psi}(\mathbf{r},t)$ can be described using the Heisenberg equation with the many-body hamiltonian (2.37), which gives:

$$i\hbar\frac{\partial}{\partial t}\hat{\Psi}(\mathbf{r},t) = [\hat{\Psi}(\mathbf{r},t),\hat{H}] \\ = \left[-\frac{\hbar^2\nabla^2}{2m} + V_{ext}(\mathbf{r}) + \int d\mathbf{r}'\hat{\Psi}^\dagger(\mathbf{r}',t)V(\mathbf{r}-\mathbf{r}')\hat{\Psi}(\mathbf{r}',t)\right]\hat{\Psi}(\mathbf{r},t). \tag{2.39}$$

2.5.1 Gross-Pitaevskii equation

The Gross-Pitaevskii equation constitutes the zeroth order of the Bogoliubov development, that is assuming $\hat{\Psi}' \equiv 0$. With this assumption, one can replace the operator $\hat{\Psi}$ with the classical field Φ_0. A further simplification of Eq.(2.39) comes from substituting the real two-body interaction potential $V(\mathbf{r}-\mathbf{r}')$ by the effective potential introduced previously in this chapter. This gives:

$$i\hbar\frac{\partial}{\partial t}\Phi_0(\mathbf{r},t) = \left[-\frac{\hbar^2\nabla^2}{2m} + V_{ext}(\mathbf{r}) + \int d\mathbf{r}'\Phi_0^*(\mathbf{r}',t)V_{eff}(\mathbf{r}-\mathbf{r}')\Phi_0(\mathbf{r}',t)\right]\Phi_0(\mathbf{r},t). \tag{2.40}$$

This equation is known as the Gross-Pitaevskii equation (GPE) [80, 81]. It is valid for a macroscopic occupation of the condensate. It can be used,at low temperature, to explore the macroscopic behaviour of the system, characterized by variations of the order parameter over distances larger than the mean distance between the atoms.

Contact interacting case Let us assume that the particles have a negligible dipole moment, and therefore their interaction can be expressed by the short-range effective potential of Eq.(2.20). Thus, $V(\mathbf{r}-\mathbf{r}') = g\delta(\mathbf{r}-\mathbf{r}')$, with $g = 4\pi\hbar^2 a/m$. The GPE (2.40) for the order parameter now reads:

$$i\hbar\frac{\partial}{\partial t}\Phi_0(\mathbf{r},t) = \left(-\frac{\hbar^2\nabla^2}{2m} + V_{ext}(\mathbf{r}) + g|\Phi_0(\mathbf{r},t)|^2\right)\Phi_0(\mathbf{r},t). \tag{2.41}$$

The stationary solution of the GPE (i.e. the ground state of the system with the many-body Hamiltonian (2.37), in mean-field approximation) can be obtained by writing the condensate wave function as $\Phi_0(\mathbf{r},t) = \phi(\mathbf{r})e^{-i\mu t/\hbar}$, where μ is the

chemical potential and ϕ is real and normalized to the total number of particles: $\int d\mathbf{r}\phi^2 = N_0 \simeq N$. Then the GPE (2.41) becomes:

$$\left(-\frac{\hbar^2\nabla^2}{2m} + V_{ext}(\mathbf{r}) + g\phi^2(\mathbf{r})\right)\phi(\mathbf{r}) = \mu\phi(\mathbf{r}). \tag{2.42}$$

This is typically referred to as the stationary Gross-Pitaevskii equation, and plays a central role in determining the static properties of a dilute BEC, as will be discussed below. The stationary GPE has the form of a "nonlinear Scrödinger equation", with a term proportional to the particle density $n(\mathbf{r}) = \phi^2(\mathbf{r})$. It is a single-particle equation describing how the wave function of each atom in the condensate is determined by the combined effect of the kinetic energy $-\frac{\hbar^2\nabla^2}{2m}$, the trapping potential $V_{ext}(\mathbf{r})$, and the mean-field exerted on a given atom at position $\mathbf{r}$ by the density of the other $(N-1)$ atoms at that point times the effective coupling, $g\phi^2(\mathbf{r})$. This explains the name "mean-field approximation" given to this treatment. Note that here the eigenvalue is the chemical potential (dE/dN), not the energy per particle (E/N), as it is for the usual (linear) Scrödinger equation.

One can study the properties of the ground state wave function in two limit cases: the one where interparticle interactions are very low with respect to the kinetic term, and therefore the nonlinear mean-field term in the stationary GPE can be neglected (non interacting limit), and the opposite case where (repulsive) interactions dominate over the kinetic energy, so that this latter term can be ignored. Before going into the calculations for these two cases, it is worth making a qualitative reasoning which allows to define a dimensionless parameter characterizing the relative strength of the atom-atom interaction compared to the kinetic energy. Because of its experimental relevance in the context of this thesis, the trapping potential is assumed to be harmonic. For simplicity, let us suppose that the harmonic potential is isotropic, with angular frequency ω_0: $V = m\omega_0^2 r^2/2$. In absence of interactions, the BEC matches the ground state of the harmonic oscillator potential, such that its extent R is equal to the *harmonic oscillator length*, defined as:

$$a_{ho} = \sqrt{\frac{\hbar}{m\omega_0}}, \tag{2.43}$$

and the mean kinetic energy is given by $\hbar\omega_0/4$. Let us now consider the effect of interactions perturbatively. The mean interaction energy per particle is of the order of $gn \sim gN/a_{ho}^3$. Now one can compare the total (for N particles) interaction energy $E_{int} \sim Ngn$ with the total kinetic energy $E_{kin} \sim N\hbar\omega_0/4$, and obtains the following relation:

$$\frac{E_{int}}{E_{kin}} \propto \frac{N|a|}{a_{ho}}. \tag{2.44}$$

The parameter $N|a|/a_{ho}$ expresses the importance of interatomic interactions with respect to the kinetic energy.

In the limit $N|a|/a_{ho} \ll 1$ interactions can be ignored. In the absence of interactions ($g = 0$), the condensate wavefunction is simply the Gaussian of the harmonic oscillator ground state. For a generic 3D harmonic confinement of the form:

$$V_{ext}(\mathbf{r}) = \frac{1}{2}m(\omega_x^2x^2 + \omega_y^2y^2 + \omega_z^2z^2) \tag{2.45}$$

where the three oscillator frequencies ω_i ($i = x, y, z$) may differ from each other,the condensate density reads:

$$n(\mathbf{r}) = \phi^2(\mathbf{r}) = N\left(\frac{m\omega_{ho}}{\pi\hbar}\right)^{3/2} e^{-\frac{m}{\hbar}(\omega_x^2x^2+\omega_y^2y^2+\omega_z^2z^2)}. \tag{2.46}$$

Here, $\omega_{ho} = (\omega_x\omega_y\omega_z)^{1/3}$ is the geometric average of the oscillator frequencies. The value of the density at the centre is proportional to N. The size of the cloud is instead independent of N, and is fixed by the harmonic oscillator length (2.43) for ω_{ho}.

If the atoms are interacting, the shape of the condensate density can change significantly with respect to the Gaussian. The central density is lowered (raised) by a repulsive (attractive) interaction and the radius of the atomic cloud consequently increases (decreases). This effect of the interaction has important consequences, not only for the structure of the ground state, but also for the dynamics and thermodynamics of the system (see, for instance [66]).

One should note that only large repulsive interactions ($a > 0$) are allowed within the GPE treatment. In the case of too large attractive interactions, the gas

would collapse leading to also very interesting phenomena (like the "Bose Nova", see ref. [82]). In this case other mechanisms, not included in the GPE, should be taken into account to describe the gas behavior (for instance, three-body losses and beyond mean-field effects [78]).

Thomas-Fermi approximation In the limit $N|a|/a_{ho} \gg 1$, the predictions of mean-field theory take a rather simple analytical form. Regarding the ground state, the effect of increasing the parameter $N|a|/a_{ho}$, with $a > 0$ is that the atoms are pushed outwards, the central density becomes rather flat, and the radius grows. As a consequence, the kinetic term in the GPE (2.42), proportional to $\nabla^2\sqrt{n(\mathbf{r})}$, takes a significant contribution only near the boundary of the density distribution and becomes negligible with respect to the interaction energy. Therefore, a better approximation for the condensate wave function in this limit may be obtained by solving the GPE (2.42) neglecting the kinetic energy term. The GPE in this case becomes an algebraic equation for the condensate density:

$$[V_{ext}(\mathbf{r}) + g\phi^2(\mathbf{r})]\phi(\mathbf{r}) = \mu\phi(\mathbf{r}). \tag{2.47}$$

The solution of the previous equation gives the density profile in the form:

$$n(\mathbf{r}) = \phi^2(\mathbf{r}) = \frac{\mu - V_{ext}(\mathbf{r})}{g} \tag{2.48}$$

in the region where $\mu > V_{ext}(\mathbf{r})$, and $n = \phi = 0$ outside. This is referred to as the *Thomas-Fermi (TF) approximation*. The boundary of the cloud is therefore given by the condition

$$V_{ext}(\mathbf{r}) = \mu \tag{2.49}$$

for which the density $n(\mathbf{r})$ vanishes. In the TF approximation the extension of the cloud in the three directions is given by the three semi-axes R_i obtained by inserting the harmonic potential (2.45) into Eq.(2.49):

$$R_i = \sqrt{\frac{2\mu}{m\omega_i^2}}, \qquad i = x, y, z. \tag{2.50}$$

The density (2.48) can thus be re-written as follows:

$$n(\mathbf{r}) = n_{TF}(0)\left(1 - \frac{x^2}{R_x^2} - \frac{y^2}{R_y^2} - \frac{z^2}{R_z^2}\right), \tag{2.51}$$

where $n_{TF}(0) \equiv \mu/g$ is the value of the density at the centre of the trap. Eq.(2.51) shows that the condensate density in the TF regime takes the form of an inverted parabola. The so-called TF radii R_i of Eq.(2.50) can be evaluated in terms of trap parameters once the chemical potential has been determined. The normalization condition on $n(\mathbf{r})$ provides a relation between the chemical potential and the total number of particles N:

$$\mu = \frac{\hbar\omega_{ho}}{2}\left(\frac{15Na}{a_{ho}}\right)^{2/5}. \tag{2.52}$$

Note that the chemical potential depends on the trapping frequencies, entering the potential V_{ext} only through the geometric average ω_{ho}. A convenient measure of the spatial extent of the cloud may be identified with the quantity $\bar{R} = (R_x R_y R_z)^{1/3}$. By combining equations (2.50) and (2.52), one gets:

$$\bar{R} = a_{ho}\left(\frac{15Na}{a_{ho}}\right)^{1/5}, \tag{2.53}$$

Therefore, $\bar{R}$ is larger than a_{ho}, and increases with N.

On the contrary, the value of the density at the center of the trap $n_{TF}(0)$ is typically much lower than the one predicted for noninteracting particles, $n_{ho}(0) = N/(\pi^{3/2}a_{ho}^3)$ and the ratio between the central densities in the two cases decreases with N.

A remarkable feature of Bose-Einstein condensates in the TF limit is that interactions can be important even though the gas is dilute. Indeed, for a typical BEC with $a \sim 10^{-3}$ μm, and an average density $\bar{n} \sim 10^{14}$ cm^{-3}, one has $\bar{n}a \ll 1$. This condition identifies a dilute gas. For a typical trapping frequency $\omega_{ho} \sim 100$ Hz, the harmonic oscillator length is ~ 1 μm. Therefore, for a BEC of $N = 10^5$ atoms, one has $\frac{Na}{a_{ho}} \sim 10^2$. This implies that the Thomas-Fermi approximation is very well justified in most experimental circumstances.

Finally, it is worth mentioning that the balance between the kinetic energy and the interaction energy of the condensate fixes a typical length scale, called the *healing length*, and indicated by ξ. It describes the minimum distance over which the condensate wave function recovers its bulk value when subjected to a localized perturbation (this explains the use of the term "healing" for this length). To derive an expression for the healing length, let us consider a BEC confined by a box with infinitely hard walls. At the wall, the wave function must vanish, and in the interior of the box the condensate density approaches its bulk value. If one indicates the spatial scale of the density variations by ξ, the kinetic energy per particle is of order $\hbar^2/2m\xi^2$, and it competes the interaction energy per partcile gn for:

$$\frac{\hbar^2}{2m\xi^2} = gn = \frac{4\pi\hbar^2 an}{m} \tag{2.54}$$

which gives

$$\xi = \frac{1}{\sqrt{8\pi an}}. \tag{2.55}$$

In typical experiments the healing length is of the order of 1 μm, and therefore it is much larger than the scattering length a.

The healing length plays an important role in the Bogoliubov theory of the elementary excitations of a weakly-interacting BEC, as will be shown in Chapter 4.2.

2.5.2 Non-local Gross-Pitaevskii equation for dipolar systems

As already pointed out, dipolar interactions are expected to change many of the properties of a BEC. Here I will present the *non-local* Gross-Pitaevskii equation (NLGPE) needed for a mean-field description of dipolar BECs, and its consequencies on the shape and size of the ground state of the system.

Here we consider Eq.(2.40) with $V_eff(\mathbf{r}-\mathbf{r}') = g\delta(\mathbf{r}-\mathbf{r}') + V_{dd}(\mathbf{r}-\mathbf{r}')$, where $V_{dd}(\mathbf{r}-\mathbf{r}') = \frac{\mu_0\mu_m^2}{4\pi}\frac{1-3\cos^2\theta}{|\mathbf{r}-\mathbf{r}'|^3}$.

This gives a generalized form of the GPE (2.41) for the order parameter, which

includes the dipolar contribution to the mean-field interaction energy, and is typically referred to as the NLGPE (non-local Gross-Pitaevskii equation):

$$i\hbar\frac{\partial}{\partial t}\Phi_0(\mathbf{r},t) = \left(-\frac{\hbar^2\nabla^2}{2m} + V_{ext}(\mathbf{r}) + g|\Phi_0(\mathbf{r},t)|^2 + U_{dd}(\mathbf{r},t)\right)\Phi_0(\mathbf{r},t), \qquad (2.56)$$

where

$$U_{dd}(\mathbf{r},t) = \int d\mathbf{r}' V_{dd}(\mathbf{r}-\mathbf{r}')|\Phi_0(\mathbf{r}',t)|^2. \qquad (2.57)$$

This term is a convolution of the density $n(\mathbf{r},t) = |\Phi_0(\mathbf{r},t)|^2$ with the DDI potential. Eq.(2.56) is non-local due to the long-range character of the dipolar interaction. It is an integro-differential equation, much more complicated to solve with respect to the GPE, even numerically. Let us only focus here on the stationary solution of the NLGPE. Following the treatment of the previous section, in the time-independent case, the NLGPE takes the form:

$$\left(-\frac{\hbar^2\nabla^2}{2m} + V_{ext}(\mathbf{r}) + g\phi^2(\mathbf{r}) + \int d\mathbf{r}' V_{dd}(\mathbf{r}-\mathbf{r}')\phi^2(\mathbf{r}')\right)\phi(\mathbf{r}) = \mu\phi(\mathbf{r}). \qquad (2.58)$$

In the TF approximation, where the kinetic energy term can be neglected, the density distribution $n(\mathbf{r})$ satisfies the integral equation

$$\mu = V_{ext}(\mathbf{r}) + gn(\mathbf{r}) + \int d\mathbf{r}' V_{dd}(\mathbf{r}-\mathbf{r}')n(\mathbf{r}'), \qquad (2.59)$$

which is a generalization of Eq.(2.48) to dipolar systems. A striking effect of the DDI is to elongate the condensate along the direction z along which the dipoles are aligned. This effect, called *magnetostriction* [83], that is a change of the shape and volume of the atomic cloud due to internal magnetic forces, can be understood in a simple way for an isotropic harmonic trap with $V_{ext} = m\omega_{ho}^2 r^2/2$, and treating the dipolar interaction as a perturbation ($\epsilon_{dd} \ll 1$). To zeroth order, that is in the absence of DDI, Eq.(2.59) has the solution $n^{(0)}(r) = (\mu - m\omega_{ho}^2 r^2/2)/g \equiv n_{TF}(0)(1 - r^2/R^2)$, where R is the TF radius of the condensate. By inserting this $n^{(0)}(r)$ into the last term of Eq.(2.59) and carrying out the integration over $\mathbf{r}'$, one

obtains the dipolar contribution to the energy of an atom at point $\mathbf{r}$ in the form:

$$U_{dd}^{(0)}(\mathbf{r}) = \int d\mathbf{r}' V_{dd}(\mathbf{r}-\mathbf{r}') n^{(0)}(r'). \tag{2.60}$$

Thus, from Eq.(2.59), one gets:

$$n(\mathbf{r}) = \frac{\mu - V_{ext}(\mathbf{r}) - U_{dd}^{(0)}(\mathbf{r})}{g}. \tag{2.61}$$

Since $U_{dd}^{(0)}(\mathbf{r})$ is anisotropic, the cloud is distorted with respect to the non-dipolar case. It can be demonstrated (see ref.[66]) that, to first order in ϵ_{dd}, the TF solution for the ground state of a dipolar BEC in a spherical trap has still an inverted parabola shape as in the case of a purely contact interacting gas, of the form:

$$n(\mathbf{r}) = n_{TF}(0)\left(1 - \frac{x^2}{R_{dd,x}^2} - \frac{y^2}{R_{dd,y}^2} - \frac{z^2}{R_{dd,z}^2}\right), \tag{2.62}$$

but with the TF radii in the three spatial directions x, y and z containing the explicit dependence on ϵ_{dd}:

$$R_{dd,x} = R_{dd,y} \simeq R(1-\epsilon_{dd}/5) \qquad R_{dd,z} \simeq R(1+2\epsilon_{dd}/5). \tag{2.63}$$

Eq.(2.63) shows that the condensate is elongated along the direction of the dipoles. One can then calculate to first order in ϵ_{dd} the mean-field DDI potential (2.57) created by the density distribution (2.64), and finds [77]:

$$U_{dd}(\mathbf{r}) = \epsilon_{dd}\frac{m\omega_{ho}^2}{5}(1-3\cos^2\theta)\begin{cases} r^2 & \text{if} \quad r < R \\ \frac{R^5}{r^3} & \text{if} \quad r > R \end{cases} \tag{2.64}$$

Thus, the dipolar mean-field potential has the shape of a saddle, with minima located on the z axis, along which the dipoles are oriented. It is therefore energetically favorable for the cloud to become elongated along z, in order to maximize the attractive part of the DDI, and therefore minimize the total potential energy.

The perturbative treatment can be extended to anisotropic traps. It is worth noticing that in the case of a dipolar BEC, the *cloud* aspect ratio $R_{dd,x,y}/R_{dd,z}$ differs from the *trap* aspect ratio, due to the elongation induced by the DDI discussed

above, whereas for non-dipolar systems, the two aspect ratios coincide. The trap aspect ratio is typically defined as the ratio of the harmonic oscillator lengths, or equivalently the inverse of the corresponding trapping frequencies, along the direction longitudinal to the dipoles and perpendicular to them, and it is equal to 1 for isotropic traps ($\omega_x = \omega_y = \omega_z$). As we will see in Chapter 4, because of the anisotropic character of the DDI, the geometry of the trapping potential plays a crucial role in determining the static and dynamic properties of dipolar BECs.

Chapter 3

Design of a new vacuum apparatus for the realization of tunable Bose-Einstein condensates

This chapter presents the design of the vacuum system for a new experimental apparatus for producing BECs of ^{39}K atoms, to be constructed in Florence. I will give technical descriptions of the various components of the designed system, like the vacuum chambers, the vacuum pumps and the magnetic coil configurations. The experimental steps towards the realization of the BEC that are planned for this experiment are also presented, since they fundamentally determine the choices of design. The scheme includes a vapour cell with a solid potassium sample as atom source, where a pre-cooling and trapping stage in a 2D MOT is planned, a subsequent 3D MOT, followed by the loading of the atoms in a in-vacuum optical resonator, and finally the optical transport of the atoms in the science chamber. This latter step will be achieved by moving the focus of an optical dipole trap beam through the use of lenses with a tunable focal length. At the end of the chapter I will present a preliminar experimental test of the optical setup designed for the optical transport.

3.1 Design of the vacuum system

The knowledge of the internal atomic structure of K, together with the experimental techniques typically used to bring a gas of K atoms to degeneracy, is essential for the design. At the University of Florence and LENS, the route towards the Bose-Einstein condensation of ^{39}K in a single species experiment is well estabilished [84]. In my work, several parts of the vacuum system as well as its fundamental structure have been inspired by the "K39 Experiment" at LENS, while other parts have been designed from scratches.

When designing a vacuum system for the production of a degenerate atomic gas, one has already to think of which kind of experiments wants to perform on that system. The following major requirements have been kept in mind during the design of the vacuum apparatus:

- The pressure in the vacuum chambers should be low enough to allow for a lifetime of the atomic sample of at least few seconds. The lifetime of the sample is proportional to the inverse of the background pressure. A simple calculation based on the background collision cross section yields a lifetime of the atomic sample between 2 and 8 s (depending on the chemical composition of the background gas) for a pressure of 10^{-9} mbar, that is within the ultra-high vacuum (UHV) regime.

- The system should be sufficiently compact to allow for a high repetition rate of the experimental sequence for the production of the BEC.

- A wide optical access onto the atoms is needed to allow the use of many trapping beams as well as the implementation of high spatial resolution imaging and laser speckles for creating disordered potentials (see for instance [85]).

- The vacuum system has to be designed in such a way that a proper configuration of magnetic field coils can be placed around the vacuum chambers, allowing for the creation of homogeneous magnetic fields up to 400 G for tuning of interactions via Feshbach resonances and gradient fields up to 30 G/cm for MOT operation. The previous maximal desired values for the magnetic field and the magnetic field gradient are taken from [84].

- Since potassium atoms are magnetic, particular care has to be taken in order to reduce any magnetic field fluctuation or instability, in particular very close to the atoms. For this reason, low-magneticity building materials, like the steinless steel compounds SS304 or SS316, have to be employed for vacuum components such as chambers, viewports, valves and bellows.

In order to satisfy these conditions, a scheme with three vacuum chambers has been designed (Fig.3.1).

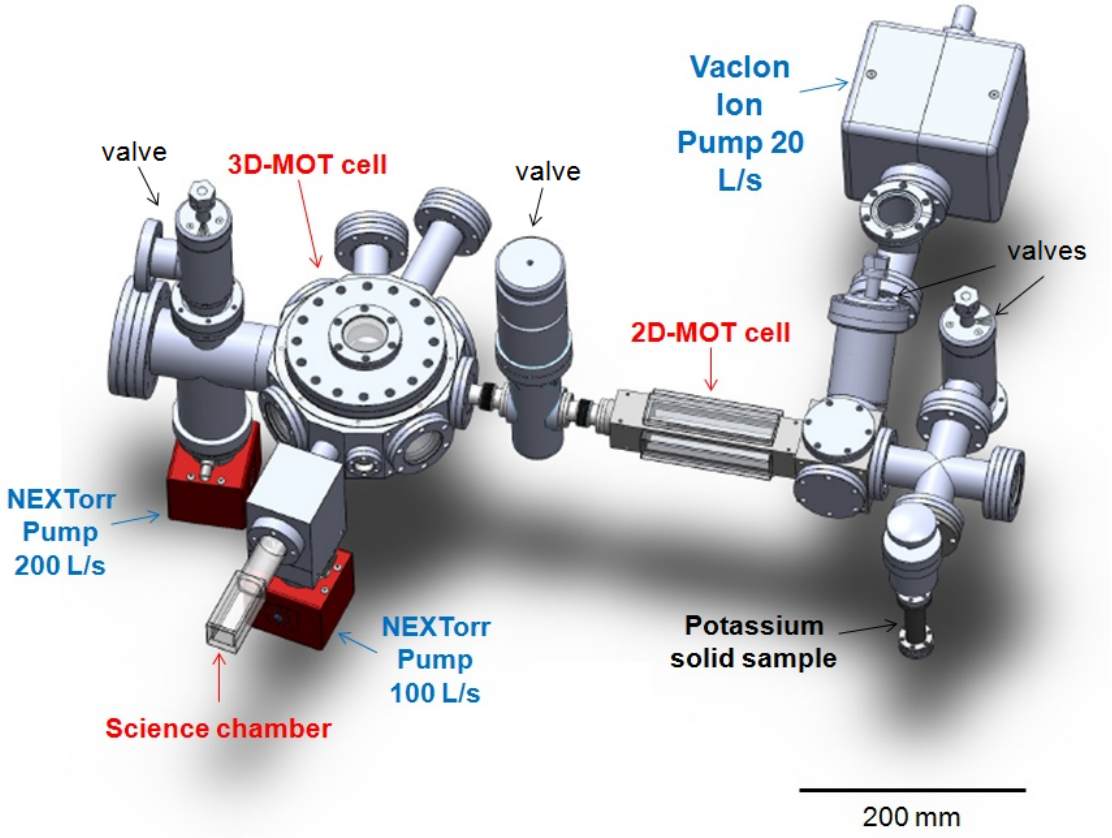

Figure 3.1: Overview of the vacuum system. The three chambers are indicated as 2D-MOT, 3D-MOT and science chamber. The vacuum pumps, the valves and the nipple containing the potassium sample are also shown.

The first cell (which serves as a vapour cell, see below) is meant to host a bi-dimensional magneto optical trap (2D-MOT) used as a first cooling and trapping stage for the atomic gas. A relatively high pressure of potassium vapour of 1.3×10^{-8} mbar at room temperatue [86] ensures a fast loading rate into the 2D-MOT.

The (high flux) atomic beam will then be pushed towards the second cell, where a three-dimensional magneto optical trap (3D-MOT) will be performed. Finally, the atoms will be optically transferred into the third cell, which constitutes the science chamber of the experiment. In the science chamber a very large optical access onto the atoms can be achieved, due to the shape of the cell and to the absence of MOT laser beams.

Following the approach described in [47], the 2D-MOT and 3D-MOT are planned to be operated on the D_2 line of potassium, with a transition wavelength of 767 nm, and a linewidth of $\approx 2\pi \times 6$ MHz [42], for which a commercially available diode laser source will be used.

In the following, the various parts of the vacuum apparatus and the pumping scheme to achieve UHV pressures in the system, are described in detail.

3.1.1 Vacuum chambers

2D-MOT cell The design of the 2D-MOT cell is taken from [47, 87]: four rectangular 126×31 mm^2 N-BK7 anti-reflection coated windows, providing optical access to four transverse trapping beams, are glued on a metallic rectangular frame, machined from a low magneticity titanium block. The choice of the N-BK7 material for the windows is due to a similar thermal expansion coefficient of titanium and N-BK7, which allows to minimize stresses on the windows in the metal-to-glass contact region during the baking of the cell. The potassium vapor can be released into the 2D-MOT chamber by heating a solid sample up to 100°C for few days. In this way, the oxide layer that forms on the surface of the metal melts, and potassium is released in the cell.

3D-MOT cell The 3D-MOT chamber has been designed completely from scratches. The chosen building material is the very low-magnetic stainless steel aisi 316L. In this chamber several steps of the experimental procedure towards the Bose-Einstein condensation of the atomic sample will take place:

1. Trapping and cooling of the atoms in a 3D-MOT;

2. Loading in a deep optical trap created by using a in-vacuum optical resonator (see section 3.3) and initial evaporative cooling;

3. Loading in a far-off resonant optical dipole trap. This trap will be also used to transfer the atoms from the 3D-MOT chamber to the science cell (as described in section 3.4).

In order to provide optical access for all the necessary laser beams, a geometry of the cell with six optical axes has been designed. It is sketched in Fig.3.2.

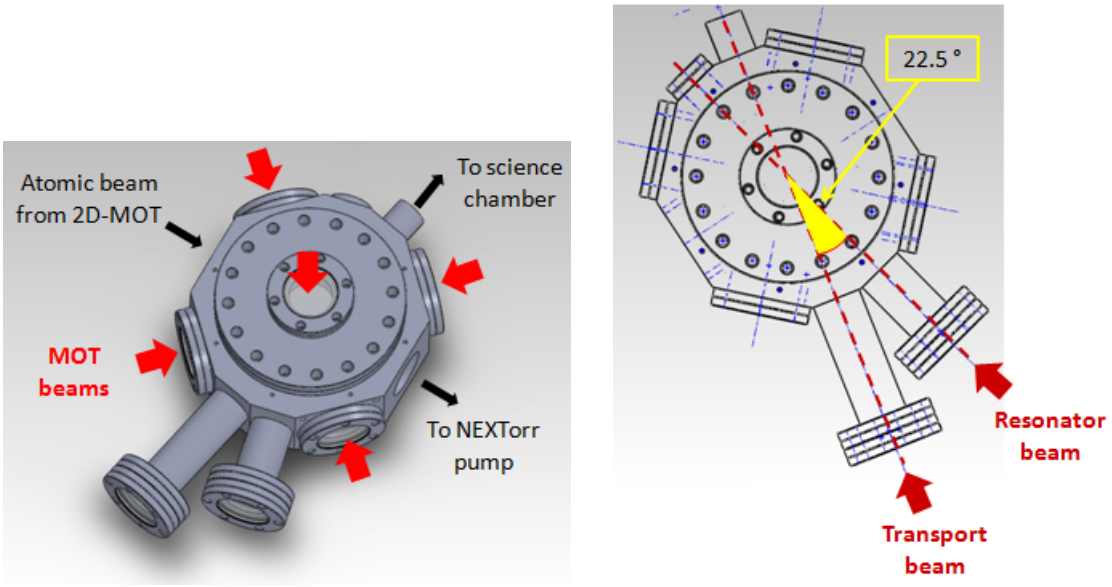

(a) (b)

Figure 3.2: Schematic view of the laser beams configuration in the 3D-MOT cell. (a) MOT beams. The sixth beam is counterpropagating with respect to the one coming from the top, and is hidden in the figure. (b) Optical trap beams for resonator and transport. The two optical axes forming an angle of 22.5° are shown.

In order to achieve an efficient loading of the atomic beam coming from the 2D-MOT in the 3D-MOT, large diameter MOT beams have to be used. In the present setup the idea is to employ MOT beams with a diameter of 25 mm, entering the vacuum chamber through standard CF40 viewports, whose effective view diameter is 35 mm. This means that no other laser beams can enter the cell from

the same viewports used for the MOT beams. The two optical axes needed for the resonator and the dipole trap beams are therefore obtained in the chamber by modifying its originally octagonal shape into a decagonal one, as shown in Fig. 3.2(b). The small angle of 22.5° between these two axes should allow for an efficient loading of the atoms from the resonator trap into the dipole trap, as will be discussed later (see section 3.4).

The 3D-MOT chamber has been manufactured just before I left Florence. Fig. 3.3 shows a picture of this cell, where I have already assembled most of the flanges and vacuum viewports.

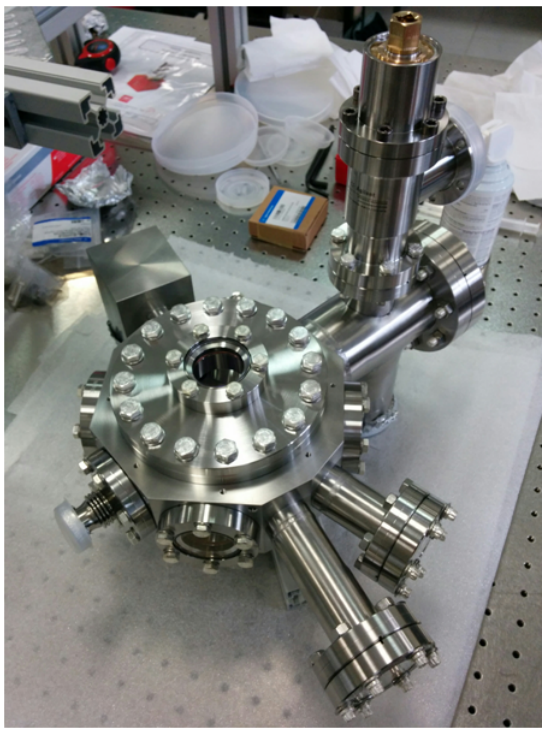

Figure 3.3: Picture of the 3D-MOT cell for the new vacuum system. The custom made cell is made up of stainless steel aisi 316L. It has been manufactured by the MORIMECCANICA srl, Parma (Italy). The flanges, viewports, and all-metal valve visible in the picture have been assembled to the cell by me.

Science chamber The science chamber of the experiment is a rectangular glass cell with dimensions 30 × 30 × 60 mm^3, which is connected to the rest of the

apparatus via a 57 mm long glass cylinder (see Fig.3.1). The size and shape of the cell have been designed in order to fulfill three main requirements. First, large optical access onto the atoms is needed in this cell in order to employ several laser beams: a crossed optical dipole trap, laser speckles, high resolution absorption imaging, and eventually optical lattices. Second, large Feshbach coils have to be placed close to the cell for tuning of the atomic interactions. Third, the distance through which the atomic cloud can be efficiently transported between two points of the vacuum system is limited by atom losses and heating of the atomic sample during the transport. On the basis of an already existent experiment with a similar optical transport setup [88], it can be estimated that the maximal transport distance for the present system, allowing to have an efficient transport, is around 300 mm. This poses a constrain on the length of the glass cylinder and the cell itself.

3.1.2 Vacuum pumps

Fig.3.1 shows the three vacuum pumps that will be used to pump out the background gas from the vacuum system and reach the desired UHV pressures in the chambers. In between a vacuum chamber and the next one, a differential pumping stage reduces the pressure progressively, in order to get the minimum pressure over the whole apparatus in the final glass cell. The achievement of sufficiently low pressures will require a baking procedure of all the parts of the vacuum apparatus at a temperature higher than 100 °C for several days, in order to eliminate condensed water laying onto the internal surfaces of the system and most of the hydrogen accumulated in the steel components during their fabrication process.

The pump used for the 2D-MOT cell is a Vaclon Diode ion pump from *Agilent Technologies*, with a nominal pumping speed of 20 L/s. This pump is particularly indicated for pumping of active gases such as N_2, O_2, CO_2, H_2. In particular, H_2 turns out to be the main residual gas at UHV pressures. The effective pumping speed at the chamber decreases to 6.8 L/s due to the conductance of the connections (all the values are calculated for air). By calculating the outgassing of the various surfaces, an achievable pressure of 1.5×10^{-9} mbar in the 2D-MOT cell can be estimated [47].

For the pumping of the 3D-MOT cell and the science chamber the plan is to use two NEXTorr pumps from *Saes Getters*, with different nominal pumping speeds of 200 L/s and 100 L/s, respectively. These pumps combine a non-evaporable getter (NEG) cartridge with a small ion pump. The getter element provides very large pumping speed and capacity and acts as the main pump for active gases, in particular for hydrogen. Instead the ion pump has the task to remove noble gases and methane, which are not pumped by the NEG. The NEXTorr pumps have a much more compact design with respect to standard ion pumps, which also means smaller magnets, and therefore a convenient reduction of stray magnetic fields close to the vacuum system.

The expected effective pumping speed at the two chambers can be calculated by knowing the nominal pumping speed of the pumps and the conductances of all the tubes through which the pumps are connected to the chambers. In analogy with electric circuits, the inverse of the conductances of a series of tubes or components (such as a pump) sum up to give the inverse of the total conductance of the series [89]:

$$\frac{1}{C_{eff}} = \frac{1}{C_1} + \frac{1}{C_2} + \frac{1}{C_3} + ... + \frac{1}{C_{pump}} \tag{3.1}$$

where C_{eff} is the effective pumping speed at the chamber, C_1, C_2, C_3, ... are the conductances of all the components that separate the chamber from the pump, which depend on the geometry of the components, and C_{pump} is the nominal pumping speed of the pump.

Using Eq.(3.1) it is possible to estimate the effective pumping speed at the two chambers in the designed vacuum system. The effective pumping speed of the NEXTorr pumps turns out to be 50 L/s at the 3D-MOT chamber and 42 L/s at the science chamber, respectively.

Once the effective pumping speed at a chamber is known, the achievable pressure in the chamber can be estimated. It is worth noticing that, after the baking of the system, the main residual gas in the vacuum chambers is expected to be the potassium itself, whose pressure at room temperature is on the order of 10^{-8} mbar. Therefore, to calculate the ultimate pressure in the chambers one has to consider the flux of potassium atoms entering the chamber (expressed in units of

mbar × L /s) and divide it by the effective pumping speed at the chamber.

- In the case of the 3D-MOT cell, assuming an incoming atomic flux of 10^{11} atoms/s (see ref. [84]), which corresponds to 10^{-8} mbar × L/s [1], and dividing this quantity by 50 L/s, one gets an estimated achievable pressure of 2×10^{-10} mbar.

- To estimate the incoming atomic flux in the final glass cell, one divides the pressure in the 3D-MOT chamber by the conductance of the 16 mm diameter tube that connects the 3D-MOT chamber to the differential pumping stage provided by the 100 L/s NEXTorr pump (visible in Fig.3.1). The resulting flux of 12.6×10^{-10} mbar × L/s has to be divided by the effective pumping speed at the science chamber (42 L/s), to obtain a ultimate pressure in the final cell of 3×10^{-11} mbar.

The calculated achievable pressures in the 3D-MOT cell and science chamber are whitin the UHV regime, and are expected to provide a lifetime of the atomic sample of several seconds, which allows to perform experiments.

3.2 Design of the magnetic field coils

Different sets of coils have to be used in the experiment. In particular, around each vacuum chamber a proper configuration of magnetic coils is needed for magnetic trapping of atoms and/or Feshbach tuning of the interactions. The design of the coils has to take into account the different operational requirements as well as the experimental constraints of the apparatus. It has been performed by using the RADIA package for Wolfram Mathematica [90] with which it is possible to simulate the magnetic field created by a given configuration of coils.

Magnetic coils at the 2D-MOT chamber For bi-dimensional trapping of the atoms, one needs to create a homogeneous magnetic field along the longitudinal axis of the 2D-MOT cell (y-axis in the experimental apparatus, see Fig.3.4 for

[1] The density of 10^{16} atoms/cm^3 of air corresponds to a pressure of approximately 1 mbar.

reference), with zero field on the axis. Such a configuration can be realized by using two pairs of rectangular coils with the long side parallel to the y-axis, and the coils' axes along x for one pair and along z for the other one. To realize magneto-optical trapping, the current has to flow in opposite directions for coils facing each other (see section 1.3.3). Moreover, if the magnetic field lines are pointing inside the cell for one pair of coils, they have to point outside the cell for the other one, such that the magnetic field gradients generated by the two pairs of coils sum up along the coils' axes x and z, while they subtract to zero along the 2D-MOT y-axis. The coils configuration around the 2D-MOT cell is sketched in Fig.3.4(a).

The following parameters for the coils allow to create magnetic field gradients of up to 10 G/cm along the z-axis:

- Distance between the closest faces of each pair of facing coils: 69 mm (the 2D-MOT cell is 40 mm wide along x and z, then the minimum distance between each pair of coils is limited by the space needed for the support of the coils)
- Height of each coil $\simeq$ 23 mm.
- Width of each coil $\simeq$ 5.7 mm.
- Applied current: 5 A (around 1 W dissipated power, calculated for steady state operation at the indicated current).

Assuming to use a isolated copper wire with a rectangular section of 3.15 $\times$ 1.25 mm^2 to wind up the coils, each of the four 2D-MOT coils will be made up of 7 axial windings and 4 radial windings.

Magnetic coils at the 3D-MOT chamber To realize the 3D-MOT, a single pair of circular coils with axis along z and current flowing in opposite directions is needed. This configuration provides a certain magnetic field gradient (depending on the applied current) along the coils' axis and half of its value in the radial direction. However, at the 3D-MOT chamber, not only MOT coils have to be employed. In fact, after the MOT operation, the atoms will be loaded into the

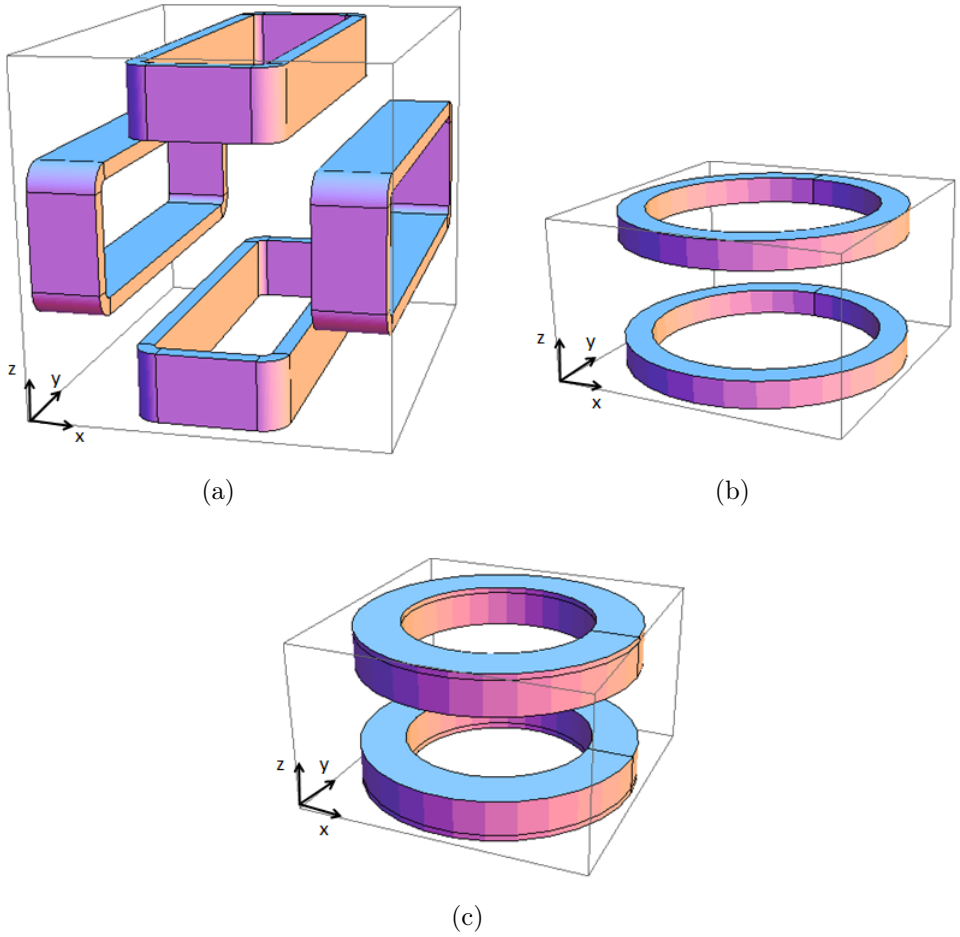

Figure 3.4: Sketch of the magnetic field coils in the experiment. Magnetic coils configuration at 2D-MOT cell (a), 3D-MOT cell (b) and science chamber (c). The different sets of coils are not drawn in scale.

optical resonator, where a first stage of evaporative cooling will be performed. In the case of potassium, the collisional rate at zero magnetic field is too low to allow an efficient evaporative cooling, therefore the use of Feshbach resonances is needed to tune the s-wave scattering length towards high positive values and achieve an efficient evaporation. A pair of coils in Helmholtz configuration is thus needed for Feshbach tuning of interactions. The Helmholtz configuration means that the current circulates in the same direction in the two colis, and the distance between the coils equals the coil radius. The magnetic field generated at the center of the coils is thus homogeneous.

In order to keep the experimental setup as more compact as possible, the idea is to use the same set of coils both for creating the gradient during the MOT cycle and for creating the homogeneous Feshbach field in the successive evaporation in the resonator. A relay system with a fast switching time[2] will allow to change the direction of the current in one of the coils, passing from the anti-Helmholtz (gradient) configuration to the Helmholtz (homogeneous) one.

The size of the coils is determined by their distance. For a given applied current, the highest magnetic field and magnetic field gradient are obtained when the coils are as closest as possible to each other. In order to fulfill the Helmholtz condition, this also means that the coils are as smaller as possible, and therefore they dissipate low power and can be easily cooled down via a water cooling technique. However, the chamber itself poses some limitations on how close the coils can be. In the present setup, in order to place the coils as close as possible to each other, the plan is to lean the coils directly on the chamber, around the CF100 flanges that constitutes the superior and inferior parts of the 3D-MOT cell.

According to the experimental procedure described in [84], during the MOT cycle a magnetic field gradient of around 10 G/cm is applied. At the end of the MOT operation, the atoms occupy the three levels of the $F = 1$ manifold. In order to have a fully polarized sample with all the atoms in the same Zeeman sublevel, a quadrupole field of 30 G/cm is applied instantly. As a consequence, approximately two thirds of the atoms are lost in the $|F = 1, m_F = 0, +1 >$ states and a fully pure sample is created in the $|F = 1, m_F = -1 >$ magnetically trappable state. In the experiment described in [84], the sample needs to be polarized in a magnetically trappable state after the MOT cycle, because then the atoms are loaded in a quadrupole trap with a high magnetic field gradient which is used to magnetically transfer the atoms between two vacuum chambers. In the present case, even if no magnetic transport has to take place, the polarization of the sample in the $|F = 1, m_F = -1 >$ state could be useful for the tuning of interactions via a Feshbach resonance. In fact, there exists a broad Feshabch resonance (with a width of ≈30 G) at an easily accessible magnetic field of around 160 G for atoms in the $|F = 1, m_F = -1 >$ state [27].

[2] A switching time on the order of 100 μs, much smaller than the typical time for an experimental cycle, has been obtained with a similar setup in [47].

The goal in designing the coils at the 3D-MOT chamber is therefore to create magnetic field gradients of up to 30 G/cm when the coils are operated in the anti-Helmholtz configuration, and homogeneous fields of up to 160 G when the Helmholtz configuration is employed. The simulations carried out with RADIA insure that the previous requirements can be fulfilled by using magnetic coils with the following parameters:

- Distance between the closest faces of the two coils: 75 mm (73 mm is the heigth of the 3D-MOT cell, then 1 mm of isolating layer is considered between each coil and the chamber).
- Height of each coil $\simeq$ width of each coil: 20 mm.
- Applied current: 17.7 A (around 80 W dissipated power for steady state operation at the indicated current) when operating the coils in Helmholtz configuration, and 20 A (around 100 W dissipated power for steady state operation) when using the anti-Helmholtz configuration.

In terms of axial and radial windings, the 3D-MOT coils will be made up of 6 axial windings and 16 radial ones.

Fig.3.5 shows the simulated magnetic field along the z-axis obtained for the 3D-MOT coils using the above parameters.

Magnetic coils at the science chamber In the science chamber the final stage of the evaporative cooling towards the Bose-Einstein condensation of the atomic sample will take place. As previously stated, to achieve an efficient evaporation process, it is crucial to properly tune the s-wave scattering length. This requires a pair of Feshbach coils to be employed around the science chamber. Once the degenerate regime has been reached, the Feshbach coils will be used to control and tune the interactions between the atoms while performing experiments. In order to eventually be able to reach the condensation in each of the three magnetic sublevels m_F of the hyperfine ground state $F = 1$ manifold, the Feshbach coils have to be designed such that they can provide a homogeneous magnetic field up to around 400 G [84, 27]. Thanks to the small dimension of the glass cell, the two

Feshbach coils can be placed very close to each other. The following parameters for the Feshbach coils turn out to give the desired homogeneous magnetic field of 400 G at the center of the chamber, with a relatively low dissipated power:

- Distance between the clostest faces of the two coils: 34 mm (30 mm is the heigth of the glass cell, then 2 mm are left between each coil and the chamber as a safe distance in order to protect the delicate chamber from possible contact with the coils).
- Height of each coil : 18.9 mm.
- Width of each coil: 25 mm.
- Applied current: 20 A (around 72 W dissipated power for steady state operation at the indicated current).

Beside the achievement of the control of interactions by using Feshbach coils, in the science chamber the atoms have to be retained against gravity. The gravity field exerts a magnetic field gradient of $\simeq$ - 7 G/cm, along the vertical (z-) direction. In the 2D-MOT and 3D-MOT chamber this is already compensated by the quadrupole field (even if it is possible to use additional coils to specifically compensate the effect of gravity). Since no quadrupole trap is needed in the final cell, a proper coil configuration for the gravity compensation has to be designed. A simple option considers to use a single layer (single axial winding) of each of the two Feshbach coils for the gravity compensation purpose. For instance, the upper layer of the top coil and the lower layer of the bottom coil can be controlled separately with respect to the remaining layers that form the Feshbach coils. In these pair of "single-layer" coils it is possible to apply a current flowing in opposite directions, such that to create a (positive) magnetic field gradient along the coil axis, which is parallel to the z-axis, and can therefore compensate for the gradient induced by gravity. In Fig.3.4(c) the coil configuration at the science chamber is sketched. If a current of 8.5 A is applied in opposite directions to the two outer layers of the Feshbach coils, a magnetic field gradient of $\simeq$ +6.7 G/cm is generated, that can be used to compensate the gradient induced by gravity.

The Feshbach coils will be made up of 6 axial and 20 radial windings, while

for the compensation coils a sinlge axial winding and 20 radial windings will be employed.

During operation the magnetic coils will heat up, therefore a proper cooling mechanism is needed. For all the coils in the experiment the expected dissipated power during steady state operation is calculated to be $\leq$ 100 W. In a normal experimental cycle the coils will be operated in pulse mode (they will be switched on and off on timescales of few seconds), therefore the expected dissipated power at each cycle is much lower than 100 W for all the coils. On the other side, one has to think that many experimental cycles have to be performed during a typical working day when the experiment is running, and the coils get unavoidably heated. All this considered, the decision has been made to use a water cooling mechanism for the coils at the 3D-MOT chamber and science chamber which consists of placing each coil in a alluminium box, where there is a separated duct through which cold water can flow. Thus, coils can be put in thermal contact with water and get cooled during operation. For the 2D-MOT chamber coils, the calculated dissipated power is so low that no water cooling mechanism is planned. However, the support of these coils is made in alluminium, therefore it can provide an heat sink for the coils.

3.3 Optical resonator

In many ultracold atomic experiments, as, for instance, in the ERBIUM experiment described in Chapter 4.3.1, at the end of the MOT operation the atoms are loaded directly into a single-beam or a crossed optical dipole trap, where evaporative cooling towards the degeneracy can be performed. Therefore, both the 3D magneto-optical trapping and the trapping in the optical dipole trap occur in the same chamber. In the present case instead, the idea is to use a optical dipole trap to first transfer the cold atomic cloud to the science chamber, and only there perform evaporative cooling to create the BEC. This will provide a larger optical access onto the atoms. To be efficient, the optical transport, which will be discussed later, requires a sufficiently small waist of the optical dipole trap, on the order of 50 μm [88] in order to provide high enough trapping frequencies and thus

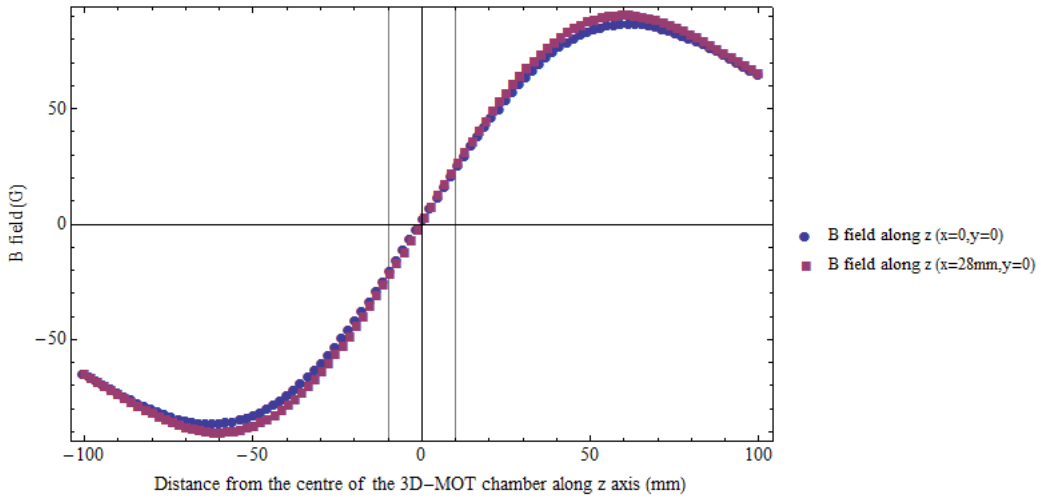

(a)

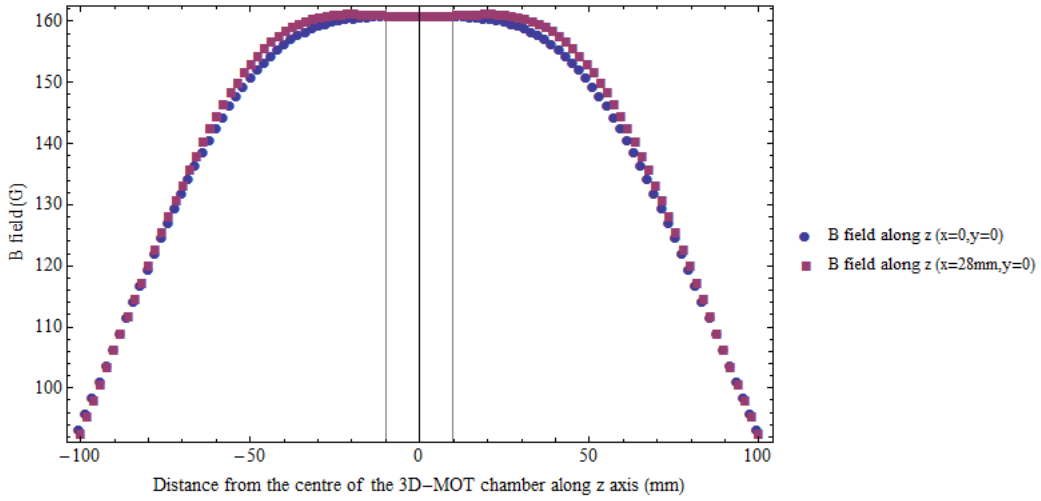

(b)

Figure 3.5: Simulated behaviour of the magnetic field at the center of the 3D-MOT chamber for two different coil configurations. (a) A magnetic field gradient of up to 30 G/cm can be created when the coils are employed in anti-Helmholtz configuration. (b) When the coils are in Helmholtz configuration, a homogeneous magnetic field of up to 160 G can be generated at the center of the chamber. In (a) and (b) the two vertical solid lines are used as a reference to indicate a region of 20 mm (from -10 mm to 10 mm) around the center of the chamber along the z-axis. The blue points represent the magnetic field along z calculated on the z-axis ($x = 0$, $y = 0$), while the purple points describe the behaviour of the magnetic field along z, 28 mm far from the z-axis, at ($x = 28$ mm, $y = 0$).

reduce as far as possible the losses of atoms during the transport. This value of the waist is much smaller than a typical radius of a potassium MOT of around 2 mm (see, for instance, [84]). As a consequence, the direct loading of the MOT into the transport beam would not be efficient in the present system, and an intermediate step is needed to confine the atoms in a smaller volume before the loading into the transport beam. Another dipole trap, with a larger waist almost matching the size of the MOT radius could in principle be used as the intermediate step, but in this case, a very deep trap would be necessary in order to have sufficiently high trapping frequencies, and this implies the use of very high power lasers of several tens of Watts. However, high power lasers typically introduce some side effects into the system, as for instance the thermal lensing effect on the viewports of the vacuum chamber, and their use should be minimized as far as possible.

The decision has been made to use a high finesse Farbry-Perot cavity mounted inside the 3D-MOT chamber, as the intermediate step for confining the atoms after the MOT cycle and before the optical transport. Inside the cavity it is possible to achieve a trapping depth much larger than the mean kinetic energy of the atoms in the MOT, even using laser powers of few Watts (< 4 W), thanks to the amplification of the power achieved when the laser radiation is resonantly coupled into the cavity. Moreover, the geometry of the resonator can be chosen in order to maximize the trapping volume for the best possible overlapping with the MOT volume, taking into account the spatial constraints of the vacuum chamber where the resonator has to be mounted.

The design of the resonator has been inspired by the one already built in the Ytterbium experiment at LENS [91]. Fig.3.6 shows a skectch of the cavity placed inside the 3D-MOT chamber.

The idea is to screw the mounts for the cavity mirrors on the CF100 flange which constitutes the inferior part of the chamber. The length of the cavity has been chosen to be 90 mm, which is the maximum possible length, limited by the presence of the gasket (in brown in Fig.3.6). The resonator has to be simmetric, so that the waist of the beam is at the centre of the cavity, where the atomic cloud is. The value of the waist of the resonator has to be chosen in order to be able to load as many atoms as possible from the MOT into the resonator, without prejudicing

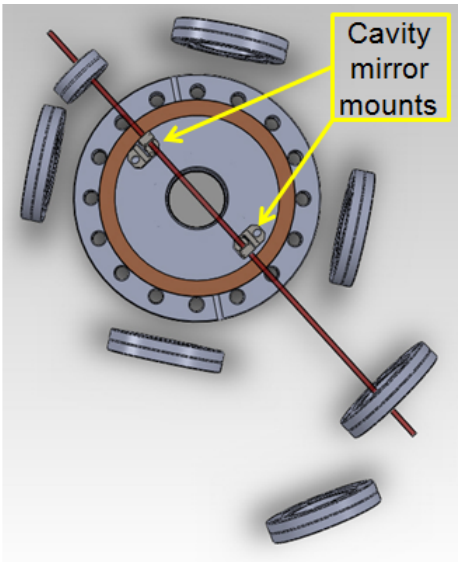

Figure 3.6: Top view of the in-vacuum optical resonator. For reference, the viewports of the 3D-MOT chamber are visible in the sketch. The two supports for the cavity mirrors are mounted on the CF100 flange attached to the chamber. The red cylinder indicates the optical axes of the resonator, which in this figure is not parallel to the axis of the entrance and exit viewports. This difference is shown to demonstrate that it would be possible to further reduce the angle between the resonator and the transport optical axes from 22.5° up to around 19°, to improve the loading of the atoms from the resonator to the transport beam, thanks to a larger overlapping of the two beams.

the stability of the cavity itself. A calculation of the effective number of atoms that can be trapped in the resonator, for different values of the waist and different laser powers is shown in Fig.3.7.

For this calculation, the following parameters have been assumed:

- Number of atoms at the end of the MOT operation: 1.65×10^{10}, with a peak atomic density of 8.1×10^{10} atoms/cm^3 (measured in ref.[84]). From the previous values, a MOT radius of around 2.5 mm can be estimated.
- Temperature of the atoms in the MOT: 25 μK [84].
- Finesse of the cavity: 1000.
- Wavelength of the laser beam coupled to the cavity: 1064 nm (red-detuned

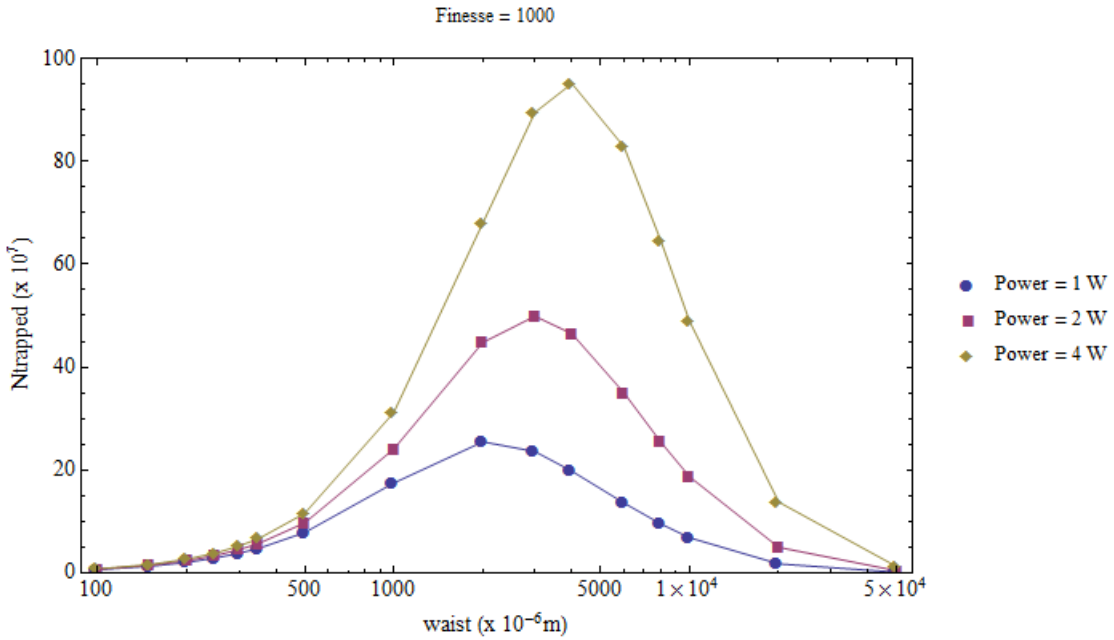

Figure 3.7: Number of atoms loaded into the resonator for different resonator waists and laser powers. For each laser power, an optimal waist exists, close to the value of the MOT radius.

far-off resonant trap).

As expected, the optimal waist of the resonator lies between 2 and 4 mm (for an increasing laser power from 1 W to 4 W, respectively), that is, it matches the expected MOT radius. However, it can be demonstrated that a waist of the resonator ≥ 1 mm makes the cavity unstable. The maximum waist that guarantees the stability of the cavity turns out to be around 400 μm. This gives a radius of curvature of the cavity mirrors of around 1.6 m for a cavity 90 mm long. The stability of the cavity is obtained at the expense of a reduced trappable number of atoms: only a few percent of the atoms in the MOT can effectively be trapped in the resonator. However, even if the loading efficiency is very low, one can take advantage of the unusual high number of atoms achievable in a potassium MOT (much higher than the usual MOT atom number in experiments with different atomic species, even other alkali-metal elements), and still have around 5×10^7 atoms in the resonator, if 1 W of laser power is used, and around 10^8 atoms if the power is increased to 4 W. This value is comparable to the one obtained in the

Ytterbium experiment, where the trapping efficiency is much higher (around 33%) [91].

Finally, with the chosen parameters for the cavity and a laser power of 1 W, a trap depth of around 300 μK (12 times the temperature of the atoms in the MOT) can be achieved, allowing to eventually start the evaporative cooling already in the resonator.

3.4 Optical transport with focus tunable lenses

After the atoms have been confined in the optical resonator, the size of the atomic cloud is expected to be reduced from $\sim$ 2 mm (MOT size) to $\sim$ 400 μm, thus facilitating the loading into the transport beam. The idea is to load the atoms from the resonator beam to a tightly focused optical dipole trap and then realize an optical transport by spatially displacing the focus of this trap over a distance of 290 mm, from the center of the 3D-MOT chamber to the center of the final glass cell, where the BEC will be realized.

The optical transport of an ultracold atomic sample can be performed in several ways, for instance by physically moving a lens with an highly precise translational stage (see ref.[92]), or by using lenses with tunable focal length [88]. Here we decide to adopt this latter strategy, using special lenses with variable focal length, from the supplier *Optotune* [93]. These lenses have a body filled with a low-optical absorption liquid and the surface is sealed off with an elastic polymer membrane. An external current applied to a magnetic ring placed on the rear of the lens, can induce the ring to mechanically press liquid from the outer area of the lens to its center, thus increasing the curvature of the membrane, and therefore also the focal length of the lens.

In a recent experiment by the group of T. Esslinger in Zurich [88], a setup with two focus tunable lenses has been implemented to transfer an ultracold sample of $\sim 10^6$ ^{87}Rb atoms at a temperature of 5 μK over a distance of 280 mm from a first vacuum chamber to their science chamber. Using a far-off resonant trapping beam at 1064 nm, with a power of 3.5 W and a waist of 47 μm kept constant during the transport, they have been able to transport the atoms over the whole distance in about 3 s, with an increase in temperature of the sample of few μK and almost no

atom losses.

The idea here is to reproduce the setup used in Zurich. However, it is worth noticing that one possible limitation to the efficiency of the optical transport in the Florence experiment is related to the loading of the atoms from the optical resonator to the transport beam. First, the beam in the resonator has a waist of 400 μm, while the transport beam should have a much smaller waist of around 50 μm. This difference in the beam waists limits the loading efficiency of the atoms from one trap to the other. Second, the two trap beams form an angle of 22.5°, limited by the geometry of the 3D-MOT chamber, and therefore the effective overlapping volume between the transport beam and the resonator must be reduced by a factor $\cos(22.5°) \approx 0.92$ (eventually, a minimum angle of 19° between the two beams can be reached, if the resonator beam is sent into the chamber at a certain angle with respect to the axis of the entrance and exit viewports, see Fig. 3.6).

During the time I spent at the Institute for Experimental Physics of the University of Innsbruck, I had the opportunity to carry out a preliminary test (not with atoms) of an optical transport with focus tunable lenses, in a slightly different setup, with respect to the one planned for the experiment in Florence. This preliminary test is presented in the next section.

3.4.1 Test of the optical transport

The setup for the optical transport with focus tunable lenses that I have built and preliminarly tested is meant to be implemented in a new experiment under construction. In this experiment, a mixture of two strongly magnetic atomic species, erbium and dysprosium, will be created. Here, the ultracold atomic sample has to be transferred from the main chamber of the experiment, where the two-species MOT will be operated, either forward to a glass cell devoted to high-resolution imaging, or backward to a second chamber where Rydberg spectroscopy will be performed. Since the transport setup is not specific to the used atomic species, the knowledge gained in this project can be easily adapted to the necessity of the potassium experiment in Florence .

The goals of the optical transport in the experiment in Innsbruck are the following:

- Waist of the optical dipole trap of about 30 to 40 μm, constant during the transport;
- Full transport distance to be covered: $\approx$ 320 mm backward (towards the "Rydberg" chamber) and $\approx$ 380 mm forward (towards the glass cell) starting from the center of the main vacuum chamber;
- Transport duration: 1 to 2 s.

The type of focus tunable lenses used in the test setup is the *Optotune* EL-10-30-Ci-NIR-LD [93]. These are plano-convex lenses with a view diameter of 11 mm, a focal length tuning range between 100 and 200 mm (which corresponds to a focal power tuning range between +10 and +4 diopters) and a broad-band cover glass anti-reflection coating between 700 and 1100 nm, suitable for the laser wavelength of the transport beam of 1064 nm. The lenses can be controlled by using the Lens Driver 4i [95] and the software supplied by *Optotune*.

Design of the optical setup The optical setup has been designed using the *Zemax Optic Studio* software [94] and is sketched in Fig. 3.8.

It is made up of two EL-10-30-Ci-NIR-LD focus tunable lenses (indicated by "FTL1" and "FTL2" in Fig.3.8), one "offset" lens and one "converging" lens. The offset lens is a 1 inch plano-concave spherical lens, with focal length f = - 150 mm. In combination with FTL2, it allows to reach an effective focal tuning range between -600 mm and 300 mm. The converging lens is a 2 inch plano-convex lens with a focal length of 500 mm, which is used to focus the beam. With this setup, using an initial collimated beam radius of 0.9 mm, the expected beam waist is $\approx$ 36 μm (diffraction limited), which is within the desired values. A bigger initial beam radius would allow to reach a smaller waist, but the size of the initial collimated beam is limited by the 11 mm view diameter of the FTL2. Thus, 0.9 mm turns out to be the maximum radius for the initial beam such that the beam is not cut by the FTL2 aperture. Moreover, by properly varying the current in the FTL2, the designed setup is expected to allow the displacing of the focus of the trap over

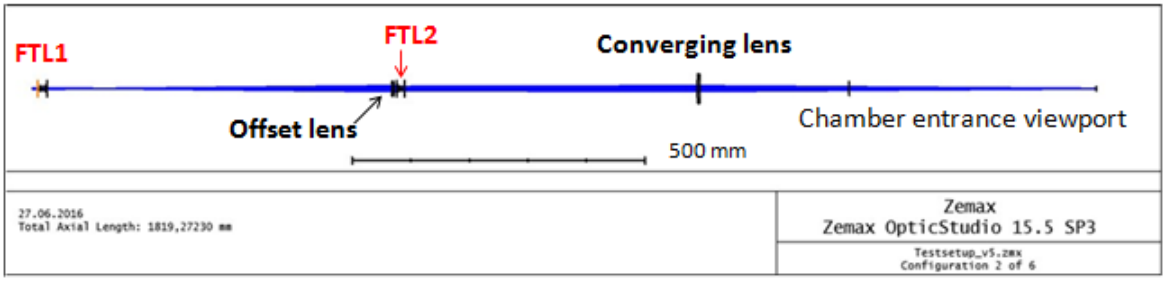

Figure 3.8: Setup for the optical transport at costant waist. The distance between FTL1 and the offset lens is 590 mm; the offset lens and the FTL2 are 15 mm apart; the converging lens is 500 mm far from the FTL2. The position of the viewport from which the transport beam enters the vacuum chamber is also indicated. In the sketched configuration, the focal length of FTL1 and FTL2 are 100 mm and 138 mm, respectively. With this value the focus of the trap beam is at the center of the main chamber (see Table 3.1 below), that is the starting position for the transport.

the full transport distance (-320 mm and 380 mm), maintaining the waist constant during the transport.

For the transport process, only the focal length of the FTL2 is varied, while FTL1 is kept always at the same focal length of 100 mm. This would suggest that FTL1 could be replaced by a simple fixed focal length lens. However, it is convenient to have two tunable lenses in the setup, since a proper tuning of the focal length of the two lenses allows to dynamically change the waist size of the optical dipole trap during the transport. This opens the possibility to have a dynamic control over the trapping potential (trap curvature and depth) without affecting its position or varying the beam power (see reference [88]).

Test of the optical setup The setup simulated with Zemax has been reproduced in the lab (Fig. 3.9). The test has included the following measurements:

- **Measurement of the beam waist.** A beam waist of $(50{,}0 \pm 6{,}5)$ μm has been measured using the *Thorlabs* beam profiler software. The CCD sensor has a resolution (pixel-size) of 6.5 μm. The measured value of the waist is slightly larger than the expected one of ≈ 36 μm, most probably because of aberration effects that are not accounted for in the calculation.

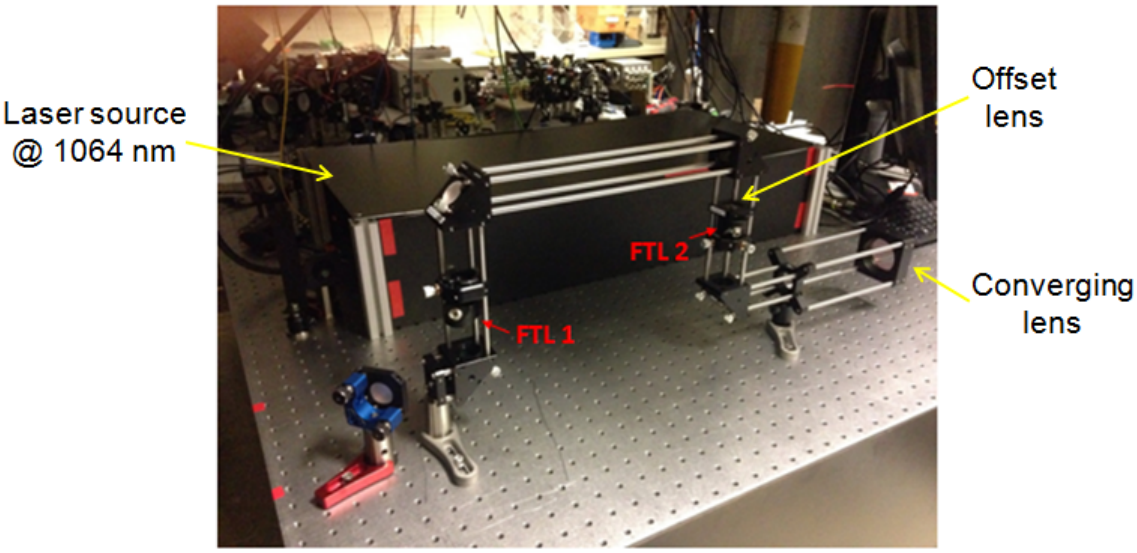

Figure 3.9: Picture of the optical setup for the transport at constant waist. Realization in the lab of the design of Fig.3.8. The laser source used for the test is a commercially available laser emitting at a wavelength of 1064 nm.

- **Temperature effects.** When increasing the current, the lens heats up, the optical fluid expands in volume and therefore the focal length of the lens decreases. A decreasing of the focal distance by approximately 0.6 diopters ($\approx$ 12 mm) per 10°C temperature increase has been observed (from datasheet, see [93]). This effect crucially affects the reproducibility of the optical transport, and needs to be carefully characterized and compensated for. In the case of the EL-10-30-Ci-NIR-LD lens type the temperature compensation can be achieved thanks to an integrated temperature sensor (SE97B) which allows for active feedback on the focal length variation. The temperature compensation mechanism works as follows. At each given value of the applied current corresponds a certain value of the lens focal power (the focal power depends linearly on the applied current, as reported in [95]), and a certain value of the temperature. These calibration data are stored in the EEPROM of the lens and allow for the reproducibility of the focal power. In practice, when a certain value of the focal power is set, if the sensor measures a temperature which is different from the one stored in the lens memory for that particular focal power, the current is adjusted such that to provide the

desired set focal power.
When this compensation mechanism is activated, the measured reproducibility of the lens focal power is 0.1 diopters, which corresponds to a reproducibility of the focal length within 3 mm. A shift of the trapping beam focus of 3 mm at each experimental cycle is considerable for the purpose of the optical transport, but it is sistematic: at an increase in temperature corresponds a positive shift of the focal power (up to + 0.1 diopters), while a decrease in temperature causes a negative shift of the focal power, up to -0.1 diopters. This effect can therefore be properly compensated for in the experiment.

- **Achievable transport distance and duration.** The range of focal powers that can be maintained at a given temperature depends on the minimum and maximum limits on the operational temperatures and currents of the lens, which can be set by the user. In the test these values have been set as follows: $T_{min} = 20$ °C, $T_{max} = 45$ °C, $I_{min} = 0$ mA, $I_{max} = 290$ mA (recommended maximum operational current [95]). For these limit values, the range of guaranteed maintained focal powers goes from 4.0 to 10.5 diopters. Table 3.1 summarizes the values of the focal power of FTL1 (fixed) and FTL2 and the corresponding focal lengths, that are needed to have the focus of the transport beam in the three desired positions: the center of the main chamber (indicated with position A in the table), the center of the glass cell (position B) and the center of the Rydberg chamber (position C). All the values of focal power are within the guaranteed range for temperature compensation operation. This means that the temperature compensation mechanism is guaranteed over the whole transport distance. Concerning the duration of the transport, the test has proved that it is possible to move the focus of the beam over a distance of up to 380 mm in 1 s. In fact, the response time of the lens to a current change of 200 mA is only about 15 ms [93].

It is worth noticing that the performed test of the optical transport setup is only preliminary, for two main reasons. First, it has been done at a very low laser power of 10 mW, while the actual transport is meant to be performed at

	Focus at position A	Focus at position B	Focus at position C
Focal power FTL1	10.0 dpt (f = 100 mm)	10.0 dpt (f = 100 mm)	10.0 dpt (f = 100 mm)
Focal power FTL2	7.21 dpt (f ≈ 138 mm)	8.41 dpt (f ≈ 118 mm)	5.85 dpt (f ≈ 170 mm)

Table 3.1: Values of the focal powers of FTL1 and FTL2 needed for the optical transport at constant waist. At each configuration of focal powers corresponds a different position of the transport beam focus: focus at the center of the main chamber (A), focus at the center of the glass cell (B), focus at the center of the Rydberg chamber (C).

higher power (at least few Watts). At higher powers there might be some effect of heating of the lens due to absorption of laser light that are independent from the applied current, and cannot be easily compensated for. Second, the setup has to be implemented in the experiment, and a comprehensive test of the optical transport (as the one described in [88]) has to be performed with the atoms. However, this first test is necessary to understand the working principle of the lenses and check the efficiency and stability of this technique to displace the focus of an otical trap.

Chapter 4

Exploring dipolar Bose-Einstein condensates with tunable interactions: observation of roton mode population

This chapter focuses on the work I carried out in the ERBIUM experiment at the Institute for Experimental Physics of the Univeristy of Innsbruck (Austria). There, I have been working with dipolar BECs of Er atoms, for which the anisotropic and long-range dipole-dipole interaction add to the contact interaction, opening the access to many intriguing new phenomena that can be studied with these systems. Among them, an interesting phenomenon, theoretically predicted in 2003 [35], is the emergence of a roton-maxon excitation spectrum in a dipolar BEC, reminescent of that in superfluid helium. Before our investigation, it had never been observed in experiments. Here, I will report on the first experimental observation of the roton mode population in a dipolar BEC of ^{166}Er atoms.

I will first give an historical introduction to the roton excitation, originally observed in superfluid helium, and describe how superfluidity and Bose-Einstein condensation are linked. Then, I will give a theoretical description of the elementary excitations in a trapped dilute BEC, showing that in conventional (non-dipolar) BECs a roton excitation is not present. On the contrary, in dipolar BECs the

roton emerges as a consequence of the peculiar long-range and anisotropic character of the DDI. The above mentioned theoretical proposal, at the basis of our experimental investigation, is reviewed in this chapter.

I will then describe the ERBIUM experiment in Innsbruck, giving the details of the production of degenerate gases of ^{166}Er in this system. The experimental study of the roton mode excitation in the dipolar BEC is then reported. Here, we have exploited the tuning of the s-wave scattering length using a Feshbach resonance. This has been an essential tool to reach the regime where DDI dominate over the contact interactions, where the roton mode is expected to emerge. I will describe the measurements, and present the results. I will show the comparison of our experimental data to both analytical model and numerical simulations, which confirm the population of the roton mode in our system. Finally, I will present numerical simulations that I personally performed, which helped in having a better understanding of the physics at play when the roton mode in the dipolar BEC is populated. The results of these simulations also rised up interesting interpretations which might connect the roton physics to the physics of the quantum droplets [32, 26] in a dipolar quantum gas. This connection will be discussed at the end of the chapter.

4.1 Historical introduction to roton excitations: rotons in superfluid helium

Helium (He) was first liquefied in 1908 by H. Kamerlingh Onnes, who cooled it below the liquid-gas transition temperature of 4.2 K. One special property of helium is that, below a certain pressure, it remains liquid for arbitrarily low temperatures, even down to the absolute zero. On the contrary, all other elements of the periodic table solidify below a certain temperature, when they are cooled down. Indeed, at very low temperatures the kinetic energy of the atoms is only given by the zero-point motion, which is inversely proportional to the atomic mass. For helium, the atomic mass is so small that the zero-point motion is sufficiently high to win over the interatomic attractive van der Waals forces, thus preventing the atoms from forming a crystal and keeping the system fluid even at absolute

zero. Only under strong pressure (> 25 atm) does helium solidify. For almost all the other elements, the atomic mass is so much higher than the one of helium, that the zero-point motion is not sufficient to oppose the crystalizing effect of the attractive forces. The only exception is hydrogen, whose atoms are lighter than the helium ones. However, even if they are lighter, the interatomic interactions are much stronger than in helium, and hydrogen too solidifies at sufficiently low temperature.

In 1927 M. Wolfke and W.H.Keesom discovered that in the bosonic ^{4}He isotope there exists a distinct phase transition at a temperature of around 2.17 K, lower than the liquid-gas transition temperature. This phase transition has been observed in a discontinuity of the specific heat, whose curve as a function of temperature has the shape of the Greek letter λ, and thus the transition temperature was called λ point, $T_\lambda = 2.17$ K. The two phases of liquid ^{4}He were named "helium I" ($T > T_\lambda$), and "helium II" ($T < T_\lambda$). Later, in 1938, P. Kapitza [96] and independently, J.F. Allen and A.D.Misener [97] performed experiments on liquid helium II revealing its extremely low viscosity. Indeed, the flow in liquid helium II below the λ point was observed to be strikingly non-dissipative. This behaviour inspired Kapitza to coin the term *superfluid* for helium II, in connection to the phenomenon of electronic superconductivity in metals. Superconductivity is the property of electrons to flow without resistance through a metal if it is cooled down below a certain critical temperature. It had already been observed earlier, in 1911 [98] (even if not yet microscopically understood at that time).

One of the most fruitful ideas in interpreting the behaviour of helium II is the so-called two-fluid model, developed by L. Tisza [99] and L. Landau [100] shortly after the intuition by Kapitza. In this model the system is formally divided into two fluids: the *superfluid* and the *normal fluid*. At zero temperature there is only a superfluid, that is a perfect ideal fluid which may flow without friction. If heated, the heat energy excites the liquid. The excitations created within the liquid can propagate from one place to another, collide with the walls and with each other, and give to helium II some properties associated with the normal fluid component, such as a finite viscosity. Thus, the viscous normal fluid component supports thermal excitations in the system. If the temperature is increased, the normal fluid becomes more and more dominant until the superfluid completely vanishes at and

above the critical λ point.

4.1.1 Landau's dispersion relation and superfluid critical velocity

In 1941 Landau, as a result of his studies of quantum hydrodynamics, supposed that every weakly excited state in liquid helium II was the combination of two kinds of low-lying elementary excitations or *quasiparticles* [100]. On the one hand, there are the phonons, or quantized sound waves, that are low momentum excitations whose energy ϵ is a linear function of their momenum k: $\epsilon(k) = \hbar kc$, where c is the sound velocity. On the other hand, there are the *rotons*, elementary excitations at finite momenta with an energy forming a parabola of minimum Δ, the roton energy gap. These latter were initially interpreted as quantized vortices: this explains the name rotons, due to the rotational nature of such vortices. The energy of the roton excitations is a quadratic function of their momentum k_{rot}:

$$\epsilon(k) = \Delta + \frac{\hbar^2(k - k_{rot})^2}{2m_{rot}}, \tag{4.1}$$

where m_{rot} is the effective mass of a roton. Few years later, Landau finally unified the two types of excitation in a single dispersion relation $\epsilon(k)$, which continuously evolves from linear at low k (phonons), up to a maximum, denoted as *maxon*, to parabolic-shaped with a minimum (roton) at a finite $k = k_{rot}$, and finally it rises again, as represented in Fig.4.1. At the low temperatures encountered in helium II, only the states near $k = 0$ and those close to the roton minimum are excited.

Originally, Landau proposed his phonon-roton dispersion relation to explain the observed thermodinamic properties of ^{4}He around the λ point. Later, in 1954, R. Feynmann linked Landau's energy spectrum to the static structure factor of the liquid, through the following relation [101]:

$$\epsilon(k) \leq \frac{\hbar^2 k^2}{2mS(k)}, \tag{4.2}$$

where $S(k)$ is the static structure factor, defined as $S(k) \equiv \langle 0|\hat{\rho}_k \hat{\rho}_k^\dagger|0\rangle/N$. Here

N is the number of atoms of mass m, $|0\rangle$ is the ground state of the system, and $\hat{\rho}_k \equiv \sum_q \hat{a}_q^\dagger \hat{a}_{q+k}$ is the density fluctuation operator, with $\hat{a}_q^\dagger$ the bosonic creation operator of a particle of momentum q. $S(k)$ is the Fourier transform of the two-body correlation function and hence provides a measure of the degree of correlation between the atoms. The existence of strong two-body correlations in helium II may, at first glance, seem surprising since helium remains a liquid even at temperatures close to the absolute zero exactly because of weak interatomic interactions. However, despite their apparent weakness, these interactions are strong if associated to the density of the liquid state. Indeed, typical densities in helium II are $n \sim 10^{21}$ - 10^{23} cm^{-3} (for comparison, the density of a gaseous BEC is $\sim 10^{14}$ cm^{-3}), which is such that the average interatomic separation d is close to the distance b corresponding to the minimum of the attractive interatomic van der Walls potential well: $d \sim b \simeq 3 \times 10^{-10}$ m [101]. Thus, for helium II the diluteness parameter $nb^3 \sim 1$, and the system is said to be *dense*, in opposition to dilute as in the case of BECs, for which typically $n|a|^3 \ll 1$.

Feynmann identified the peculiar roton minimum in the energy spectrum of helium II with a peak of the static structure factor occurring at $k_{rot} \simeq 2\pi/d$. This manifests a tendency of the system to establish a local order on the length scale of the interparticle distance, driven by the strong correlations among the atoms. In 1957, M. Cohen and Feynmann proposed that Landau's dispersion could be measured by inelastic scattering of neutrons off of a liquid ^{4}He sample [102]. This experiment was carried out soon after, and confirmed Landau's theory [103] (see Fig.4.1).

Based on his intuition of the phonon-roton dispersion relation, Landau developed a very general argument that results in a hard criterion for these elementary excitations to allow for superfluidity in helium II. The criterion states that superfluid, or dissipationless flow only exists below a critical velocity, the so-called superfluid critical velocity or Landau critical velocity. Let us consider a superfluid flow moving at velocity $\mathbf{v}_s$ and a small aperture or a small defect at rest in it. The flow can lose kinetic energy (dissipation) by creating elementary excitations. The energy cost of an excitation of momentum k is $\epsilon(k)$ in the frame of the superfluid. In the laboratory frame, it is instead equal to $\epsilon(k) + \hbar\mathbf{k} \cdot \mathbf{v}_s$. For a given k, the energy cost is minimum for an excitation propagating against the superfluid flow:

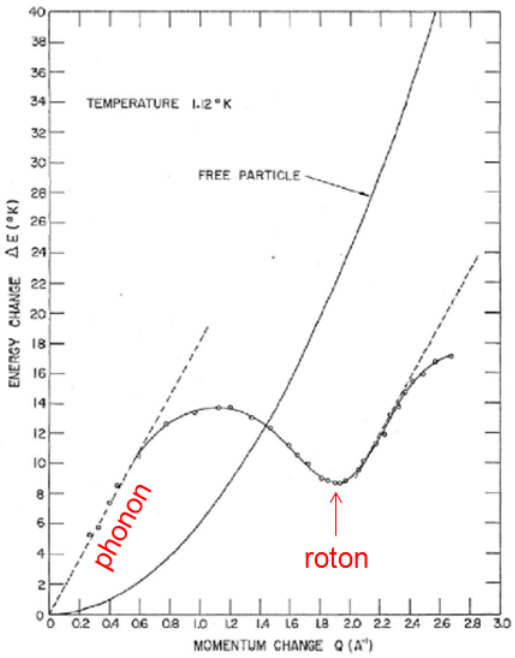

Figure 4.1: Measured phonon-roton dispersion relation of liquid ^{4}He at a temperature of 1.12 K. The circles are neutron scattering data from ref. [103]. The solid line shows the calculated free-particle dispersion curve. The dashed line from the origin is the theoretical phonon branch calculated from a velocity of sound of 237 m/s, and the dotted line has a slope equal to the velocity of sound. The smooth curve through the points is a guide to the eyes. The measured dispersion relation shows a linear phononic behaviour at small momenta, and the roton minimum at a momentum ≈ 2.0 Å^{-1}, which is on the order of the inverse of the interparticle distance. Figure adapted from [103].

$\epsilon(k) - \hbar k v_s$. The fluid loses energy through dissipation if $\epsilon(k) - \hbar k v_s < 0$. Consequently, the minimum velocity giving rise to dissipation is the Landau critical velocity, given by:

$$v_L = \min_k \frac{\epsilon(k)}{\hbar k}, \tag{4.3}$$

where the minimum is on the full k-spectrum.

This simple argument by Landau, based on the conservation of energy and momentum, is of fundamental importance for the understanding of superfluidity. A direct consequence is that systems where $\min_k \frac{\epsilon(k)}{\hbar k} = 0$ can not be superfluid,

since then $v_L = 0$ and an arbitrarly small velocity would result in dissipation. For helium II, the superfluid critical velocity is set by the roton minimum, and it has been measured to be $v_L \simeq \Delta/k_{rot} \approx 60$ m/s [104].

4.1.2 Superfluidity and Bose-Einstein condensation

Inspired by the variety of experimental evidences for the superfluid behavior of ^{4}He below T_λ, by the fact that such phenomena were not observed in the fermionic ^{3}He isotope at the same temperatures, and by the earlier theoretical work of Einstein on the Bose-Einstein condensation of an ideal Bose gas, in 1938, F. London proposed that the unusual behavior of liquid ^{4}He was due to the phenomenon of Bose-Einstein condensation taking place in the cold fluid below the λ point [105]. London was the first to link the superfluidity of helium II to the Bose-Einstein condensation, and he did it at a time when only the non-interacting theory of BECs had been developed. Successively, in 1947, Bogoliubov constructed his theory of a weakly interacting BEC (see section 2.5), and in 1956 L. Onsager and R. Penrose generalized Bogoliubov theory of a BEC making it applicable to a system of strongly interacting particles. In their paper [106], Onsager and Penrose derived a criterion for superfluidity and Bose-Einstein condensation that linked definitively the two phenomena. The criterion, which is applicable to either a liquid or a gas, states that Bose-Einstein condensation is equivalent to the existence of a macroscopic eigenvalue of the one-body correlation function, where macroscopic means scaling as the total number of particles, N. The authors demonstrated that helium II indeed satisfies this criterion, with roughly less than 10% of the atoms "condensed" at zero temperature, thus confirming the original idea of London.

Today, much of the physics of superfluid ^{4}He remains elusive, due primarily to its very high density and strong interactions. Because of strong interactions, in superfluid helium usually only a very small number of atoms are in the condensate, at most 10% of the total number of atoms even at zero temperature, compared to the typical percentage of atoms in the condensate for dilute BECs, of more than 80%. Atoms that are kicked out of the condensate at zero temperature because of the interactions form the so-called *quantum depletion* of the condensate. The large quantum depletion in helium II makes it very hard to investigate also theo-

retically, since the mean-field perturbative approach which can be used with BECs (see section 2.5) can not be applied here, and more complex theories have to be developed (see, for instance, the discussion in ref. [107]).

Gaseous BECs, constituting "the other" quantum fluid than superfluid helium, bring a complementary high degree of control and tunability of the system parameters, togheter with an easier theoretical description, allowing to further investigate superfluidity in cold matter.

4.2 Elementary excitations in trapped Bose-Einstein condensates

In the previous section we have seen that superfluid ^{4}He and gaseous BECs are manifestations of the same physical phenomenon. Now, a question may arise whether a BEC also shares the same low-energy excitation spectrum as helium II, characterized by the phonon-roton dispersion relation. This is an interasting question, because we have seen that this dispersion relation has a fundamental impact on the macroscopic properties of the superfluid. In addition, excitations determine the dynamic behaviour of the system in the regime of weak perturbations and, therefore, they provide experimental access to important information about the system. The goal of this section is to give an answer to this question. First I will give a general theoretical description of the elementary excitations in a dilute BEC, following the treatment of ref. [78]. Then I will discuss two specific cases in which the emergence of a roton minimum in the low-energy spectrum of a trapped BEC is theoretically predicted. One of this two cases will be the subject of the experimental investigation presented later in this chapter.

The hamiltonian of a gaseous atomic assembly was introduced in Chapter 2.5 (see Eq. (2.37)). There, a mean-field treatment was introduced, and by using the zeroth order in the non-condensed field operator Ψ', a semi-classical equation for the BEC state Φ_0 was obtained (Eq. 2.40), the so-called GPE.

The description of the elementary excitations of a dilute BEC is usually performed on the basis of the so-called Bogoliubov-de Gennes (BdG) equations [79],

which are obtained by diagonalizing the quadratic hamiltonian (2.37) using the celebrated Bogoliubov transformation of the particle annhilation and creation operators into quasiparticle ones [108]. These equations can be alternatively obtained by developing to second order in Ψ' the equations of section 2.5.1, that is performing a perturbative treatment on the GPE, linearizing it around the stationary solution Φ_0. In other words, one can look for solutions of Eq.(2.40) of the form:

$$\Phi_0(\mathbf{r},t) = e^{-i\mu t/\hbar}[\phi(\mathbf{r}) + u(\mathbf{r})e^{-i\omega t} + v^*(\mathbf{r})e^{i\omega t}], \tag{4.4}$$

where $u(\mathbf{r})$ and $v(\mathbf{r})$ are complex amplitudes of small oscillations around the ground state wavefunction, with frequency ω. By substituting (4.4) into Eq.(2.40), and keeping only terms linear in the functions $u(\mathbf{r})$ and $v(\mathbf{r})$, one obtains a set of coupled linear equations, which are exactly the BdG equations:

$$\begin{pmatrix} H_0 + \mathcal{A} + \mathcal{B} & -\mathcal{B} \\ \mathcal{B} & -(H_0 + \mathcal{A} + \mathcal{B}) \end{pmatrix} \begin{pmatrix} u(\mathbf{r}) \\ v(\mathbf{r}) \end{pmatrix} = \epsilon \begin{pmatrix} u(\mathbf{r}) \\ v(\mathbf{r}) \end{pmatrix} \tag{4.5}$$

where $H_0 = -(\hbar^2/2m)\nabla^2 + V_{ext}(\mathbf{r})$, $\mathcal{A} = \int d\mathbf{r}' V_{eff}(\mathbf{r}-\mathbf{r}')n(\mathbf{r}')$, and the operator $\mathcal{B}$ acting on a function ψ, and evaluated at point $\mathbf{r}$ is defined as:

$$(\mathcal{B}\psi)(\mathbf{r}) = \int d\mathbf{r}' \phi(\mathbf{r}') V_{eff}(\mathbf{r}-\mathbf{r}')\psi(\mathbf{r}')\phi(\mathbf{r}). \tag{4.6}$$

The coupled equations (4.5) allow one to calculate the eigenenergies $\epsilon_j = \hbar\omega_j$ of the excitations, and the corresponding eigenfunctions $(u_j(\mathbf{r}), v_j(\mathbf{r}))$, from which one can extract the wavefunction of the elementary excitation using Eq.(4.4).

In a uniform gas, i.e. $V_{ext} = 0$, the amplitudes u and v are plane waves. In addition, if the inteparticle interactions are simple contact interactions, $V_{eff}(\mathbf{r}) = g\delta(\mathbf{r})$, one gets the following Bogoliubov dispersion relation [79]:

$$\epsilon = \hbar\omega = \sqrt{\frac{\hbar^2 k^2}{2m}\left[\frac{\hbar^2 k^2}{2m} + 2gn\right]}, \tag{4.7}$$

where $\mathbf{k}$ is the wave vector of the excitation and $n = |\phi|^2$ is the density of the gas. At low momenta, Eq.(4.7) gives the phonon dispersion relation $\epsilon(k) = \hbar c_s k$,

where

$$c_s = \sqrt{\frac{gn}{m}} \tag{4.8}$$

is the sound velocity. Instead, at large momenta, the energy spectrum coincides with the free-particle energy $\epsilon(k) = \hbar^2 k^2/2m$. The transition between the collective and the single-particle behaviour occurs at momenta of the order of $\hbar/\xi$, where ξ is the healing length introduced in section 2.5.1 [109].

In the presence of a trapping potential the spectrum gets discretized [78].

Eq.(4.7) shows a monotonic behaviour, and thus no roton excitation is present in weakly-interacting BECs with only contact interactions. This has been also verified experimentally. As an example, J. Steinhauer and coworkers at the Weizmann Institute of Science in Israel have measured the bulk excitation spectrum of a ^{87}Rb BEC and they found excellent agreement with Bogoliubov theory (4.7), (see ref. [110]). The absence of a roton minimum in their measured energy spectrum can be understood by recalling the qualitative discussion about the relation (4.2) from Feynmann between the energy spectrum and the static stracture factor in helium II. The interactions in ^{87}Rb are repulsive and characterized by an s-wave scattering length $a \approx 5$ nm. This is between 1 and 2 orders of magnitude smaller than the average atomic distance at typical densities.

4.2.1 Emergence of the roton

In 2003 two seminal theoretical works predicted the existence of a roton minimum in the energy spectrum both in BECs with dipole-dipole interactions [35], and in BECs irradiated by a off-resonant laser light [111]. The former proposal is the seed argument for the experimental work described later in this chapter, and will be discussed extensively in the next section.

In the latter proposal, one exploits a far off-resonant laser shined on a gaseous BEC inducing dipole-dipole interactions between the atoms. The dynamically induced DDIs give rise to long-range interatomic correlations whose characteristic length is the laser wavelength. These correlations, which are tunable via the laser intensity and frequency, can produce a minimum at finite momentum in the excitation spectrum of the BEC, reminescent of the roton minimum in the strongly

correlated liquid helium II. Inspired by the idea of long-range interactions mediated by light, a roton-type mode softening has been recently observed in a BEC coupled to an optical cavity [112]. In that experiment, the strong coupling between the cavity light and the atomic system induces an effective global (infinite)-range atom-atom interaction which extends over the entire atomic cloud and is tunable in strength. The coupling arises from the coherent scattering of photons from a pump laser beam into the cavity mode and back to the pump. When the pump laser is switched on the excitation frequency decreases and shows a minimum as a function of the pump-laser power (not in momentum space). Because of the existence of a minimum in the frequency domain, this effect has been called “roton-type mode softening”.

Additionally, roton-like softening of the excitation spectrum can be created in BECs with spin-orbit coupling [113, 114], and in BECs in shaken optical lattices [115], using off-resonant laser light to engineer the single-particle dispersion relation. In the first case, the single-particle dispersion is modified to show a "double-well" structure by coupling different momentum classes of spin components in a BEC through the use of a pair of off-resonant Raman beams [116]. The degeneracy of the two wells can be further lifted by adjusting the Raman detuning of the beams. This can be interpreted as a roton-maxon-like feature of the dispersion relation. In the second case, a similar double-well structure in the single-particle dispersion is realized by loading a 3D BEC into a 1D shaken (i.e. periodically phase modulated) optical lattice [117]. If the BEC is loaded into one of the dispersion minima by providing a momentum kick, before phase modulating the lattice, the dispersion relation is again modified. In particular, the degeneracy between the two wells is lifted and the resulting dispersion relation features a roton-maxon like behaviour.

In all the above described examples, the wavelength of the roton-like excitation is externally set by the driving light field. One can therefore speak about "artificial rotons" [115] in contrast to the "genuine" roton arising in liquid helium II, which is driven by internal interatomic interactions. An alternative system where a roton minimum of the excitation spectrum is theoretically predicted, corresponding to the second proposal from 2003, is a BEC with dipole-dipole interactions [35]. Interestingly, BECs with dipolar interactions are more closely related to superfluid

helium with respect to BECs irradiated by off-resonant light, in what concerns the origin of the roton minimum, arising from the genuine interaction between the atoms. In particular, the roton excitation is compressible (i.e. its wavelength can be changed by changing the density of the system), as in the case of superfluid helium. However, in contrast to helium, the emergence of an energy minimum at finite momentum in dipolar BECs does not require strong inter-particle interactions. It instead arises in the weakly-interacting regime and originates from the peculiar anisotropic and long-range character of the DDI, as will be discussed in the next section.

4.2.2 Roton mode in dipolar Bose-Einstein condensates

In their seminal paper [35], L. Santos and co-workers theoretically predict the existence of a roton-maxon excitation spectrum for dipolar BECs in an anisotropic geometry. They point out that, as in superfluid helium, the roton spectrum in such systems is a genuine consequence of the underlying interactions among the particles.

They consider the case of a quasi-2D dipolar BEC, harmonically confined in the direction of the dipoles (z-axis) and uniform in the other two directions (see Fig.4.2). This trapping geometry is also later called "infinite pancake".

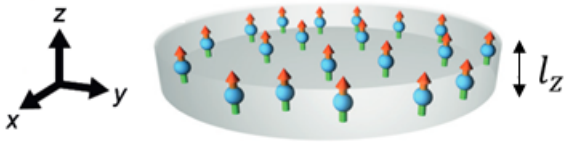

Figure 4.2: Quasi-2D pancake trap geometry considered in ref. [35]. The system is harmonically confined along the direction of orientation of the dipoles (z-axis) and is assumed to be uniform in x and y. The size of the cloud along z is given by the harmonic oscillator length $l_z = \sqrt{\hbar/m\omega_z}$, where ω_z is the trapping frequency. Figure adapted from [37].

The origin of a minimum of the excitation spectrum at finite momentum in such a system can be qualitatively understood from the following geometrical argument. Let us consider elementary excitations in the infinite (xy)-plane. They are characterized by their planar momentum of norm k and correspond to in-plane density

modulations of wavelength $2\pi/k$. The harmonic confinement along the dipoles fixes a characteristic length for the size of the BEC along that direction through the harmonic confinement along $l_z = \sqrt{\hbar/m\omega_z}$, where ω_z is the trapping frequency along z. For low k, the wavelength of the real-space density modulations is larger than l_z and the dipoles sit mainly side-by-side. Therefore the DDI are predominantly repulsive and the phononic part of the dispersion relation $\epsilon(k)$ is stiffened with respect to a non dipolar system. In contrast, for $kl_z \geq 1$, the wavelength of the real-space density modulations is on the order of l_z, and a head-to-tail alignment of the dipoles is favoured. In this configuration the DDI are mainly attractive, which results in a softening of the excitation spectrum. This softening for $k \geq 1/l_z$ is counterbalanced by the contributions of the repulsive contact interaction, and of the kinetic energy, which ultimately dominates at very large $k \gg 1/l_z$, leading the dispersion relation to eventually bend up into a single-particle spectrum. For strong enough DDI, the changing of sign of the dipole-dipole contribution to the excitation energy for increasing momentum, and the competition of the DDI with the contact interactions and the kinetic energy, give rise to a roton minimum in the dispersion relation $\epsilon(k)$, occurring at momentum $k = k_{rot}$, set by the geometrical scaling $k_{rot} \sim 1/l_z$ [35]. Fig.4.3 shows a drawing of the expected excitation spectrum in the above described trapping geometry. The sketches of the real-space density modulations help to visualize the qualitative description.

Quantitatively, for a condensate of dipolar particles harmonically confined in the z direction, along which the dipoles are aligned, and uniform in the other two directions, the ground state wave function is independent of the in-plane coordinates $\mathbf{r} = (x, y)$, and can be written as $\Phi_0(\mathbf{r}, t) = \phi(z)e^{-i\mu t/\hbar}$, where μ is the chemical potential. We recall that Φ_0 is dictated by the NLGPE given in Eq.(2.56). Then, integrating over $\mathbf{r}'$ in the dipole-dipole term U_{dd}, one obtains a one-dimensional equation similar to the stationary GPE (2.42) for short-range interactions:

$$\left(-\frac{\hbar^2\nabla^2}{2m} + \frac{m}{2}\omega_z^2 z^2 + (g + g_{dd})\phi^2(z)\right)\phi(z) = \mu\phi(z). \tag{4.9}$$

where $g_{dd} \equiv \mu_0\mu_m^2/3 = 4\pi\hbar^2 a_{dd}/m$ is a measure of the strength of the DDIs. The problem can be simplified by using the TF approximation for the condensate

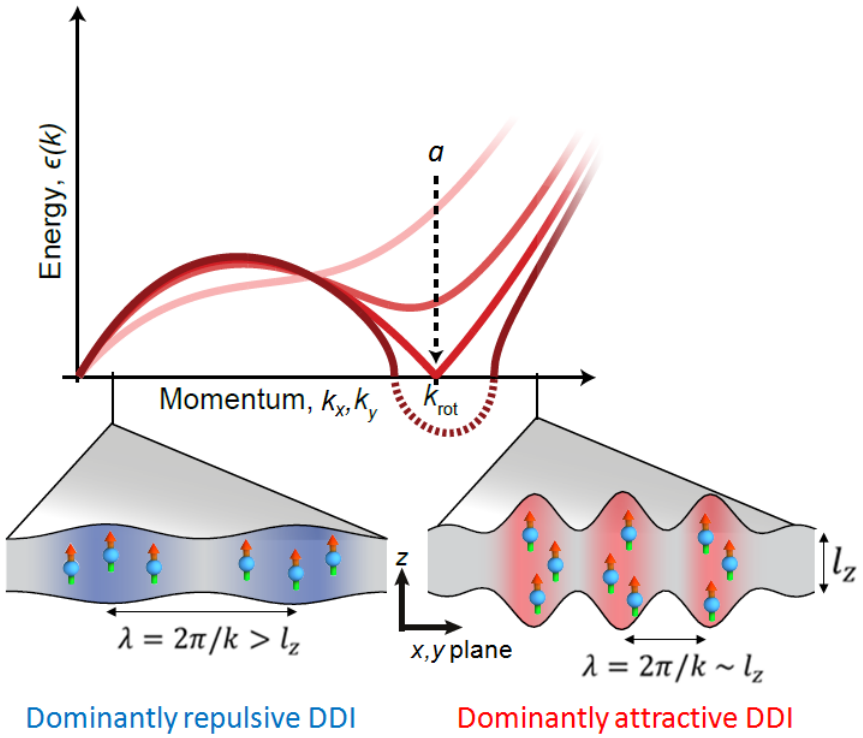

Figure 4.3: Roton mode in a dipolar BEC. Real (solid line) and imaginary (norm of the dotted line) parts of the dispersion relation for a dipolar BEC in the geometry of Fig.4.2, showing the emergence of the roton minimum for decreasing a (regime of dominant DDI). The DDI change sign from repulsive to attractive for increasing momentum. The sketches at the bottom of the figure show the dipole alignment corresponding to small-k (on the left) and large-k (on the right) density modulations. Figure adapted from [37].

wave function, which is valid for $\mu \gg \hbar\omega_z$, and reads:

$$\phi^2(z) = n_0(1 - \frac{z^2}{L^2}), \tag{4.10}$$

where $n_0 = \mu/(g+g_{dd})$ is the condensate maximum density and $L = (2\mu/m\omega_z^2)^{1/2}$ is the TF radius of the condensate in the z direction. As done for the purely-contact interacting case in section (4.2), one can obtain the spectrum of the elementary excitations in the Bogoliubov-de-Gennes approximation by linearizing Eq.(4.9) around the approximate ground state solution (4.10). For low in-plane momenta $kL \ll 1$, the BdG equations become identical to the ones for the exci-

tation of a trapped condensate with a short-range interaction characterized by a coupling constant $(g + g_{dd}) > 0$ (see section 4.2). In this case, the lowest branch represents phonons propagating in the (xy)-plane. The dispersion relation is given by:

$$\epsilon_0(k) = \hbar c_s k, \qquad kL \ll 1 \tag{4.11}$$

where the sound velocity is $c_s = \sqrt{2\mu/3m}$. This branch is not modified by the effect of the DDI. One finds that the most interesting behaviour of the excitation spectrum in the TF regime is expected in the opposite limit, $kL \gg 1$. Here the effective coupling strength decreases due to the negative contribution of the dipolar term, coming from mainly attractive DDI. One can demonstrate that in this case the BdG equations are similar to the ones for the excitation of a trapped condensate with a short-range interaction characterized by a coupling constant $2(g - g_{dd})$. The parameter ϵ_{dd} introduced in Eq.(2.35), can now be expressed as $\epsilon_{dd} = g_{dd}/g$. For the threshold value $\epsilon_{dd} = 1$, for which the effective coupling vanishes, the dispersion law is characterized by a plateau, and the lowest branch of the spectrum is given by [35]:

$$\epsilon_0^2(k) = E_k^2 + \hbar^2\omega_z^2, \qquad kL \gg 1, \tag{4.12}$$

where $E_k = \hbar^2 k^2/2m$. Instead, for $\epsilon_{dd} \neq 1$, assuming $\mu E_k|1/\epsilon_{dd} - 1|/(1 + 1/2\epsilon_{dd}) \ll \hbar^2\omega_z^2$, the lowest branch of the spectrum is found to be:

$$\epsilon_0^2(k) = E_k^2 + \frac{(1/\epsilon_{dd} - 1)(5 + 1/\epsilon_{dd})}{3(1 + 1/2\epsilon_{dd})(2 + 1/2\epsilon_{dd})}\mu E_k + \hbar^2\omega_z^2, \qquad kL \gg 1, \beta \neq 1/2. \tag{4.13}$$

For $\epsilon_{dd} > 1$, that is when DDI dominate over the short-range interactions, the dispersion law (4.13) has a minimum, and the whole spectrum should have a roton-maxon character (see Fig.4.3).

From Eq.(4.13), one can evaluate the momentum at which the roton minimum is located (the "roton momentum"), and the excitation energy at the roton minimum (typically indicated as the "roton energy gap"). For ϵ_{dd} close to 1, the roton momentum k_{rot} is given by:

$$k_{rot} = \left(\frac{16\mu(1 - 1/\epsilon_{dd})}{30\hbar\omega_z} \right)^{1/2} \frac{1}{l_z}, \tag{4.14}$$

while the roton energy gap $\Delta \equiv \epsilon_0(k_{rot})$ reads:

$$\Delta = \left[\hbar^2\omega_z^2 - \left(\frac{8\mu(1 - 1/\epsilon_{dd})}{30} \right)^2 \right]^{1/2}. \tag{4.15}$$

Eq.(4.15) shows that the roton minimum can be made deeper, or in other words, the roton gap can be decreased by increasing the density (chemical potential) or ϵ_{dd}. In particular, increasing ϵ_{dd} means decreasing the s-wave scattering length a (see Fig.4.3). For $\mu(1 - 1/\epsilon_{dd})/\hbar\omega_z = 30/8$ the minimum energy reaches zero at $k_{rot} = \sqrt{2}/l_z$. At larger values of μ or ϵ_{dd} one gets imaginary excitation energies for $k \sim 1/l_z$, which correspond to an unstable condensate [69]. This analytical result is confirmed by numerical calculation [35] and by several other theoretical works developing theoretical calculations in more sophisticated configurations (see, for instance, [118, 119, 120, 121, 122, 123]).

The roton in dipolar BECs is highly tunable, as we have seen that, by varying the density, the frequency of the tight confinement, and the s-wave scattering length, one can vary the depth of the roton minimum in the dispersion relation.

Despite the physics of the roton mode in dipolar BECs is theoretically deeply understood, the experimental observation of dipolar roton modes has remained elusive so far. This may be due to the fact that, up to few years ago, the only dipolar BEC available in experiments consisted of chromium atoms [18], for which the achievable dipolar interaction strength is not sufficient to dominate over the short-range interaction and support a roton mode. More recently, the realization of BECs of the higly magnetic lanthanide dysprosium [23] and erbium [24], opened new possibilities for accessing the regime of dominant DDIs.

4.3 Observation of roton mode population in a dipolar BEC of strongly magnetic erbium atoms

In this section I will first give an overview of the experimental apparatus used at the ERBIUM experiment in Innsbruck for producing ultracold degenerate samples of ^{166}Er atoms. Then I will describe the experimental investigation of the roton mode in Er.

4.3.1 The ERBIUM experiment in Innsbruck

The ERBIUM experiment is a machine working with ultracold bosonic and fermionic erbium atoms. It can produce BECs of bosonic ^{168}Er [24] and ^{166} Er isotopes, containing up to 10^5 atoms, with a typical maximum density of 10^{14} cm^{-3} . The ^{168}Er isotope can also be used to create Er_2 molecules via magneto-association using a Feshbach resonance [124]. Moreover, degenerate Fermi gases can be realized by using the fermionic ^{167}Er isotope [125].

In the following I will focus on the description of the production of an ^{166}Er BEC, since this is the isotope with which I have been working. The first BEC of ^{166}Er has been achieved in 2016, before my arrival on the experiment [26].

Overview of the apparatus and experimental sequence for producing an ^{166}Er BEC The experimental apparatus, sketched in Fig.4.4, has been designed by F. Ferlaino and mainly his PhD student A. Frisch starting in 2009. It is described in detail in the PhD thesis of the latter (see ref. [43]). It includes the vacuum system and the laser sources used for cooling and trapping the atoms. The vaccum system is composed of two sections with different background pressures, connected via a differential pumping tube. The first section is at high vacuum (HV) and includes a high temperature oven, a transversal cooling stage and a first pumping stage. The second section is at ultra high vacuum (UHV) and contains a Zeeman slower, the main experimental chamber and a second pumping stage.

The two pumping stages in the two vacuum sections and the differential pumping tube provide a pressure of 4×10^{-9} mbar and 1×10^{-11} mbar in the HV and UHV parts, respectively. The high temperature oven uses an effusion cell,

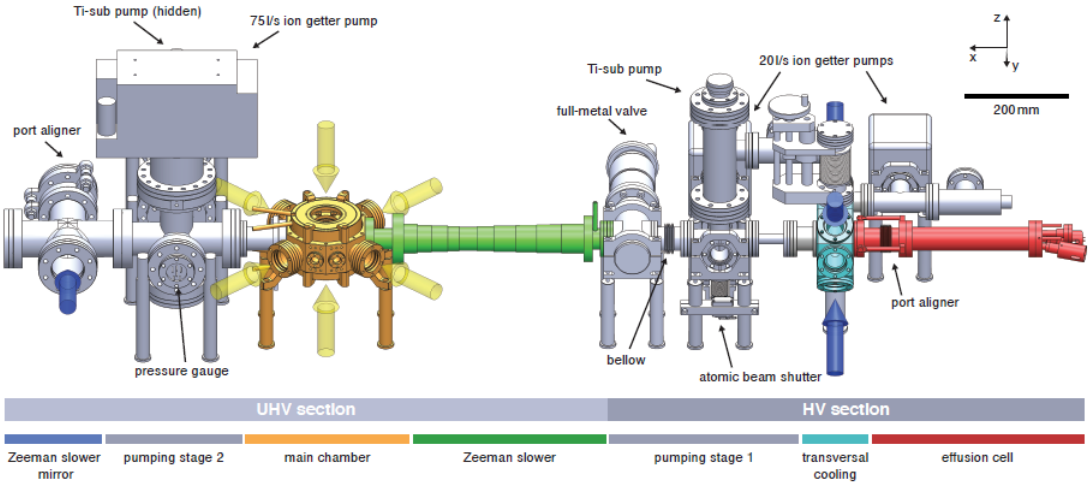

Figure 4.4: Drawing of the ERBIUM experiment vacuum system. The HV and UHV sections are shown. The starting point for the production of ultracold atomic samples is the high temperature oven, coloured in red on the right of the figure. The atoms are subjected to two stages of cooling (trasversal cooling, in blue, and Zeeman slowing, in green) before arriving at the main experimental chamber (in yellow in the figure). There, 3D magneto optical trapping is performed, followed by evaporative cooling in a crossed optical dipole trap. The blue and yellow arrows in the figure represent cooling light at 401 nm and 583 nm, respectively. Figure taken from [43].

containing small pieces of solid erbium. It is typically operated at 1100 °C. At this temperature erbium atoms can evaporate inside the oven. Then, a set of apertures is used to produce a collimated atom beam out of the oven.

After the oven, the atom beam is subjected to a first optical cooling stage, in two orthogonal directions transversally to the beam propagation direction. This allows to increase the atom flux along the longitudinal direction. The optical cooling, whose principle has been described in section 1.3.2, is performed on the broad 401 nm-wavelength transition of erbium, with a linewidth of $\approx 2\pi \times 30$ MHz [43]. After the transversal cooling, the atoms enter a Zeeman slower (see section 1.3.2). The Zeeman slower light is also operated at 401 nm. This allows to slow the atoms down along the longitudinal direction. With the Zeeman slower, the velocity of the atoms can be decreased by two orders of magnitude, reaching ≈ 8 m/s at the end of the Zeeman slower. This velocity is low enough for the atoms to be captured by a 3D MOT at the main experimental chamber. The MOT is operated on a narrow-

linewidth transition at a wavelength of 583 nm [50]. The linewidth of the atomic transition of $\Gamma \approx 2\pi \times 190$ kHz gives a Doppler temperature of $T_D \approx 4.6$ μK (see section 1.3.3). In this special narrow-line MOT the atoms are cooled down to a temperature of ≈ 15 μK and additionally, they are automatically spin-polarized to their lowest Zeeman sublevel [50]. For ^{166}Er typically 3×10^7 atoms are captured into the MOT after 3 s of MOT loading.

In order to bring the cold atomic sample to degeneracy, the atoms are first loaded from the MOT into a horizontal red-detuned far off-resonant optical dipole trap (ODT) at 1064 nm, propagating along the y-axis of Fig. 4.4, and with a tunable geometry. The horizontal ODT beam has a maximum power of 24 W, a vertical waist $w_z = 18$ μm, and a tunable horizontal waist, $w_x = \lambda' w_z$. The ellipticity of the horizontal ODT beam can be changed from 1.57 to 15 by time averaging the frequency of the first-order deflection of an Acousto-Optic Modulator (see ref. [126]). For ^{166}Er typically 7×10^6 atoms are loaded into the horizontal ODT using $\lambda' = 6$ and the maximum power available. For the two bosonic isotopes, an additional vertical 1064 nm ODT beam, propagating nearly collinear to the z-axis, is used. The vertical ODT beam has a maximum power of 7 W and an elliptical beam profile with waists of 110 μm and 55 μm along x and y, respectively. The two red-detuned ODTs cross at their respective focii, thus realizing a so-called crossed dipole trap. Here the atoms are subjected to forced evaporative cooling (see section 1.3.5). First the power and then the ellipticity of the horizontal ODT beam are changed in order to reach quantum degeneracy. During the evaporation sequence a uniform magnetic field is applied. It fixes the magnetization axis and set the value of the scattering length via the multitude of Feshbach resonances available in Er (see section 2.4 and ref. [75]). For ^{166}Er, the magnetic field is set to 1.9 G during the evaporation to optimize the elastic to inelastic collision ratio. We typically obtain a BEC of 10^5 ^{166}Er atoms, with a condensed fraction of $\approx 70\%$.

Imaging procedure Resonant absorption imaging (see section 1.4.1) on the broad-line at 401 nm is used to image the atoms at the end of the experimental sequence. Two optical setups are available for imaging in the experiment, one allows to image the atoms horizontally, approximately along the y-direction, and

the other setup provides a vertical imaging, approximately along the z direction. In the experiment that I will describe in the following, the horizontal imaging setup has been used for calibration of final atom number and condensate fraction in the BEC, and the vertical imaging setup for the science measurements. The atom number and the condensate fraction are determined by fitting the absorption images of the gas to a bimodal distribution, which is the sum of a Thomas-Fermi density profile (for the condensate) and a broad Gaussian density profile (for the background thermally excited atoms). With the vertical imaging the density distribution in the (xy)-plane perpendicular to the dipole direction can be measured.

The spatial resolution of the vertical imaging is 3.7 μm. In the experiment we employ time-of-flight (TOF) expansion measurements, accessing the momentum distribution of the gas [109]. The used TOF time of 30 ms translates the spatial imaging resolution into a momentum resolution of $\approx 0.32\ \mu\text{m}^{-1}$. The recorded 2D TOF absorption images of the cloud provide the spatial density distribution at a TOF time t_{TOF} on the (x, y) plane: $n_{TOF}(x, y, t_{TOF})$. We assume that this expanded density distribution directly maps the 2D in-trap momentum distribution $\tilde{n}(k_x, k_y)$, via the simple mapping:

$$\tilde{n}(k_x, k_y) = \left(\frac{\hbar t_{TOF}}{m}\right)^2 n_{TOF}\left(\frac{\hbar k_x t_{TOF}}{m}, \frac{\hbar k_y t_{TOF}}{m}, t_{TOF}\right). \tag{4.16}$$

which neglects the initial size of the cloud in the trap and the effect of interparticle interactions during the TOF expansion. Numerical simulations of the experimental sequence (see section 4.3.4) confirm that the interactions are negligible during the expansion, and justify the use of (4.16).

4.3.2 Choice of the trapping geometry

Before this work, rotons in dipolar BECs have been mostly connected to quasi-2D (pancake-like) geometries of the trap [35, 118, 119, 120, 121, 122, 123]. However, as emerges from the physical description based on the seminal work [35] (see section 4.2.2), the conditions for the presence of the roton minimum in the energy spectrum of a dipolar BEC are the peculiar anisotropic and long-range character of the DDI and a strong confinement along the direction of the dipoles. Apparently,

no strict constraints on the shape of the trap are necessary. In our work [37], the study of roton physics is extended to a largely unexplored (3D) geometry with trap elongation along only one direction (y) transverse to the magnetization axis (see Fig.4.5). This trap geometry is also indicated as *cigar-shaped*. Here, one expects a rotonization of the excitation spectrum along y.

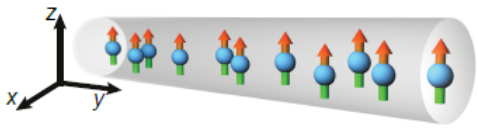

Figure 4.5: The axially elongated trap geometry used in the experiment. The dipoles are aligned transversely to the axis of the trap and subjected to a 3D harmonic confinement, with the thightest confinement along their orientation direction (z-axis). Figure adapted from [37].

This choice of the trap geometry is motivated by the choice of the experimental observable we want to measure in our investigation. Among the various consequencies of the emergence of a roton minimum in the dispersion relation, such as a reduction of the superfluid critical velocity below the velocity of sound, and a peaked structure factor (signal of strong two-body correlations), which have been measured in previous experimental works with non-dipolar BECs (see section 4.2.1, and references [112, 114, 115]), there is also another consequence, that is a peculiar momentum distribution of the atoms. We focus on this latter observable. As already discussed, in a dipolar BEC the roton energy gap $\Delta = \epsilon(k_{rot})$, depends on the density and on the strength of the interactions. In ultracold gases the scattering length a can be tuned using Feshbach resonances (see section 2.2). When a is reduced, Δ decreases, vanishes, and eventually becomes imaginary (Fig.4.3). In this case, the system undergoes a roton instability and the atoms in the condensate, that is the atoms with momentum $k_y = 0$, are transferred into the states at momentum $\pm k_{rot}$. The population of the roton mode should then be clearly visible in the momentum distribution of the gas. Now, in the extensively-studied pancake geometries, the roton population in momentum-space is expected to spread over a ring of radius $k = k_{rot}$ (Fig.4.6(a)), as follows from the discussion in section 4.2.2. Instead, in a cigar-shaped trap geometry the same roton population is ex-

pected to focus in two prominent peaks at $k_y = \pm k_{rot}$, thus providing an enhanced experimental signal with respect to the pancake case (Fig.4.6(b)).

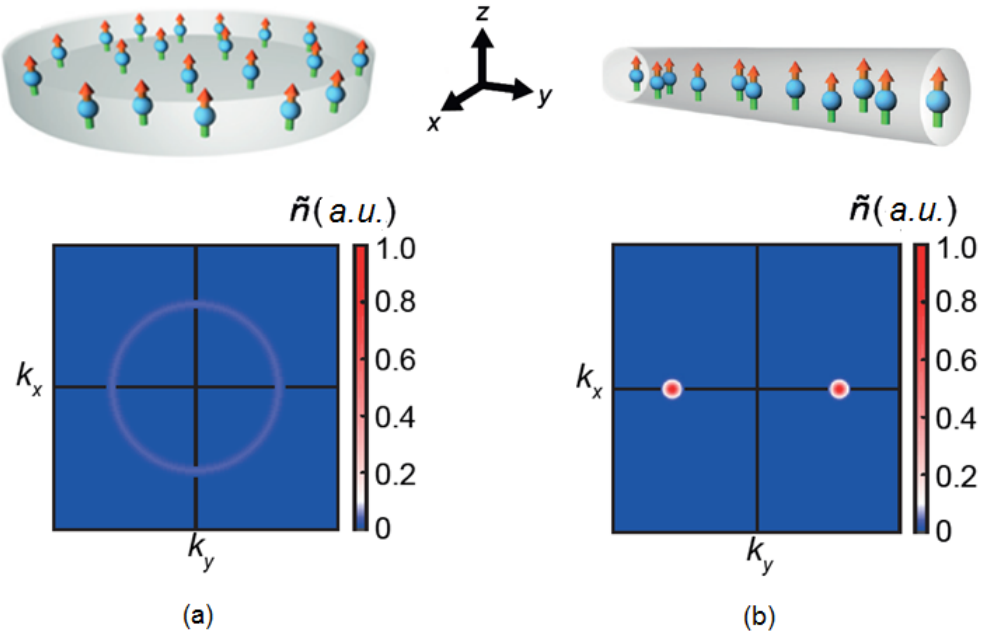

Figure 4.6: Signatures of the roton mode in the momentum distribution. (a) In a pancake trap the population of the roton mode manifests itself as a ring in the (k_x, k_y)-density distribution, indicated by $\tilde{n}$. An identical roton population focuses into two peaks in a cigar-shaped geometry **(b)**, thus producing an enhanced experimental signal. Figure adapted from [37].

Shaping of the trap The crossed optical dipole trap beams provide a harmonic trapping potential $V(\mathbf{r}) = 2m\pi^2(\nu_x^2 x^2 + \nu_y^2 y^2 + \nu_z^2 z^2)$, with frequencies (ν_x, ν_y, ν_z) along the three coordinate axes for the BEC. By adjusting independently λ' and the powers of the vertical and horizontal ODT beams, it is possible to dynamically control the geometry of the trap. In particular, the trapping frequency ν_y is essentially set by the vertical ODT beam power, while ν_z by that of the horizontal ODT beam. ν_x is controlled by both the power and ellipticity of the horizontal ODT beam, with $\nu_z/\nu_x \approx \lambda'$. The independent control of ν_y and ν_z allows to easily tune the relevant trap aspect ratio for the cigar-like geometry, denoted by $\lambda = \nu_z/\nu_y$. Once the BEC has been created, the beam parameters are changed

to shape the trap into an axially elongated configuration, favourable for observing the roton physics, that is $\nu_y \ll \nu_x, \nu_z$.

4.3.3 Measurements

Quench of the scattering length For ^{166}Er the dipolar length $a_{dd} = \mu_0\mu^2 m/12\pi\hbar^2 \simeq 65.5\ a_0$, which measures the strength of the DDI, is comparable to the estimated background s-wave scattering length $a_{bg} = 72(13)a_0$ [43]. In order to enter the dipole-dominated regime and be able to observe the roton physics, we make use of a magnetic Feshbach resonance to decrease the value of the scattering length sufficiently below the dipolar length. The chosen Feshbach resonance is centered around $B = 0$ G. For this resonance the B-to-a conversion has been previously precisely measured via lattice modulation spectroscopy, as reported in ref. [26] (see Fig.4.7). The errors on the estimation of the scattering length are of 3-to-5 a_0 for the relevant range of a of 27-67 a_0 explored in this work, and are due to statistical uncertainties of the conversion and effects of magnetic field fluctuations (for instance from stray fields).

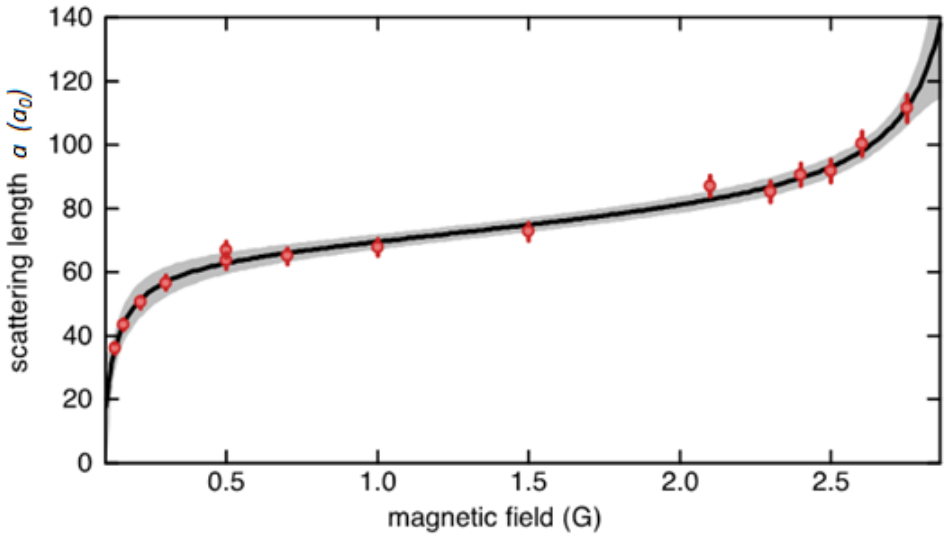

Figure 4.7: Scattering length as a function of the magnetic field. The data points (circles) are extracted from spectroscopic measurements of the gas in a optical lattice (see ref. [26]) and the solid line is a fit to the data with its statistical uncertainty (grey shaded region). Figure adapted from [26].

During the shaping of the trapping potential into the cigar-like geometry the magnetic field set value B_{set} is slowly (in 300 ms) changed from 1.9 G (the value at which the BEC is created, corresponding to a =80(2) a_0) to 0.4 G, which corresponds to a scattering length of 61 a_0. Thus, the experiment starts with a stable BEC with initial scattering length a^i = 61 a_0. To excite the roton mode we then perform a quench, i.e. a sudden variation, of the interactions into the dipole-dominated regime. This is done by abruptly changing B_{set} from 0.4 G to the desired lower value, corresponding to a final scattering length a^f. After the quench, the atoms are held in the trap for a variable holding time t_h, before being released from the trap for performing TOF imaging. Immediately after the trap is switched off, B_{set} is suddenly changed back to 0.3 G, corresponding to $a^{img} = 57$ a_0. This change guarantees constant and optimal imaging conditions with a fixed probing procedure of maximal absorption cross-section. In addition, the increase of a allows to minimize the time during which the dynamics happens in the regime of small-a values where the roton is populated, such that we effectively probe only the short-time evolution of the gas.

The experimental sequence for the scattering length is sketched in Fig.4.8. Because of delays in the experimental setup coming, for instance, from eddy currents in the main chamber, the actual B value felt by the atoms responds to a change of B_{set} via $B(t) = B_{set}(t) + \tau dB/dt$, see ref. [71]. By performing pulsed-radio-frequency spectroscopy measurements (with pulse duration of 100 μs) on a BEC after changing B_{set} (from 0.4 G to 0.2 G), this law has been verified in our system and τ has been calibrated to be $\tau = 0.98(5)$ ms. As a consequence, a is still evolving during the hold time and the TOF time and converges to its set value with a characteristic timescale of τ. This effect is accounted for in the experiment (and also in the simulations, discussed later), and in the following I will report the roton properties as a function of the effective value of a at a certain t_h. In order to investigate the short-time physics, yet long enough compared to τ, we focus here on t_h between 3 and 6 ms.

The momentum distribution $\tilde{n}(k_x, k_y)$ is then recorded as described in section 4.3.1. To investigate the excitation of the roton mode, the measurement is repeated at various values of $a^f < a_{dd}$ in a fixed cigar-shaped trap geometry. The observed $\tilde{n}(k_x, k_y)$ shows a striking behaviour (Fig.4.9). For large enough a^f, the

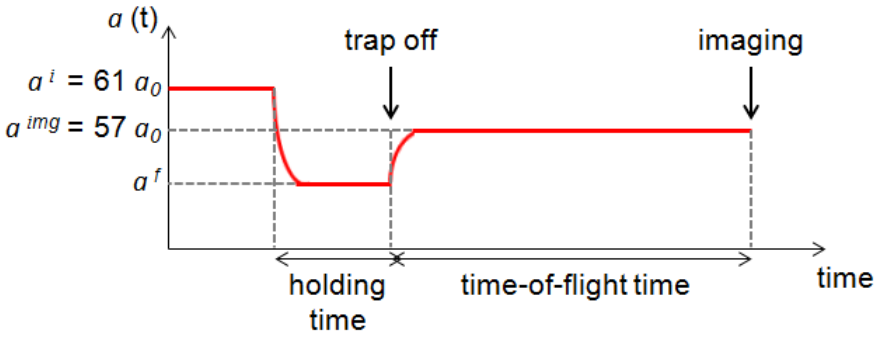

Figure 4.8: Experimental sequence for the scattering length.

momentum distribution shows a single central narrow peak with an inverted aspect ratio compared to the trapped gas, typical of a stable BEC with a macroscopic occupation of the condensate state with momentum $k_y = 0$ (Fig.4.9(a)). The center of the momentum distribution is defined as the origin of k_y. When the scattering length is decreased further below a_{dd}, we observe a sudden appearance of two finite-momentum peaks at the sides of the central one, which are of similar shape and symmetrically located with respect to $k_y = 0$. Decreasing even further a^f into the dipole-dominated regime, we see that the relative population of the two side peaks with respect to the central one increases (Fig.4.9(b), (c)). We repeat the experiment several times, and observe that the peaks consistently appear at the same positions, so that they are clearly visible in the averaged distributions. The robustness and reproducibility of these observations support our interpretation of the two finite-momentum peaks in the momentum distribution, appearing when quenching the scattering length into the dipole-dominated regime, as a signature of the roton mode population in our system.

To quantitatively investigate the structure of the peaks, a sum of three Gaussian distributions is fitted to the central cuts of the average $\tilde{n}(k_x, k_y)$ (Fig.4.9(d), (e), (f)), as detailed in ref. [37]. From the fit it is possible to extract the central momentum $|k_y| \equiv k_{rot}$ of the side peak.

Probing the scaling of the roton momentum As derived in [35], and confirmed in other theoretical works [118, 121, 120], a smoking gun of the roton mode in dipolar BECs is its geometrical scaling with the harmonic oscillator

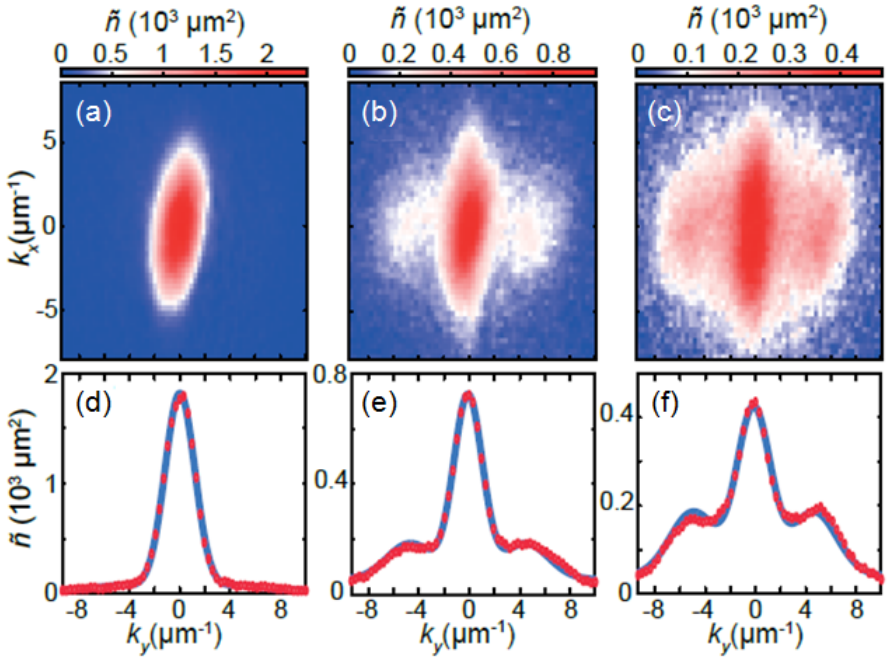

Figure 4.9: Observed roton peaks in momentum distribution. $\tilde{n}(k_x, k_y)$ obtained by averaging 15-to-25 absorption images for the trapping configuration (ν_x, ν_y, ν_z) = (267, 32, 456)Hz ($\lambda = 14.3$), with $t_h = 3$ ms, and $a^f = 54a_0$ **(a)**, $44a_0$ **(b)**, $37a_0$ **(c)**. **(d), (e), (f)** Corresponding central cuts at $k_x \approx 0$ (dotts) and their fits to three-Gaussian distributions (lines). Figure adapted from [37].

length along the tighter confined direction, $k_{rot} \sim 1/l_z$, where $l_z = \sqrt{h/m\nu_z}$ (see. Eq.(4.14)). Additionally, k_{rot} is expected to be almost independent on the scattering length close to the instability [35, 120]). In the experiment we study both dependencies.

In a first set of measurements, the quench experiment described above is repeated for different trapping configurations. In particular, we vary ν_z from ≈150 Hz to ≈800 Hz, while keeping ν_y almost constant during the experiment at about 35 Hz. This is possible thanks to the independent control we can have on the two trapping frequencies ν_z and ν_y in the experiment. The range of variation of ν_z corresponds to a tuning of the trap aspect ratio $\lambda = \nu_z/\nu_y$ from about 4 to 30 (the ratio ν_z/ν_x is instead kept constant during the experiment at about 1.6). All the explored trapping configurations are listed in Table 4.1.

Increasing the strength of the confinement along the z direction, we clearly

λ	ν_x (Hz)	ν_y (Hz)	ν_z (Hz)	N (10^4)	BEC$_f$ (%)	T (nK)
4.3	114	35	149	9	66	45
10.2	183	30	306	11	62	104
14.3	267	32	456	8.6	50	150
21.3	357	30	638	8.4	36	179
29.7	432	26	771	7	20	171

Table 4.1: Experimental parameters for the measurements reported in Figures 4.9 and 4.10. In the table, BEC$_f$ indicates the fraction of the total number of atoms N which are in the condensate, and T is the temperature. The typical statistical uncertainties on ν_x and ν_z are below 1%, and can be up to 10 % for ν_y. The experimental repeatability results in 5-to-10% shot-to-shot fluctuations of N, BEC$_f$ and T.

observe the expected geometrical scaling for the roton momentum. The measured values of k_{rot} increase linearly with $1/l_z$, with a slope of 1.61(4) (Fig.4.10(a)).

In a second set of measurements, we fix the trap geometry and investigate the dependence of k_{rot} on a. We observe that, within our experimental uncertainty, k_{rot} shows a smooth increase when decreasing a (Fig.4.10(b)).

4.3.4 Comparison to theory

In order to confirm our observations and get a deeper understanding of the roton population in our system, the experimental data are compared to two theoretical models, which have been specifically developed by L. Santos, F. W*ä*chtler, and R.M.W. van Bijnen, for our system parameters. These models are fully explained in ref. [37]. Here I will only report their main assumptions and results.

Analytical model The analytical model developed by L. Santos generalizes the results of ref. [35] to a non-radially symmetric trapping geometry. The starting point is the calculation of the low-energy excitation spectrum of the stationary BEC. The condensate is assumed to have a homogeneous density along the y-axis, i.e. it is not confined along y, and to be harmonically trapped along x and z. Thus, in the model the so-called local density approximation [109] is applied along the y-axis. Then, similarly to the approach detailed in section 4.2.2, in order to analyt-

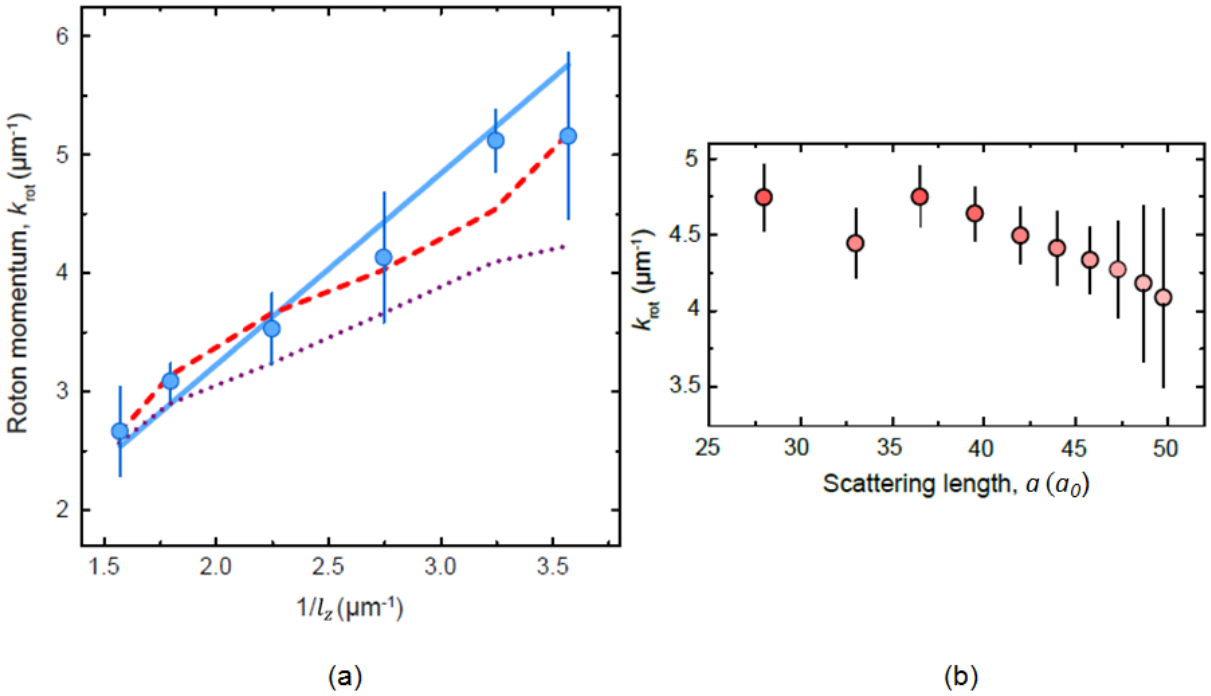

Figure 4.10: Characteristic scalings of the roton momentum. **(a)** Measured k_{rot} as a function of $1/l_z$ for the trapping configurations listed in Table 4.1 (circles). The solid line is a linear fit to the data, passing through the origin, with a slope of 1.61(4). The dotted and dashed lines are the predictions from the analytical model and the numerical simulations, respectively. **(b)** Measured dependence of k_{rot} on a^f for the trapping configuration (ν_x, ν_y, ν_z) = (267, 32, 456)Hz (λ = 14.3). Error bars show the statistical uncertainty from the fit. Figures adapted from [37].

ically evaluate the energy spectrum $\epsilon(k_y)$, the Thomas-Fermi (TF) approximation is used for the BEC wave function along the confined x and z directions. Under the above mentioned approximations, one finds that for dominant DDI ($\epsilon_{dd} \geq 1$), $\epsilon(k_y)$ for our cigar-shaped dipolar BEC indeed shows a roton minimum. At the instability, where the roton energy gap vanishes, the model predicts a simple geometrical scaling for the roton momentum, $k_{rot} \sim \kappa/l_z$, with the geometrical factor κ depending only on the ratio ν_z/ν_x. This stationary description thus accounts for the existence of the roton mode in the elongated geometry used in experiments, and predicts the scaling of k_{rot} with the system parameters [37]. The values of k_{rot} calculated from the analytical model for the various trapping configurations ex-

plored in our experiment are in good agreement with the measured ones, as shown in Fig.4.10(a).

Numerical simulations The system dynamics under the quench of the scattering length has been numerically simulated by F. Wächtler and R.M.W. van Bijnen. They calculated the time evolution of a generalized non-local Gross-Pitaevskii equation (gNLGPE) of the form:

$$i\hbar\frac{\partial}{\partial t}\Phi_0(\mathbf{r},t) = \left(-\frac{\hbar^2\nabla^2}{2m} + V_{ext}(\mathbf{r}) + gn + U_{dd}(\mathbf{r},t) + \Delta\mu[n] - i\hbar\frac{L_3}{2}n^2\right)\Phi_0(\mathbf{r},t) \tag{4.17}$$

which constitutes an extension of the NLGPE introduced in Eq.(2.56), with two additional terms in the right-hand side operator. The fifth term accounts for the effect of quantum fluctuations, which can be accurately included in the NLGPE in a mean-field treatment through the so-called Lee-Huang-Yang (LHY) correction to the chemical potential, obtained under a local density approximation [127, 128]:

$$\Delta\mu[n] = \frac{32}{3\sqrt{\pi}}g(na)^{3/2}\left(1+\frac{3\epsilon_{dd}^2}{2}\right). \tag{4.18}$$

The sixth term describes three-body inelastic loss processes (see section 2.3) via a non hermitian term [129]. It includes an experimentally determined loss parameter L_3, which depends on a, and is typically of the order $L_3 \simeq 10^{-41}$ m^{6}s^{-1}, as reported in ref. [26].

The importance of the combined effect of these two terms in the dynamics of dipolar BECs has been estabilished by recent theoretical and experimental results (see, for instance, [130, 131, 132, 133, 26]), which have proven that, on one hand, three-body losses limit the peak density of the atomic cloud, and on the other hand, quantum fluctuations constitute the leading mechanism for stabilizing dipolar BECs against collapse.

The effect of a finite temperature is additionally accounted for in the simula-

tions by populating the excited states of the system. The excited states used in this procedure are the eigenstates of the harmonic trap, as in ref.[130].

The simulations reproduce as close as possible the conditions of our experiments, including initial atom number in the BEC, temperature, trapping frequencies, ramping, holding, and TOF times. Moreover, the exact experimental sequence for the scattering length is included in the numerics. From the simulated evolution, the 3D wavefunction of the gas is obtained as a function of t_h, $\Phi_0(\mathbf{r}, t_h)$, from which the spatial and momentum distributions can be extracted. In particular, the integrated momentum distribution $\tilde{n}(k_y, t_h) = \int dk_x dk_z |\tilde{\Phi}_0(\mathbf{k}, t_h)|^2$, with $\tilde{\Phi}_0(\mathbf{k}, t_h)$ the Fourier transform of $\Phi_0(\mathbf{r}, t_h)$, can be evaluated. The calculations show that, few ms after the quench, the system developes roton peaks in the integrated momentum distribution $\tilde{n}(k_y, t_h)$, and real-space short-wavelength density modulations at the centre of the BEC, verifying the predicted "roton confinement" phenomenon [121], according to which the density modulation corresponding to a roton instability in a dipolar BEC is confined in the trap centre, where the density of the gas is maximal. The values of k_{rot} extracted from the calculated momentum distributions for the different trap configurations used in the experiment, and their geometrical scaling, are in very good quantitative agreement with both the experimental data and the analytical model calculations, as shown in Fig.4.10.

Numerical simulations are also performed to control the validity of the mapping (4.16) used in the experiment. In fact, they provide both the real momentum distribution from the in-trap wave function, and the expanded spatial distribution after 30 ms of ballistic expansion. The two values of the roton momentum extracted from the two calculated distributions agree within 5%, thus confirming that the interactions have a small importance during the expansion for our system parameters.

4.4 Complementary simulations of the time evolution

To have a further insight into the dynamics of our system induced by the quench of the scattering length, I have personally carried out time evolution simulations,

using the code written by R.M.W. van Bijnen. In particular, in my simulations I focused on the in-trap dynamics. In a first set of simulations, I calculated the time-evolution for varying t_h of the dipolar BEC following the quench of a to different final values a^f, for a fixed trap geometry. From the simulated wavefunction, I extracted the spatial density distribution as a function of t_h, which gives access to information not accessible in the experiment. I will present an analysis of this information. In a second set of simulations I concentrated on the specific effects of quantum fluctuations and three-body losses on the system dynamics, by artificially switching on and off these terms in the simulations based on the gNLGPE (4.17). By comparing the time evolution of the in-trap density in the different cases, I analyzed the specific role of each of these terms. In the following I will first describe the main features of the code from R.M.W. van Bijnen, and then present the results.

4.4.1 The code

The simulation is based on a numerical procedure considering a discrete version of the 3D wave function of the gas and it calculates the time evolution of the wave function along the gNLGPE (4.17) using discrete time steps. The code can accomplish two distinct tasks. First, it can compute the ground state of the gNLGPE. Second, it can calculate the real-time evolution of any 3D wave function along the gNLGPE. For both tasks I will summarize here the main computational steps.

Features of the numerical computation

- The wave function considered by the program is defined on a discrete spatial grid in the coordinates $\mathbf{r} \equiv (x, y, z)$, with $N_x \times N_y \times N_z$ grid points, which constitutes the "simulation box". Typical values for the grid points are $N_x = 128$, $N_y = 512$, $N_z = 64$. In order to describe the evolution along Eq.(4.17) without being limited by edge effects, the grid typically has an extent in all spatial directions at least three times bigger than the size of the BEC wave function in the corresponding direction.

- A key point consists in using the convolution theorem to calculate the DDI potential term $U_{dd}(\mathbf{r}) = \int d\mathbf{r}' V_{dd}(\mathbf{r}-\mathbf{r}')n(\mathbf{r}')$, which is a convolution of the DDI potential $V_{dd}(\mathbf{r}-\mathbf{r}') = \frac{\mu_0\mu_m^2}{4\pi}\frac{1-3\cos^2\theta}{|\mathbf{r}-\mathbf{r}'|^3}$ with the 3D spatial density $n(\mathbf{r}) = |\Phi_0(\mathbf{r})|^2$. The $\sim 1/r^3$ behaviour of the DDI potential can lead to difficulties in the calculations when the integral U_{dd} is discretized onto a real-space grid. For instance, for each grid point of coordinate $\mathbf{r}$, the integral becomes a sum over the entire spatial grid (sum over all $\mathbf{r}'$), and the divergence corresponding to the $r = 0$ pole of the DDI potential can not be treated numerically. In order to overcome this complication, and since $V_{dd}(\mathbf{r})$ and $n(\mathbf{r})$ have both well defined Fourier transforms, one can move to momentum space. Then the real-space convolution defining $U_{dd}(\mathbf{r})$ becomes a simple product in Fourier space: $U_{dd}(\mathbf{r}) = \mathcal{F}^{-1}[\tilde{V}_{dd}(\mathbf{k})\tilde{n}(\mathbf{k})](\mathbf{r})$, where $\mathcal{F}^{-1}[\cdot]$ indicates the inverse Fourier transform, and $\tilde{\cdot}$ indicates the direct Fourier transform. Note that $\tilde{V}_{dd}(\mathbf{k})$ is analytically well defined, and given by $\tilde{V}_{dd}(\mathbf{k}) = \frac{\mu_0\mu_m^2}{3}(3\cos^2(\theta_k)-1)$, with θ_k the angle between $\mathbf{k}$ and the polarization axis.

- The kinetic energy term is also conveniently calculated in momentum space. In fact, the kinetic energy operator $\hat{T} = -\nabla^2$ has the simple diagonal form in momentum space $\hat{\tilde{T}} = k^2$. Thus, $-\nabla^2\psi(\mathbf{r}) = \mathcal{F}^{-1}[k^2\tilde{\psi}(\mathbf{k})]$.

Ground state calculation

- Note that Eq.(4.17) can be obtained through a variational approach [78]:

$$i\hbar\frac{\partial}{\partial t}\Phi_0 = \frac{\delta E}{\delta\Phi_0^*}, \tag{4.19}$$

where the energy functional E is given by

$$E[\Phi_0] = \int d\mathbf{r}\left[\frac{\hbar^2}{2m}|\nabla\Phi_0|^2 + V_{ext}(\mathbf{r})|\Phi_0|^2 + \frac{g}{2}|\Phi_0|^4 + \frac{3g\epsilon_{dd}}{8\pi}\times \right.$$
$$\left.\int d\mathbf{r}'|\Phi_0(\mathbf{r}')|^2\frac{1-3\cos^2\theta}{|\mathbf{r}-\mathbf{r}'|^3}|\Phi_0(\mathbf{r})|^2 + \Delta\mu[|\Phi_0|^2]|\Phi_0|^2 - i\hbar\frac{L_3}{2}|\Phi_0|^6\right] \tag{4.20}$$

Thus, finding the ground state is equivalent to minimize the energy functional (4.20).

- The numerical minimization of (4.20) is done by using the *conjugate gradients* algorithm [134]. The idea of this method is to sample the variations of the energy functional $E[\Phi_0]$ on a large scale. One starts from minimizing the energy functional $E[\Phi_0]$ by considering an initial wavefunction $\Phi_{0,0}$, which is assumed to be a Gaussian in the code. The wavefunction is then changed by considering the direction of the most negative gradient $\delta E/\delta\Phi_0^*$ around the initial $\Phi_{0,0}$. The direction of the next change of Φ_0 is then constructed iteratively by a linear combination between the direction of most negative gradient evaluated at $\Phi_{0,n-1}$ and $\Phi_{0,n-2}$ (or all $\Phi_{0,n'}$ with $n' < n$), to construct the new $\Phi_{0,n}$. This is iteratively repeated until the minimum of the energy functional is found, i.e. the gradient in that point is zero. In the code, the condition of zero gradient is assumed to be achieved when the gradient amplitude reaches values smaller than a threshold that can be set by hand. With this method the ground state wave function is typically calculated in few tens of seconds. Other typically used techniques for function minimization, such as the *imaginary time evolution* method [134], have been demonstrated to provide a much slower convergence for the specific case of a Gross-Pitaevskii energy functional, as reported, for instance, in ref. [135].

Time evolution The time evolution of the gNLGPE (4.17) is calculated using the *split-step* method (see, for instance, ref. [136]). In this method, one considers the time-independent hamiltonian $\hat{H}$ as given by the sum of the kinetic energy term $\hat{T}$ and the potential energy term $\hat{V}$, $\hat{H} = \hat{T}+\hat{V}$. Here, the effective potential energy for the evolution includes the external trapping potential, the interparticle interactions, the LHY correction and the three-body loss term. The evolution operator over a time Δt can be approximately split as $e^{-i\hat{H}\Delta t/\hbar} = e^{-i\hat{T}\Delta t/\hbar}e^{-i\hat{V}\Delta t/\hbar}+O(\Delta t^2)$, where the two operators $-\frac{i}{\hbar}\hat{T}\Delta t$ and $-\frac{i}{\hbar}\hat{V}\Delta t$ do not commute in general. The time evolution operator $e^{-i\hat{H}\Delta t/\hbar}$ can now be efficiently calculated exploiting the fact that the operator $\hat{T}$ is diagonal in momentum space, and the operator $\hat{V}$ is diagonal in real space. Thus, in a certain time step Δt one can calculate only

$e^{-i\hat{V}\Delta t/\hbar}\psi$ in real space, and in the subsequent time step only $e^{-i\hat{T}\Delta t/\hbar}\psi$ in momentum space, alternatively, with the wave function that is continously Fourier transformed back and forth between each step. This turns out to be much faster than exponentiating a non-diagonal matrix. The computational speed is then ultimately determined by the size of the simulation box. The simulations I present here have been obtained using the computational facilities of HPC infrastructure LEO of the University of Innsbruck. The computation of the time evolution of the 3D wavefunction during a typical t_h up to 80 ms took about 15 hours.

Approximations used in the code

- The temperature is taken to be zero in the simulations, and the initial wavefunction is assumed equal to the ground state wavefunction. The numerical calculations reported in [37] have demonstrated that the effect of a finite temperature is to seed the population of the roton mode. This means that, if the temperature is not accounted for in the simulations, the initial population of the roton mode is expected to be delayed towards longer holding times. However, the the rapid dynamics after the seeding of the roton excitation can be considered as weakly affected by the temperature.

- In the simulations, the time evolution is calculated after an abrupt change of a, controlled by the correlated variation of B, as performed in the experiment. The variation in time of the magnetic field (and scattering length) during the experiment is simulated by using a linear ramp, instead of the experimentally measured exponential ramp (see section 4.3.3). To extract the corresponding variation of a, we use the experimentally calibrated conversion (see section 4.3.3). It is worth to note that as $T = 0$ is taken, the exact time variation at short t_h are not expected to match the experimental observations and the influence of the specific ramp should be negligible.

- The values of the three-body loss parameter L_3 for different scattering lengths are determined via a linear interpolation of the measured data reported in ref. [26].

From the 3D wave function of the gas in-trap after a hold time t_h, $\Phi_0(\mathbf{r}, t_h)$, it is possible to extract the 1D density distribution $n_1(y, t_h) = \int dxdz|\Phi_0(\mathbf{r}, t_h)|^2$ integrated along the two confined directions x and z. The 1D density profile along the elongated direction of the trap should reveal the population of the roton mode in real space, in the interesting region of parameters. This should appear through the formation of density modulations, which can not be directly observed in our experiment due to a limited spatial resolution of the imaging system.

4.4.2 In-trap dynamics after the quench of the interactions

In my simulations I consider a BEC of ^{166}Er atoms with an initial atom number $N = 10^5$, confined in a cigar-shaped trap with trapping frequencies $(\nu_x, \nu_y, \nu_z) = (156, 17, 198)$ Hz ($\lambda = \nu_z/\nu_y = 11.6$), and dipoles aligned along the tighter confined z direction by an external uniform magnetic field. The initial value of the external magnetic field is 0.8 G, corresponding to an initial scattering length for the atoms of $a^i = 67a_0 > a_{dd}$, for which the BEC is stable. In order to enter the dipole-dominated regime of interactions, a is abruptly changed to a variable final magnetic field corresponding to a final scattering length a^f below the dipolar length. The atoms are then held in the trap at a^f for a holding time t_h varying from 0 to 80 ms. Differently from what is done in the experiment, here the trap is always kept on, and the scattering length is not quenched back to a higher value. This allows to access the in-trap dynamics not only immediately after the quench of the interaction, but also at longer times.

The calculated time evolution of the 1D integrated density profile $n_1(y, t_h)$ for different values of a^f reveal a complex in-trap dynamics. Fig.4.11 shows plots of the 1D integrated density distribution obtained for a^f between $60a_0$ and $45a_0$. One can clearly distinguish three regimes. For $a^f \geq 53a_0$ the BEC is stable, and one simply observes breathing modes of the BEC size. The quench to $a^f \leq 53a_0$ causes a stronger compression of the cloud with respect to the quench to $60a_0$, and this explains the larger loss of atoms at the lower final scattering length. For $52a_0 \leq a^f \leq 48a_0$, after a consistent loss of atoms due to the initial cloud compression, density modulations form at the centre of the trap. The amplitude of the modulations increases for decreasing a^f, and is maximal at $a^f = 48a_0$. Finally,

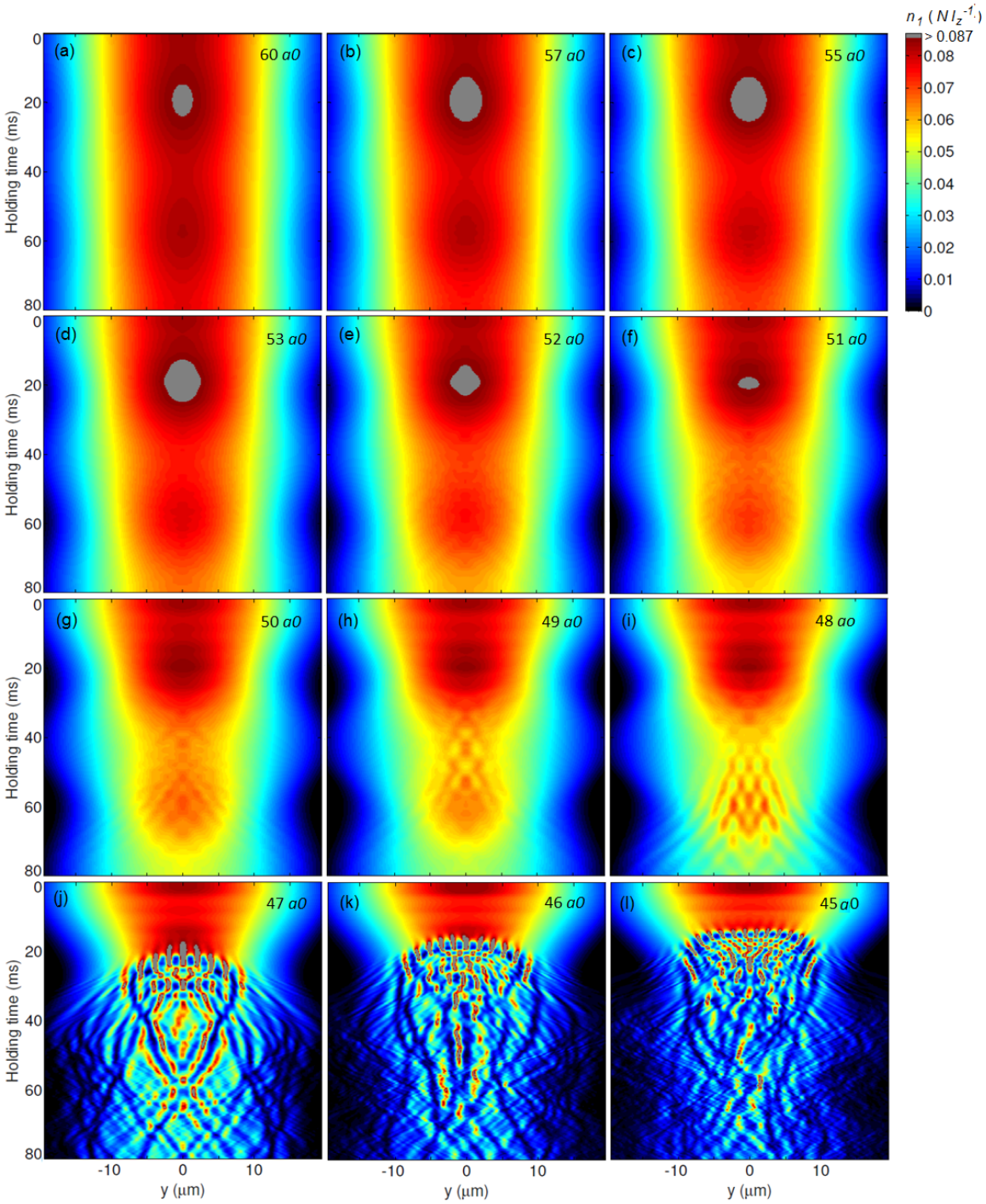

Figure 4.11: In-trap time evolution. Calculated time evolution of the 1D integrated density $n_1(y, t_h)$ after the quench of a to different values of a^f for the trap indicated in the text. Before the quench, $a^i = 67\ a_0$. a^f is indicated at the top right of each plot. The color-scale for n_1 is given in units of the initial atom number $N = 10^5$ times the inverse of the harmonic oscillator length l_z.

for $a^f \leq 47a_0$, after a similar appearance of density modulations, a completely different dynamics takes place: high-density structures develop, survive for few ms, and then merge in new structures with a lower density, until the atoms are completely lost. The lifetime of the structures seems to decrease with decreasing a^f. One can also note that the fuzzyness of the observed pattern gets stronger when lowering a^f. Fig.4.12 shows cuts of the 1D integrated density profiles at relevant holding times, in each of the three regimes of final scattering length discussed above.

The three regimes observed in the real-space dynamics can be interpreted in terms of the roton physics. For sufficiently high a^f, the roton mode is not excited, and therefore the condensate remains the only state macroscopically occupied. For $a^f \leq 52a_0$ the roton mode starts to be populated. When decreasing a^f, the roton energy gap also decreases (see section 4.2.2), and may reach $\Delta^2 < 0$ in the course of the dynamics for sufficiently low a^f. When this happens, the roton mode can get macroscopically populated. The fact that the modulations in the 1D density profile form at the centre of the trap (see Fig.4.12(b)), where the density of the cloud is maximal, verifies the previously mentioned roton confinement in this intermediate regime for the scattering length [121]. The distinct dynamics happening for $a^f <$ or $> 47a_0$ can be explained by the latter evolution of the roton gap. For $a^f > 47a_0$, the population of the roton excitation seems to temporarily increase but then it remains limited (not the full population of the BEC is transferred in a full contrast modulation). This behaviour should be explained by a roton gap temporarily reaching imaginary values, but recovering later a finite real value. This evolution is possible thanks to the variation in time of the density that we observed (in particular its decrease). A decrease of the density is induced either by the atom losses or by the oscillation of the size of the BEC, as observed in Fig.4.11. Note that oscillations of the size of the BEC also occur along x and z, leading to additional peak density variations, which are not sensitive in Fig.4.11. For $a^f < 47a_0$, on the contrary, the roton exictation population increases up to forming very strong modulations of the density profile (see Fig.4.12(c)). In this case, the dilute BEC dissapears and one traditionally talks about collapse dynamics (see, for instance, [118, 119, 120]).

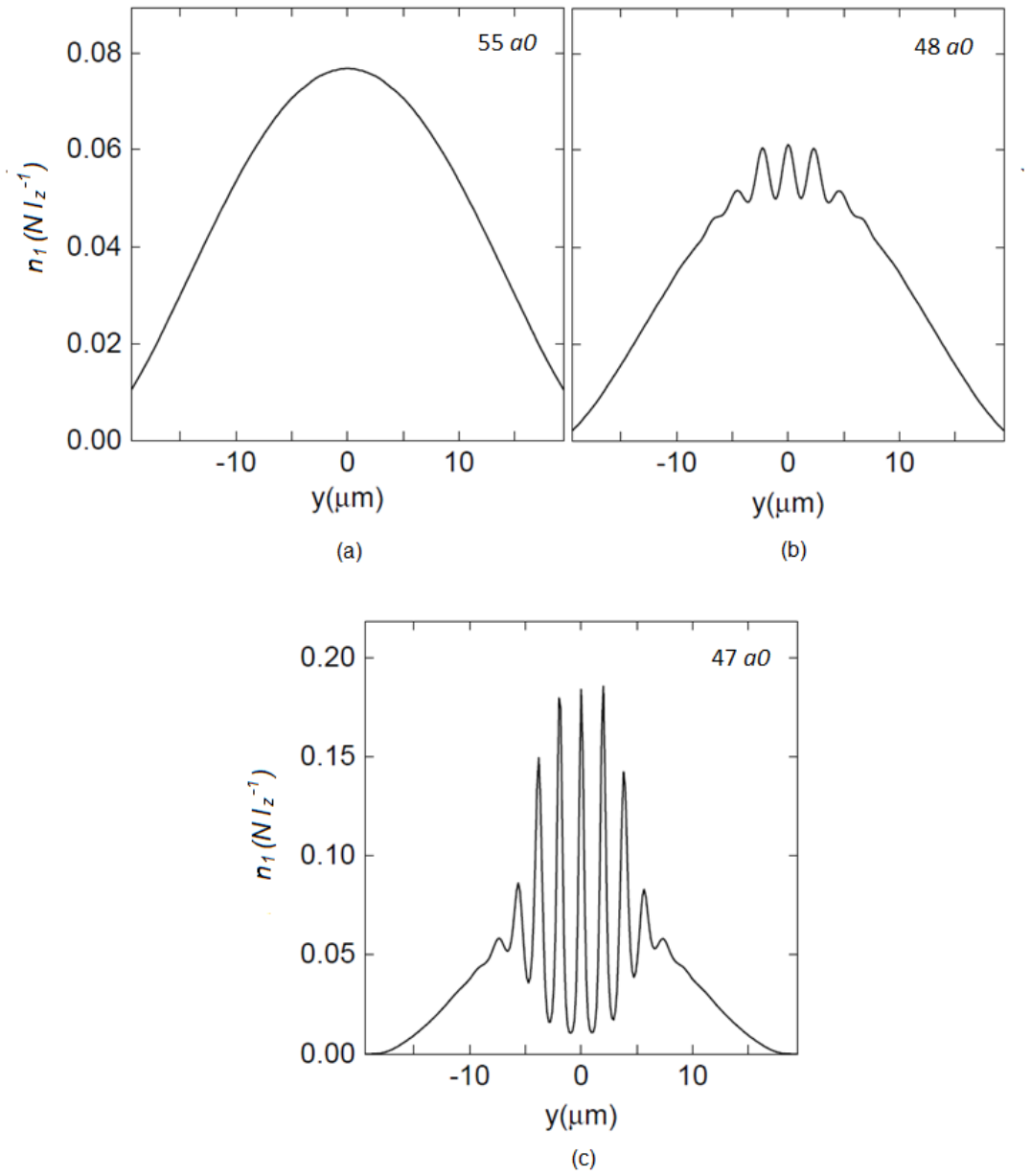

Figure 4.12: 1D integrated density profile $n_1(y)$ at various relevant t_h for three different values of a^f. **(a)** The cut of $n_1(y, t_h)$ for $a^f = 55a_0$ (Fig. 4.11(c)) at $t_h = 42$ ms shows a stable BEC profile. **(b)** A density-modulated profile characterizes the centre of the cloud for $a^f = 48\ a_0$ (Fig.4.11(i)), at $t_h = 48$ ms. **(c)** For $a^f = 47a_0$ (Fig. 4.11(j)), the cut of $n_1(y, t_h)$ at $t_h = 23$ ms reveals the formation of high-density structures in the system. Note the different scale on the y-axis of Figure (c) with respect to Figures (a) and (b).

Effect of quantum fluctuations In the last few years, the role of quantum fluctuations has been theoretically and experimentally demonstrated to be of primary importance in determining the dynamics of a dipolar BEC when reaching the regime where traditionally a collapse occur [130, 131, 132, 133, 26]. As discussed above, this is exactly the case investigated here, and in particular in the regime of Fig.4.12(c). In this regime, corresponding to the arising of the collapse, the total mean-field energy of the dipolar BEC vanishes. Now, a special property of dipolar BECs comes from the fact that this cancellation of the mean-field energy is achieved through the competition of two interaction terms, the DDI and the contact interactions, and in particular the mean-field energy cancels at non-zero scattering length. For example, in our case, it seems to cancel at around $a \sim 50a_0$. In this case, the energy contribution coming from the intrinsic quantum fluctuations of the system, i.e. beyond the zeroth order mean-field energy, does not cancel, and can thus dominate over the vanishing mean-field energy. This effect has been proven to yield the stabilization of mean-field collapsing BECs and the formation instead of so-called *quantum droplets*, constituting a novel metastable liquid-like state of matter, primarily observed in Dy [32, 133, 137, 138] and later in Er [26].

It is important to note that quantum droplets have been at first observed in the form of assemblies in the case where a stronger confinement was applied along the dipole orientation, either in pancake [32] or in cigar [133] traps. The formation of a structured metastable droplet assembly may have some connection to short-wavelength instabilities of the roton type. The study of this connection constitutes a very interesting question for future studies and better understanding of the physics at play here.

In order to investigate the effect of quantum fluctuations on our system, I repeated the time evolution simulations described in the previous section, but this time I did not include the LHY contribution in the gNLGPE (4.17). The results are presented in Fig.4.13, for relevant values of a^f, some of which are also used in Fig.4.11, thus allowing for a direct comparison between the two cases with and without quantum fluctuations included into the calculation.

In Fig.4.13 one can still observe the three regimes of scattering length discussed

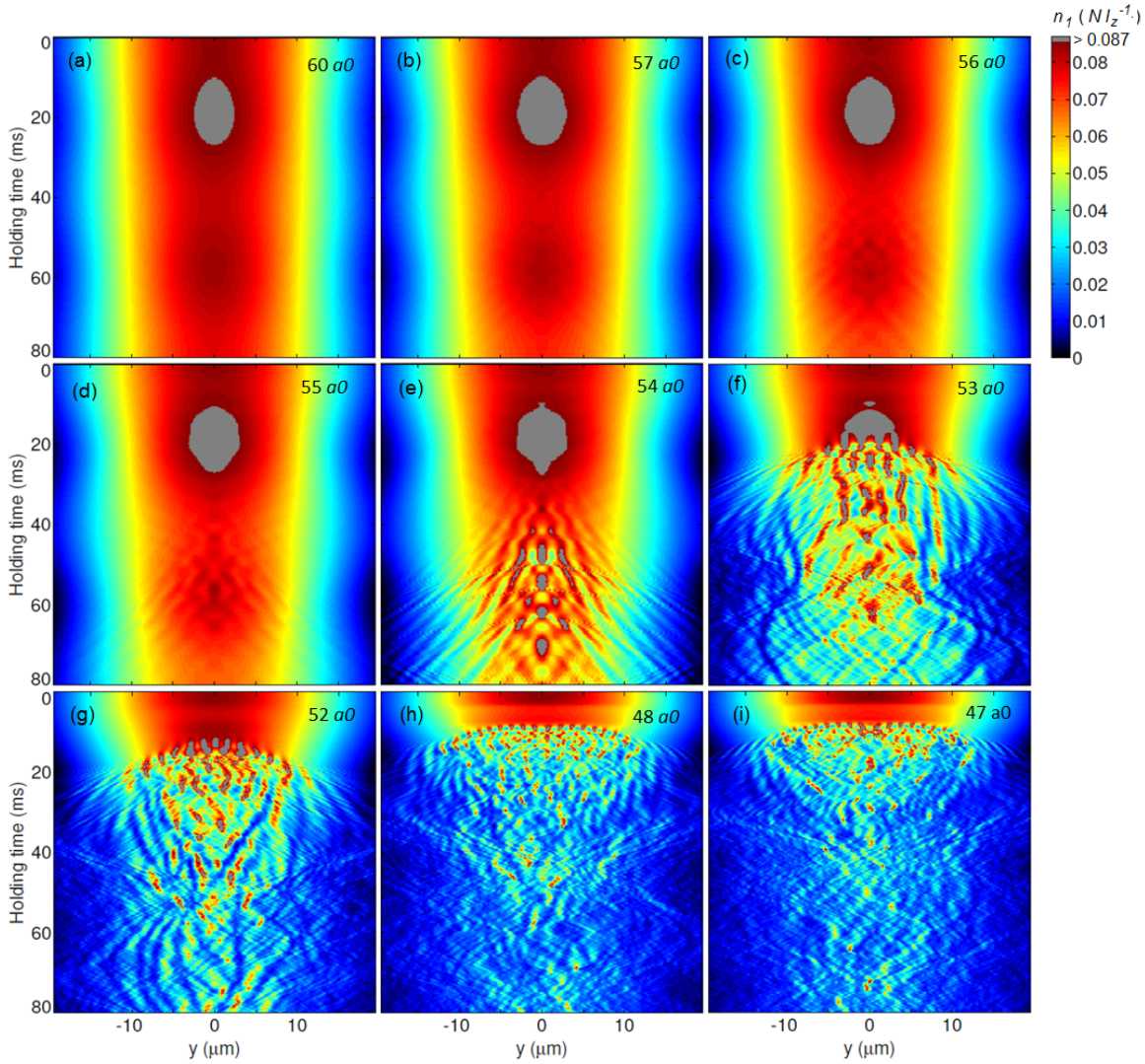

Figure 4.13: In-trap time evolution without LHY. Calculated time evolution of the 1D integrated density $n_1(y, t_h)$ as in Fig.4.11, but without including the effect of quantum fluctuations. Before the quench, $a^i = 67\ a_0$. a^f is indicated at the top right of each plot. The color-scale for n_1 is given in units of the initial atom number $N = 10^5$ times the inverse of the harmonic oscillator length l_z.

in the previous section, corresponding to a stable system for sufficiently high a^f, an intermediate regime with a density modulated profile corresponding to a populated roton mode, and an unstable system for smaller a^f. The first noticeable effect of the quantum fluctuations is that, in their absence, these three regimes are shifted towards higher values of a^f. Now a roton population appears already at $a^f = 57a_0$, instead of $52a_0$, and the instability appears at $a^f = 53a_0$ instead of $47a_0$, as previously. This proves the stabilizing role of quantum fluctuations in a dipolar BEC, pushing the energy gap of the roton to higher values. The second effect of the quantum fluctuation is on the structures of the density pattern themselves. For a^f in the unstable regime, one observes a much fuzzier and asymmetric dynamics, indicating more intricate nonlinear effects, and in particular the possible occurrence of density spikes (local collapses) not well described within the discrete numerical method I have used. Also, the revival of the density modulation structure after the first merging is in this case more limited than with the LHY contribution. Finally, one can observe the formation of smaller and smaller structures when decreasing a^f, which was not observed when quantum fluctuations were taken into account (compare Figures 4.11(i), (j), (k) with Figures 4.13(g), (h), (i)).

In the a^f range where a limited population of the roton mode is observed, between 57 a_0 and 55 a_0, I have checked that the wavelength of the modulations is equal, within the errors coming from a sinusoidal fit of the modulations, to the one obtained when the quantum fluctuations are accounted for in the calculations.

Effect of three-body losses Because of its strong dependence on the condensate density n, as $\sim n^2$, the three-body loss term in the gNLGPE (4.17) prevents the density from becoming too high. In order to study the effect of three-body losses on the dynamics of the system following the quench of the scattering length, I perform numerical simulations of the time evolution without taking into account the loss term. These results are presented in Fig.4.14 for the relevant values of a^f, and can be compared to the ones in Fig.4.11, where the losses are included into the calculations, and all the other parameters are kept the same. The difference between the two sets of calculations, with and without the three-body loss contribution, is particularly striking at low values of a^f. From the plots in Fig.4.14, one can again recognize a regime of stability of the BEC for $a^f \geq 53a_0$, and modula-

tions of limited amplitude for $52a_0 \leq a^f \leq 50a_0$. This indicates that for $a^f > 50a_0$, the instantaneous roton gap is destabilized and stabilized again by the breathing oscillation of the BEC size.

For $a^f \leq 49a_0$, the density profile shows the formation of high density long-lived structures, with a well-defined inter-structure separation distance, slightly oscillating because of the breathing of the whole cloud itself (see, in particular, Figures 4.14(g), (h), (i)). The stability of the structure contrasts with the short time scale dynamics of merging and splitting of the structure observed in presence of losses. One can see that both the size and separation distance of the structures decrease for decreasing a^f, and the number of the structures increase.

The observed stable structures are very similar to the quantum droplets. It is worth noticing that droplet arrays have been reported for a dipolar BEC of Dy atoms in an elongated trap with a similar geometry as in our experiment [139]. In that system, the stronger dipolar character of Dy with respect to Er is such that smaller densities are necessary for stabilizing the droplet state. Thus, the roton excitation might be interpreted as the triggering mechanism for an instability leading to the formation of droplet arrays in dipolar BECs. As pointed out in ref. [139], the observed droplet arrays do not constitute the ground state of the system, but rather excited metastable states. This is indeed consistent with a roton modulation instability obtained after a quench of the interaction energy, which prevents the access to the ground state of the system.

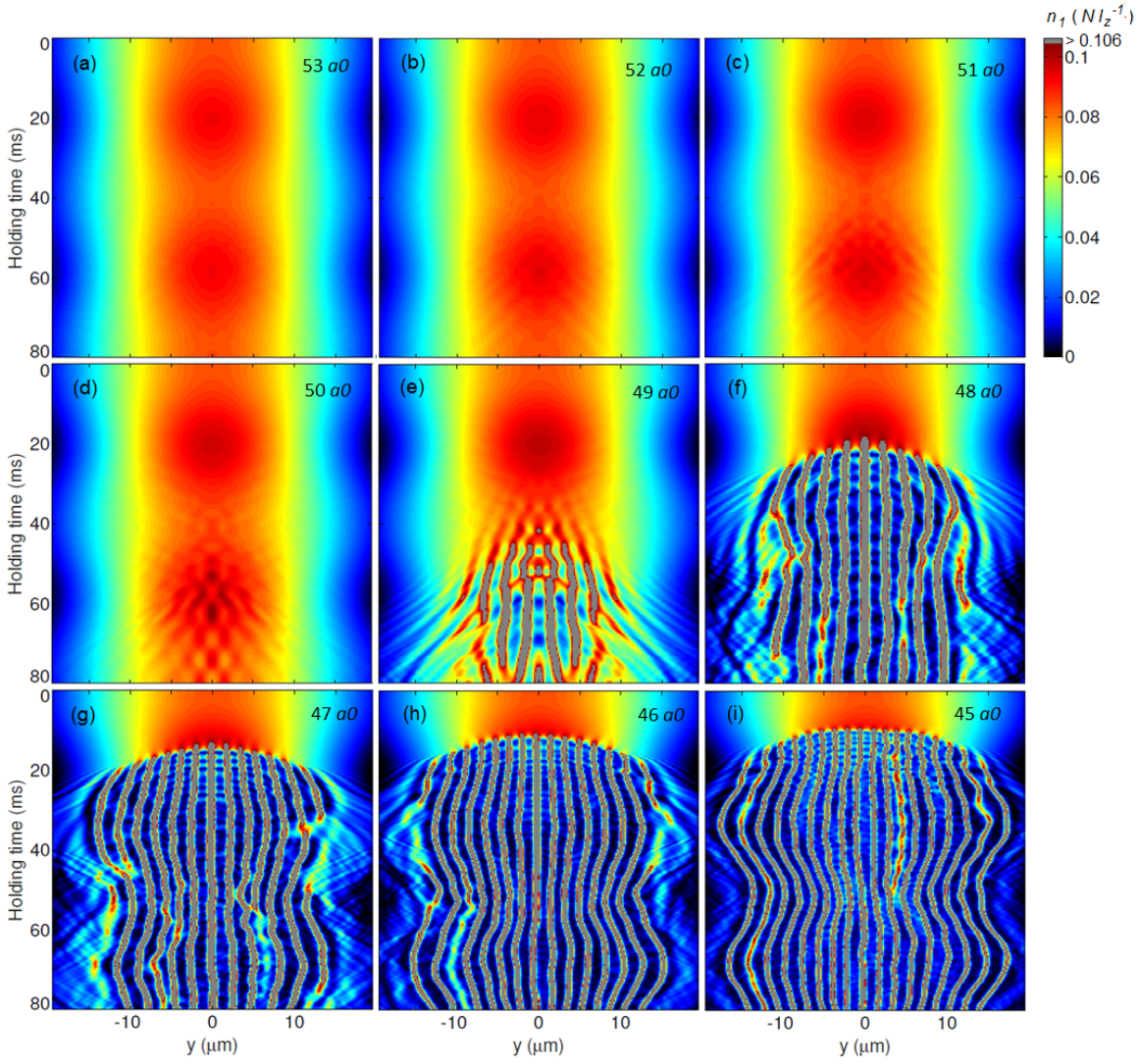

Figure 4.14: In-trap time evolution without three-body losses. Calculated time evolution of the 1D integrated density $n_1(y, t_h)$ as in Fig.4.11, but without including the effect of three-body losses. Before the quench, $a^i = 67\ a_0$. a^f is indicated at the top right of each plot. The color-scale for n_1 is given in units of the initial atom number $N = 10^5$ times the inverse of the harmonic oscillator length l_z. Note the different color-scale with respect to Figures 4.12 and 4.13.

Conclusion and outlook

This thesis focuses on the experimental study of quantum gases with tunable interatomic interactions of short- and long-range. During my PhD work I had the opportunity to experience two fundamental aspects of an experimental ultracold atomic physicist's formation, that is designing an experimental apparatus, and performing advanced measurements in a fully operating machine.

The first project is reported in **Chapter 3**. There, I presented the original design of a new vacuum apparatus, which will be employed at LENS, in Florence, for the production of BECs of ^{39}K atoms. The aim of the new setup is to guarantee a high repetition rate of the experimental sequence for the production of degenerate gases of ^{39}K, large optical access onto the atoms, and tunability of the interactions. These three tasks can be accomplished in the newly designed system. In particular, the compact design of the 3D MOT chamber has been originally developed in the context of this thesis. It is meant to allow 3D magneto-optical trapping, the loading of the atoms in a in-vacuum resonator, and the optical transport of the atoms into the science chamber. This latter, thanks to its shape and position, spatially separated from the region of magneto-optical trapping, will allow a very large optical access onto the atoms, necessary for the implementation of a high-resolution imaging optical setup and laser speckles (as in ref. [36]). A proper configuration of magnetic field coils around each vacuum chamber has been designed, allowing for magnetic trapping (in the 2D MOT and 3D MOT chambers) and magnetic tuning of the interactions via Feshbach resonances (in the 3D MOT chamber and science cell). Technical features of the chosen vacuum pumps are given and motivated. Finally, a preliminary test of the optical setup that will be used for the optical transport in the experiment is presented.

Once it will be constructed, the vacuum apparatus will be integrated with

proper laser sources for cooling and optical trapping of ^{39}K. The new system will be flexible to many future studies. The first goal will be to investigate the role of weak repulsive short-range interactions on a Anderson localized system in random potentials, a very general problem of condensed matter physics which still poses many open questions [28].

Long-range interactions are instead at the basis of the investigation presented in **Chapter 4**. There, I reported on the first experimental observation of the population of the roton mode, i.e. a mode at finite momentum in the low-energy excitation spectrum, in a dipolar quantum gas [37], theoretically predicted by L.Santos and coworkers in 2003 [35]. This work has been performed at the ERBIUM experiment of the Experimental Physics Institute of the University of Innsbruck (Austria), on a dipolar BEC of ^{166}Er atoms. Despite previous theoretical works on rotons in dipolar BECs were mainly focused on quasi-2D systems, for our investigation, aimed at measuring the momentum distribution of the gas, we chose an axially elongated trap geometry, providing an enhanced roton population signature in momentum space, with respect to a quasi-2D trap. We measured the momentum distribution of the gas after a sudden decrease of the s-wave scattering length, achieved by exploiting a Feshbach resonance, below the dipolar length (DDI-dominated regime). For sufficiently low values of the s-wave scattering length, we observed a clear signature of the population of the roton mode, in the TOF absorption images of the gas, revealing the in-trap momentum distribution. We verifyed the predicted linear scaling of the roton momentum with the inverse of the harmonic oscillator length along the direction of tightest confinement, and the mild dependence of the roton momentum on the scattering length, in the dipole-dominated regime of interactions. To confirm our observations, we compared the measurements with an analytical model and numerical simulations, specifically developed for our system parameters. Both theoretical models revealed a good agreement with our experimental data, thus confirming the roton softening of the excitation spectrum in our system.

To have an insight on the in-trap dynamics induced by the sudden decrease of the scattering length, I performed time evolution numerical simulations, complementary to the above mentioned ones, reproducing the experimental sequence. These simulations provided information on the real-space density distribution of

the gas as a function of the holding time in the trap, which was not directly accessible in our system. The results have shown a complex in-trap dynamics. In particular, for values of the scattering length sufficiently below the dipolar length, the BEC density profile developed short-wavelength modulations, corresponding to the onset of the roton mode population in the system. When the scattering length was further decreased, an instability leading to a collpase dynamics has been observed.

To gain knowledge of the specific role of quantum fluctuations and three-body losses in the dynamics of the dipolar BEC, and particularly in the regime of mean-field collapse (where the relevance of these two effects has been firmly estabilished by previous theoretical and experimental works) I carried out additional dedicated simulations. These simulations confirmed the stabilizing role of the quantum fluctuations, and, showed that, in absence of three-body losses, long-lived high-density structures form in the system, which are very similar to the recently observed quantum droplets.

The work presented here paves the way for many future investigations on the roton physics in dipolar BECs. A first goal, for instance, is the measurement of the roton gap, which could be accessed via Bragg spectroscopy [140]. Also, by improving the resolution of the imaging system it would be possible to directly probe the in-trap real-space density modulations. These density modulations might constitute an interesting link between the observed softening of the roton mode and the existence of a supersolid phase in our system. Indeed, in a supersolid phase, a phase-coherent density modulated ground-state is predicted to exist [141]. In the reported experiment, we can only access density-modulated states which are not the ground state of the system, but rather excited metastable states, as a consequence of the interaction quench used to excite the roton mode. Therefore, one would need to develope new strategies for directly probing the ground state of the system and its coherence. First investigations in this direction have been reported in ref. [139]. Thus, future research might be devoted to exploring the possibility of a stable supersolid state in a dipolar BEC.

In the long term, an interesting perspective which connects the two projects of my PhD work, might be the study of dipolar systems in disordered potentials. The many-body localization problem in dipolar system has been studied theoretically

(see, for instance, ref. [142]), but not yet investigated in experiments. At present, as I already mentioned, the interplay of disorder and short-range interactions is itself not full understood. Once new insights on this problem will be achieved, degenerate gases of strongly magnetic atoms of Er could constitute an optimal platform for studying the generalization of the many-body localization problem to dipolar systems.

Bibliography

[1] M. H. Anderson, J. R. Ensher, M. R. Matthews, C. E. Wieman, E. A. Cornell, *Observation of Bose-Einstein Condensation in a Dilute Atomic Vapour*, Science **269**, 198 (1995).

[2] K. B. Davis, M.-O. Mewes, M. R. Andrews, N. J. van Druten, D. S. Durfee, D. M. Kurn, and W. Ketterle, *Bose-Einstein Condensation in a Gas of Sodium Atoms*, Phys. Rev. Lett. **75**, 3969 (1995).

[3] A. Einstein, *Quantentheorie des einatomigen idealen gases*, Sitzungsberichte der Preussischen Akademie der Wissenschaften, 1:3 (1925).

[4] M. R. Matthews, B. P. Anderson, P. C. Haljan, D. S. Hall, C. E. Wieman, and E. A. Cornell, *Vortices in a Bose-Einstein condensate*, Phys. Rev. Lett. **83**, 2498 (1999).

[5] I. Bloch, J. Dalibard, and W. Zwerger, *Many-body physics with ultracold gases*, Rev. Mod. Phys. **80**, 885 (2008).

[6] M.R. Andrews, C G. Townsend, H.-J. Miesner, D. S. Durfee, D. M. Kurn, and W. Ketterle, *Observation of Interference Between Two Bose Condensates*, Science **275**, 637-641 (1997).

[7] D. Jaksch, C. Bruder, J. I. Cirac, C. W. Gardiner, and P. Zoller, *Cold bosonic atoms in optical lattices*, Phys. Rev. Lett. **81**, 3108 (1998).

[8] M. Greiner, O. Mandel, T. Esslinger, T. W. Hänsch, and I. Bloch, *Quantum phase transition from a superfluid to a Mott insulator in a gas of ultracold atoms*, Nature **415**, 39 (2002).

[9] J. Billy, V. Josse, Z. Zuo, A. Bernard, B. Hambrecht, P. Lugan, D. Clement, L. Sanchez-Palencia, P. Bouyer, and A. Aspect, *Direct observation of Anderson localization of matter waves in a controlled disorder*, Nature **453**, 891 (2008).

[10] G. Roati, C. D'Errico, L. Fallani, M. Fattori, C. Fort, M. Zaccanti, G. Modugno, M. Modugno, and M. Inguscio, *Anderson localization of a non-interacting Bose–Einstein condensate*, Nature **453**, 895-898 (2008).

[11] C. Chin, R. Grimm, P. Julienne, and E. Tiesinga, *Feshbach resonances in ultracold gases*, Rev. Mod. Phys. **82**, 1225 (2010).

[12] C. C. Bradley, C. A. Sackett, and R. G. Hulet, *Bose-Einstein condensation of lithium*, Phys. Rev. Lett. **78**, 985 (1997).

[13] T. Weber, J. Herbig, M. Mark, H.-C. Nägerl, and R. Grimm, *Bose-Einstein condensation of Cesium*, Science **299**, 232 (2003).

[14] G. Modugno, G. Ferrari, G. Roati, R. J. Brecha, A. Simoni, and M. Inguscio, *Bose-Einstein Condensation of Potassium Atoms by Sympathetic Cooling* , Science *294*, 1320-1322 (2001).

[15] D. G. Fried, T. C. Killian, L. Willmann, D. Landhuis, S. C. Moss, D. Kleppner, and T. J. Greytak, *Bose-Einstein Condensation of Atomic Hydrogen*, Phys. Rev. Lett. **81**, 3811 (1998).

[16] A. Robert, O. Sirjean, A. Browaeys, J. Poupard, S. Nowak, D. Boiron, C. I. Westbrook, and A. Aspect, *A Bose-Einstein Condensate of Metastable Atoms*, Science **292**, 461 (2001).

[17] F. Pereira Dos Santos, J. Léonard, J. Wang, C. J. Barrelet, F. Perales, E. Rasel, C. S. Unnikrishnan, M. Leduc, and C. Cohen-Tannoudji, *Bose-Einstein Condensation of Metastable Helium*, Phys. REv. Lett. **86**, 3459 (2001).

[18] A. Griesmaier, J. Werner, S. Hensler, J. Stuhler, and T. Pfau, *Production of a chromium Bose-Einstein condensate*, Phys. Rev. Lett. **94**, 160401 (2005).

[19] Y. Takasu, K. Maki, K. Komori,T. Takano, K. Honda, M. Kumakura, T. Yabuzaki, and Y. Takahashi, *Bose-Einstein Condensation of Yb atoms*, Phys. Rev. Lett. **91**, 040404 (2003).

[20] S. Kraft, F. Vogt, O. Appel, F. Riehle, and U. Sterr, *Bose-Einstein Condensation of Alkaline Earth Atoms:* ^{40}Ca, Phys. Rev. Lett. **103**, 130401 (2009).

[21] S. Stellmer, M. K. Tey, B. Huang, R. Grimm, and F. Schreck, *Bose-Einstein Condensation of Strontium*, Phys. Rev. Lett. **103**, 200401 (2009).

[22] Y. N. Martinez de Escobar, P. G. Mickelson, M. Yan, B. J. DeSalvo, S. B. Nagel, and T. C. Killian, *Bose-Einstein Condensation of* ^{84}Sr, Phys. Rev. Lett. **103**, 200402 (2009).

[23] M. Lu, N. Q. Burdick, S. H. Youn, and B. L. Lev, *Strongly Dipolar Bose-Einstein Condensate of Dysprosium*, Phys. Rev. Lett. **107**, 190401 (2011).

[24] K. Aikawa, A. Frisch, M. Mark, S. Baier, A. Rietzler, R. Grimm, and F. Ferlaino, *Bose-Einstein Condensation of Erbium*, Phys. Rev. Lett. **108**, 210401 (2012).

[25] G. Roati, M. Zaccanti, C. D'Errico, J. Catani, M. Modugno, A. Simoni, M. Inguscio, and G. Modugno, ^{39}K *Bose-Einstein Condensate with Tunable Interactions*, Phys. Rev. Lett. **99**, 010403 (2007).

[26] L. Chomaz, S. Baier, D. Petter, M. J. Mark, F. Wächtler, L. Santos, and F. Ferlaino, *Quantum-Fluctuation-Driven Crossover from a Dilute Bose-Einstein Condensate to a Macrodroplet in a Dipolar Quantum Fluid*, Phys. Rev. X **6**, 041039 (2016).

[27] C. D'Errico, M. Zaccanti, M. Fattori, G. Roati1, M. Inguscio, G. Modugno and A. Simoni, *Feshbach resonances in ultracold* ^{39}K, New J. Phys. **9** (2007).

[28] D.M. Basko, I.L. Aleiner, B.L. Altshuler, *Metal-insulator transition in a weakly interacting many-electron system with localized single-particle states*, Annals of Physics **321**, 1126–1205 (2006).

[29] T.-C. Chiang, *Superconductivity in Thin Films*, Science **306**, 1900-1901 (2004).

[30] J.D. Reppy, *Superfluid helium in porous media*, J. Low Temp. Phys. **87**, 205 (1992).

[31] M. Baranov, L. Dobrek, K. Góral, L. Santos, and M. Lewenstein, *Ultracold dipolar gases - a challenge for experiments and theory*, Physica Scripta 2002 **74** (2002).

[32] H. Kadau, M. Schmitt, M. Wenzel, C. Wink, T. Maier, I. Ferrier-Barbut, and T. Pfau, *Observing the Rosensweig instability of a quantum ferrofluid*, Nature **530**, 194–197 (2016).

[33] N. A. Clark, *Soft-matter physics: Ferromagnetic ferrofluids*, Nature **504**, 229–230 (2013).

[34] V. Muñoz and L. Serrano, *Local versus nonlocal interactions in protein folding and stability – an experimentalist's point of view*, Folding and Design **1**, R71-R77 (1996).

[35] L. Santos, G.V. Shlyapnikov, and M. Lewenstein, *Roton-maxon spectrum and stability of trapped dipolar Bose-Einstein condensates*, Phys. Rev. Lett. **90**, 250403 (2003).

[36] G. Semeghini, M. Landini, P. Castilho, S. Roy, G. Spagnolli, A. Trenkwalder, M. Fattori, M. Inguscio, and G. Modugno, *Measurement of the mobility edge for 3D Anderson localization*, Nature Physics **11**, 554–559 (2015).

[37] L. Chomaz, R. M. W. van Bijnen, D. Petter, G. Faraoni, S. Baier, J. H. Becher, M. J. Mark, F. Wächtler, L. Santos, and F. Ferlaino, *Observation of the Roton Mode in a Dipolar Quantum Gas*, arXiv:1705.06914 (2017).

[38] K. Huang, *Statistical Mechanics*, Wiley, New York (1987).

[39] S. N. Bose, *Plancks gesetz und lichtquantenhypothese*, Zeitschrift fur Physik 26:178 (1924).

[40] D.A. Steck, *Quantum and Atom Optics*, available online at http://steck.us/teaching (revision 0.9.9, 18 March 2014).

[41] NIST Atomic Weigths and Isotopic Compositions, http://physics.nist.gov/PhysRefData/Compositions/index.html.

[42] T.G. Tiecke, *Properties of Potassium*, http://www.tobiastiecke.nl/archive/PotassiumProperties.pdf

[43] A. Frisch, *Dipolar Quantum Gases of Erbium*, PhD Thesis, LFU Innsbruck (2014).

[44] H. Ban, M. Jacka, J. Hanssen, J. Reader, and J. McClelland, *Laser cooling transitions in atomic erbium*, Opt. Express **13**, 3185 (2005).

[45] C. Cohen-Tannoudji and D. Guéry-Odelin, *Advances in Atomic Physics*, World Scientific Publishing (2011).

[46] H. Metcalf and P. van der Straten, *Laser cooling and trapping*, Springer-Verlag, New York (1999).

[47] M. Landini, *A tunable Bose-Einstein condensate for quantum interferometry*, PhD thesis, University of Trento (2012).

[48] T.W.Hänsch and A.L.Schawlow, *Cooling of gases by laser radiation*, Opt. Commun. **13**, 68 (1975).

[49] T. Bergeman, G. Erez, and H.J. Metcalf, *Magnetostatic trapping fields for neutral atoms*, Phys. Rev. A **35**, 1535 (1987).

[50] A. Frisch, K. Aikawa, M. Mark, A. Rietzler, J. Schindler, E. Zupani4ă, R. Grimm, and F. Ferlaino, *Narrow-line magneto-optical trap for erbium*, Phys. Rev. A **85**, 051401 (2012).

[51] J. Dalibard e C. Cohen-Tannoudji, *Laser cooling below the Doppler limit by polarization gradients: simple theoretical models*, J. Opt. Soc. Am. B **6**, 2023 (1989).

[52] S. Chu S, J.E. Bjorkholm,A. Ashkin, and A. Cable, *Experimental Observation of Optically Trapped Atoms*, Phys. Rev. Lett. **57**, 314 (1986).

[53] R. Grimm, M. Weidemüller, and Y. B. Ovchinnikov, *Optical dipole traps for neutral atoms*, Adv. At. Mol. Opt. Phys. **42**, 95 (2000).

[54] B. E. A. Saleh and M. C. Teich, *Fundamentals of photonics*, John Wiley & Sons, Inc. (1991).

[55] L. Chomaz, Introductory course on cold gases, University of Innsbruck (2016).

[56] H.F. Hess, *Evaporative cooling of magnetically trapped and compressed spin-polarized hydrogen*, Phys. Rev. B **34**, 3476 (1986).

[57] W. Ketterle, K.B. Davis, M.A. Joffe, A. Martin, and D.E. Pritchard, invited oral presentation at OSA Annual Meeting, Toronto, Canada (1993).

[58] C. S. Adams, H.J. Lee, N. Davidson, M. Kasevich, and S. Chu, *Evaporative Cooling in a Crossed Dipole Trap*, Phys. Rev. Lett. **74**, 3577 (1995).

[59] W. Ketterle, D.S. Durfee, and D.M. Stamper-Kurn, *Making, probing and understanding Bose-Einstein condensates*, Proceedings of the International School of Physics "Enrico Fermi", Course CLXIV, Varenna, 20 - 30 June 2006, edited by M. Inguscio, W. Ketterle, and C. Salomon (IOS Press, Amsterdam) (2008).

[60] S. Kotochigova, *Controlling interactions between highly magnetic atoms with Feshbach resonances*, Rep. Prog. Phys. **77**, 9 (2014).

[61] L.D. Landau, and E. M. Lifshitz, *Quantum Mechanics*, Pergamon, New York (1987).

[62] H. Feshbach, *A Unified Theory of Nuclear Reactions II*, Ann. Phys. **19**, 287 (1962).

[63] U. Fano, *Effects of Configuration Interaction on Intensities and Phase Shifts*, Phys. Rev. **124**, 1866 (1961).

[64] W.C. Stwalley, *Stability of Spin-Aligned Hydrogen at Low Temperatures and High Magnetic Fields: New Field-Dependent Scattering Resonances and Predissociations*, Phys. Rev. Lett. **37**, 1628 (1976).

[65] A.J. Moerdijk, B. J. Verhaar, and A. Axelsson, *Resonances in ultracold collisions of ^6Li, ^7Li, and ^{23}Na*, Phys. Rev. A **51**, 4852–4861 (1995).

[66] C. J. Pethick, H. Smith, *Bose–Einstein Condensation in Dilute Gases*, Cambridge University Press (2008).

[67] A. J. Moerdijk, H. M. J. M. Boesten, and B. J. Verhaar, *Decay of trapped ultracold alkali atoms by recombination*, Phys. Rev. A **53**, 916 (1996).

[68] T. Lahaye, C. Menotti, L. Santos, M. Lewenstein, and T. Pfau, *The physics of dipolar bosonic quantum gases*, Rep. Prog. Phys. **72**, (2009).

[69] M.A. Baranov, *Theoretical progress in many-body physics with ultracold dipolar gases*, Physics Reports, **464**,71-111 (2008).

[70] J. Stuhler, A. Griesmaier, T. Koch, M. Fattori, T. Pfau, S. Giovanazzi, P. Pedri, and L. Santos, *Observation of Dipole-Dipole Interaction in a Degenerate Quantum Gas*, Phys. Rev. Lett. **95**, 150406 (2005).

[71] T. Lahaye, J. Metz, B. Fröhlich, T. Koch, M. Meister, A. Griesmaier, T. Pfau, H. Saito, Y. Kawaguchi, and M. Ueda, *d-Wave Collapse and Explosion of a Dipolar Bose-Einstein Condensate*, Phys. Rev. Lett. **101**, 080401 (2008).

[72] T. Köhler, K. Góral, and P. S. Julienne, *Production of cold molecules via magnetically tunable Feshbach resonances*, Rev. Mod. Phys. **78**, 1311 (2006).

[73] R. Heidemann, U. Raitzsch, V. Bendkowsky, B. Butscher, R. Löw, and T. Pfau, *Rydberg Excitation of Bose-Einstein Condensates*, Phys. Rev. Lett. **100**, 033601 (2008).

[74] A. Petrov, E. Tiesinga, and S. Kotochigova, *Anisotropy-induced Feshbach resonances in a quantum dipolar gas of highly magnetic atoms*, Phys. Rev. Lett. **109**, 103002 (2012).

[75] A. Frisch, M. Mark, K. Aikawa, F. Ferlaino, J. L. Bohn, C. Makrides, A. Petrov, and S. Kotochigova, *Quantum chaos in ultracold collisions of gas-phase erbium atoms*, Nature **507**, 475–479 (2014).

[76] M. Berninger, A. Zenesini, B. Huang, W. Harm, H.-C. Nägerl, F. Ferlaino, R. Grimm, P. S. Julienne, and J. M. Hutson, *Feshbach resonances, weakly bound molecular states, and coupled-channel potentials for cesium at high magnetic fields*, Phys. Rev. A **87**, 032517 (2013).

[77] S. Giovanazzi, A. Görlitz, and T. Pfau, *Tuning the dipolar interaction in quantum gases*, Phys. Rev. Lett. **89**, 130401 (2002).

[78] F. Dalfovo, S. Giorgini, L. P. Pitaevskii, and S. Stringari, *Theory of Bose-Einstein condensation in trapped gases*, Rev. Mod. Phys. **71**, 463 (1999).

[79] N. Bogoliubov, *On the Theory of Superfluidity*, J. Phys. (Moscow) **11**, 23 (1947).

[80] E.P. Gross, *Structure of a quantized vortex in boson systems*, Nuovo Cimento **20**, 454 (1961).

[81] L.P. Pitaevskii, *Vortex Lines in an Imperfect Bose Gas*, Sov. Phys. JETP **13**, 451 (1961).

[82] E. A. Donley, N. R. Claussen, S. L. Cornish, J. L. Roberts, E. A. Cornell, and C. E. Wieman, *Dynamics of collapsing and exploding Bose-Einstein condensates*, Nature **412**, 295-299 (2001).

[83] L. Santos, G. V. Shlyapnikov, P. Zoller, and M. Lewenstein, *Bose-Einstein Condensation in Trapped Dipolar Gases*, Phys. Rev. Lett. **85**, 1791 (2000).

[84] M. Landini, S. Roy, G. Roati, A. Simoni, M. Inguscio, G. Modugno, and M. Fattori, *Direct evaporative cooling of ^{39}K atoms to Bose-Einstein condensation* Phys. Rev. A **86**, 033421 (2012).

[85] J. W. Goodman, *Speckle Phenomena in Optics: Theory and Applications*, Roberts and Company Publishers, (2007).

[86] C. B. Alcock, V. P. Itkin, and M. K. Horrigan, *Vapor pressure equations for the metallic elements:298-2500K*, Canadian Metallurgical Quarterly, 23-309, (1984).

[87] J. Catani, P. Maioli, L. De Sarlo, F. Minardi, and M. Inguscio, *Intense slow beams of bosonic potassium isotopes*, Phys. Rev. A **73**, 033415 (2006).

[88] J. Léonard, M. Lee, A. Morales, T. M. Karg, T. Esslinger and T. Donner, *Optical transport and manipulation of an ultracold atomic cloud using focus-tunable lenses*, New J. Phys. **16** (2014).

[89] J. M. Lafferty, *Foundations of Vacuum Science and Technology*, Wiley & Sons (1998).

[90] http://www.esrf.eu/Accelerators/Groups/InsertionDevices/Software/Radia.

[91] M. Mancini, *Realizzazione sperimentale di un gas quantistico degenere di atomi di Itterbio*, Master Thesis, University of Milano (2012).

[92] T. Gustavson, A. Chikkatur, A. Leanhardt, A. Görlitz, S. Gupta, D. Pritchard and W. Ketterle, *Transport of Bose-Einstein Condensates with Optical Tweezers*, Phys. Rev. Lett. **88** 3–6 (2001).

[93] http://www.optotune.com

[94] https://www.zemax.com/os/opticstudio

[95] http://www.optotune.com/products/focus-tunable-lenses/lens-drivers

[96] P. Kapitza, *Viscosity of Liquid Helium Below the λ-Point*, Nature **141**, 74 (1938).

[97] J. F. Allen and A. D. Misener, *Flow of Liquid Helium II*, Nature **141**, 75 (1938).

[98] H. Kamerlingh-Onnes, *The Superconductivity of Mercury*, Comm. Phys. Lab. Univ. Leiden *120b* (1911).

[99] L. Tisza, *Transport Phenomena in Helium II*, Nature **141**, 913 (1938).

[100] L. Landau, *Theory of the Superfluidity of Helium II*, Phys. Rev. **60**, 356 (1941).

[101] R. P. Feynmann, *Atomic theory of the Two-Fluid Model of Liquid Helium*, Phys. rev. **94**, 2 (1954).

[102] M. Cohen and R. P. Feynman, *Theory of Inelastic Scattering of Cold Neutrons from Liquid Helium*, Phys. Rev. **107**, 13 (1957).

[103] D. G. Henshaw and A. D. B. Woods, *Modes of Atomic Motions in Liquid Helium by Inelastic Scattering of Neutrons*, Phys. Rev. **121**, 1266 (1961).

[104] D. R. Allum, R. M. Bowley, and P. V. E. McClintock, *Evidence for Roton Pair Creation in Superfluid* ^{4}*He*, Phys. Rev. Lett. **36**, 1313 (1976).

[105] F. London, *On the Bose-Einstein Condensation*, Phys. Rev. **54**, 947 (1938).

[106] L. Onsager and R. Penrose, *Bose-Einstein Condensation and Liquid Helium*, Phys. Rev. **104**, 576 (1956).

[107] F. Dalfovo and S. Stringari, *Helium nanodroplets and trapped Bose–Einstein condensates as prototypes of finite quantum fluids*, J. Chem. Phys. **115**, 10078-10089 (2001).

[108] A.L. Fetter, *Ground state and excited states of a confined condensed Bose gas*, Phys. Rev. A **53**, 4245-4249 (1996).

[109] L. Pitaevskii and S. Stringari, *Bose-Einstein condensation and superfluidity*, vol. 164 Oxford University Press (2016).

[110] J. Steinhauer, R. Ozeri, N. Katz, and N. Davidson, *Excitation Spectrum of a Bose-Einstein Condensate*, Phys. Rev. Lett. **88**, 120407 (2002).

[111] D.H.J. O'Dell, S. Giovanazzi, and G. Kurizki, *Rotons in gaseous Bose-Einstein condensates irradiated by a laser*, Phys. Rev. Lett. **90**, 110402 (2003).

[112] R. Mottl, F. Brennecke, K. Baumann, R. Landig, T. Donner, and T. Esslinger, *Roton-Type Mode Softening in a Quantum Gas with Cavity-Mediated Long-Range Interactions*, Science **336**, 6088 (2012).

[113] M.A. Khamehchi, Y. Zhang, C. Hamner, T. Busch, and P. Engels, *Measurement of collective excitations in a spin-orbit-coupled Bose-Einstein condensate*, Phys. Rev. A **90**, 063624 (2014).

[114] S.-C. Ji, L. Zhang, X.-T. Xu, Z. Wu, Y. Deng, S. Chen, and J.-W. Pan, *Softening of roton and phonon modes in a Bose-Einstein condensate with spin-orbit coupling*, Phys. Rev. Lett. **114**, 105301 (2015).

[115] L.-C. Ha, L.W. Clark, C.V. Parker, B. M. Anderson, and C. Chin, *Roton-maxon excitation spectrum of Bose condensates in a shaken optical lattice*, Phys. Rev. Lett. **114**, 055301 (2015).

[116] V. Galitski and I.B. Spielman, *Spin–orbit coupling in quantum gases*, Nature **494**, 49–54 (2013).

[117] N. Gemelke, E. Sarajlic, Y. Bidel, S. Hong, and S. Chu, *Parametric amplification of matter waves in periodically translated optical lattices*, Phys. Rev. Lett. **95**, 170404 (2005).

[118] S. Ronen, D.C.E. Bortolotti, and J.L. Bohn, *Radial and angular rotons in trapped dipolar gases*, Phys. Rev. Lett. **98**, 030406 (2007).

[119] A.D. Martin and P.B. Blakie, *Stability and structure of an anisotropically trapped dipolar Bose-Einstein condensate: Angular and linear rotons*, Phys. Rev. A **86**, 053623 (2012).

[120] P.B. Blakie, D. Baillie, and R.N. Bisset, *Roton spectroscopy in a harmonically trapped dipolar Bose-Einstein condensate*, Phys. Rev. A **86**, 021604 (2012).

[121] M. Jona-Lasinio, K. Łakomy, and L. Santos, *Roton confinement in trapped dipolar Bose-Einstein condensates*, Phys. Rev. A **88**, 013619 (2013).

[122] R.M. Wilson, S. Ronen, and J.L. Bohn, *Critical superfluid velocity in a trapped dipolar gas*, Phys. Rev. Lett. **104**, 094501 (2010).

[123] S.S. Natu, L. Campanello, and S. Das Sarma, *Dynamics of correlations in a quasi-two-dimensional dipolar Bose gas following a quantum quench*. Phys. Rev. A **90**, 043617 (2014).

[124] A. Frisch, M. Mark, K. Aikawa, S. Baier, R. Grimm, A. Petrov, S. Kotochigova, G. Quéméner, M. Lepers, O. Dulieu, and F. Ferlaino, *Ultracold Dipolar Molecules Composed of Strongly Magnetic Atoms*, Phys. Rev. Lett. **115**, 203201 (2015).

[125] K. Aikawa, A. Frisch, M. Mark, S. Baier, R. Grimm, and F. Ferlaino, *Reaching Fermi Degeneracy via Universal Dipolar Scattering*, Phys. Rev. Lett. **112**, 010404 (2014).

[126] S. Baier, *An optical dipole trap for Erbium with tunable geometry*, Master thesis, LFU Innsbruck (2012).

[127] A.R.P. Lima and A. Pelster, *Quantum fluctuations in dipolar Bose gases*, Phys. Rev. A **84**, 041604 (2011).

[128] A.R.P. Lima and A. Pelster, *Beyond mean-field low-lying excitations of dipolar Bose gases*, Phys. Rev. A **86**, 063609 (2012).

[129] Y. Kagan, B.V. Svistunov, G.V. Shlyapnikov, *Effect of Bose condensation on inelastic processes in gases*, JETP Lett. **42**, 209 (1985).

[130] F. Wächtler and L. Santos, *Quantum filaments in dipolar Bose-Einstein condensates* Phys. Rev. **A** 93, 061603 (2016).

[131] F. Wächtler and L. Santos, *Ground-state properties and elementary excitations of quantum droplets in dipolar Bose-Einstein condensates*, Phys. Rev. A **94**, 043618 (2016).

[132] R.N. Bisset, R.M. Wilson, D. Baillie, and P.B. Blakie, *Groundstate phase diagram of a dipolar condensate with quantum fluctuations*, Phys. Rev. A **94**, 033619 (2016).

[133] I. Ferrier-Barbut, H. Kadau, M. Schmitt, M. Wenzel, and T. Pfau, *Observation of quantum droplets in a strongly dipolar Bose gas*, Phys. Rev. Lett. **116**, 215301 (2016).

[134] M. C. Payne, M. P. Teter, D. C. Allan, T. A. Arias, and J. D. Joannopoulos, *Iterative Minimization Techniques for Ab Initio Total-Energy Calculations:*

Molecular Dynamics and Conjugate Gradients, Rev. Mod. Phys. **64**, 1045 (1992).

[135] R. M. Wilson, *Manifestations of the Roton in Dipolar Bose-Einstein Condensates*, PhD Thesis, University of Colorado (2011).

[136] X. Antoine, W. Bao, and C. Besse, *Computational methods for the dynamics of the nonlinear Schrödinger/Gross–Pitaevskii equations*, J. Computational Phys. **187**, 1 318-342 (2003).

[137] I. Ferrier-Barbut, M. Schmitt, M. Wenzel, H. Kadau and T. Pfau, *Liquid quantum droplets of ultracold magnetic atoms*, J. Phys. B: At. Mol. Opt. Phys **49**, 214004 (2016).

[138] M. Schmitt, M. Wenzel, B. Böttcher, I. Ferrier-Barbut, and T. Pfau, *Self-bound droplets of a dilute magnetic quantum liquid*, Nature **539**, 259 (2016).

[139] M. Wenzel, F. Böttcher, T. Langen, I. Ferrier-Barbut, and T. Pfau, *Striped states in a many-body system of tilted dipoles*, arXiv:1706.09388 (2017).

[140] J. Stenger, S. Inouye, A. P. Chikkatur, D. M. Stamper-Kurn, D. E. Pritchard, and W. Ketterle, *Bragg Spectroscopy of a Bose-Einstein Condensate*, Phys. Rev. Lett. **82**, 4569 (1999).

[141] Y. Pomeau, and S. Rica, *Dynamics of a model of supersolid*, Phys. Rev. Lett. **72**, 2426–2429 (1994).

[142] N. Y. Yao,C. R. Laumann, S. Gopalakrishnan, M. Knap, M. Müller, E. A. Demler, and M. D. Lukin, *Many-Body Localization in Dipolar Systems*, Phys. Rev. Lett. **113**, 243002 (2014).

Acknowledgements

I would like to thank Prof. Giovanni Modugno and Prof. Francesca Ferlaino for supervising my PhD work during the past exciting three years. I am deeply grateful to Prof. Marco Fattori, Dr. Chiara D'Errico and Dr. Manfred Mark for their teaching and support. Many thanks to Dr. Lauriane Chomaz for her careful reading and revising of my manuscript, and for her precious suggestions to improve it. Finally, I thank all my colleagues from the research groups of Prof. Modugno in Florence and Prof. Ferlaino in Innsbruck. It has been a pleasure to work with them, and to learn from them.